Project information

Project full title	Connecting Russian and European Measures for Large-scale Research Infrastructures – plus
Project acronym	CREMLINplus
Grant agreement no.	871072
Instrument	Research and Innovation Action (RIA)
Duration	01/02/2020 – 31/01/2024
Website	www.cremlinplus.eu

Deliverable information

Deliverable no.	D4.2 (D31)
Deliverable title	Scientific report on results concerning the conceptual development of the following components of the USSR: main storage ring, magnetic system, magnets, injection scheme, RF system for rings, insertion devices
Deliverable responsible	NRC KI
Related Work-Package/Task	WP4 / Task 4.1
Type	Report
Author(s)	
Dissemination level	Confidential
Document Version	1
Date	28 January 2022
Download page	www.cremlinplus.eu, Collaboration Platform

Document information

Version no.	Date	Author(s)	Comment
1	28 Jan. 2022	V.S. Dyubkov, E.D. Tsyplakov, M.V. Lalayan, V.L. Shatokhin, R.A. Senin	—

This project has received funding from the European Union's Horizon 2020 research and innovation programme under grant agreement No. 871072.

Contents

1 Introduction 2

2 Main storage ring 2

3 Magnetic system 4

3.1 Main ring lattice option with reverse bends 23

4 Vacuum system 43

5 Magnets 52

6 Injection scheme 63

7 RF system for ring 72

8 Insertion devices 84

9 Bibliography 89

1 Introduction

This report summarizes the design studies performed by the beam dynamics group in the framework of the Cremlin+ project task 4.1 in 2020-2021. The main goal of this project is the design of a 6 GeV diffraction limited storage ring, the USSR (SYLA), with a target horizontal emittance of 70 pm·rad. The general layout and main features of the storage ring are very similar to those for ESRF-EBS main ring, however the increased length and reduced emittance require a complete revision of the lattice design. In addition, the USSR lattice being a green field machine therefore not suffering from the same constraints as the ESRF-EBS, critical subsystems such as injectors and injection schemes can be modernized and adapted in accordance with fourth generation light source peculiarities. The storage ring lattice design will be presented followed by an evaluation of the performance with top up injector option as well as a preliminary study of potential injections schemes for the USSR storage ring. RF system design was continued and the current results are presented. Beam energy loss in storage ring is to be compensated by several modified pillbox cavities. Cavity geometry features, its operation frequency choice and induced HOM parameters are discussed. HOM damping technique using rectangular waveguides and corrugated cylindrical waveguides were studied. Longitudinal impedance values of HOM are presented for initial accelerating cavity and structure with waveguides. Due to all magnets of the baseline lattice are similar those installed on ESRF-EBS, it is not needed to redesign it except additional extra short bend. Special activities were carried out to it. Furthermore, due to scaling EBS cell for USSR the vacuum system scaling is also considered.

2 Main storage ring

For now the USSR storage ring lattice is an adaptation of the ESRF-EBS lattice with an horizontal emittance reduced from 132 pm·rad to 72 pm·rad. Results on magnetic lattice design presented here

This project has received funding from the European Union's Horizon 2020 research and innovation programme under grant agreement No. 871072.

mainly are based on Reports prepared by ESRF group of this Project and presented in [1, 2]. The starting point of the design study is therefore an N_c cell periodic lattice including an injection straight section with large horizontal β-function to increase the acceptance at the injection point.

Providing the USSR will operate at the same energy as the ESRF-EBS ring and is using the same unit cell we can use the following scaling law to determine the number of cells $N_c$required to achieve the design 70 pm·rad [3]:

$$\varepsilon_x \propto \frac{E^2}{{N_c}^3},$$

where $E$is the beam energy and N_c the number of unit cells.Using this simple scaling law we find that 72 pm·rad horizontal emittance can be achieved with $39 > N_c > 40$. A natural way to achieve the design goal without deviating too much from the well optimized ESRF-EBS standard cell is therefore to increase the number of cells to 40 with respect to the initial 32.

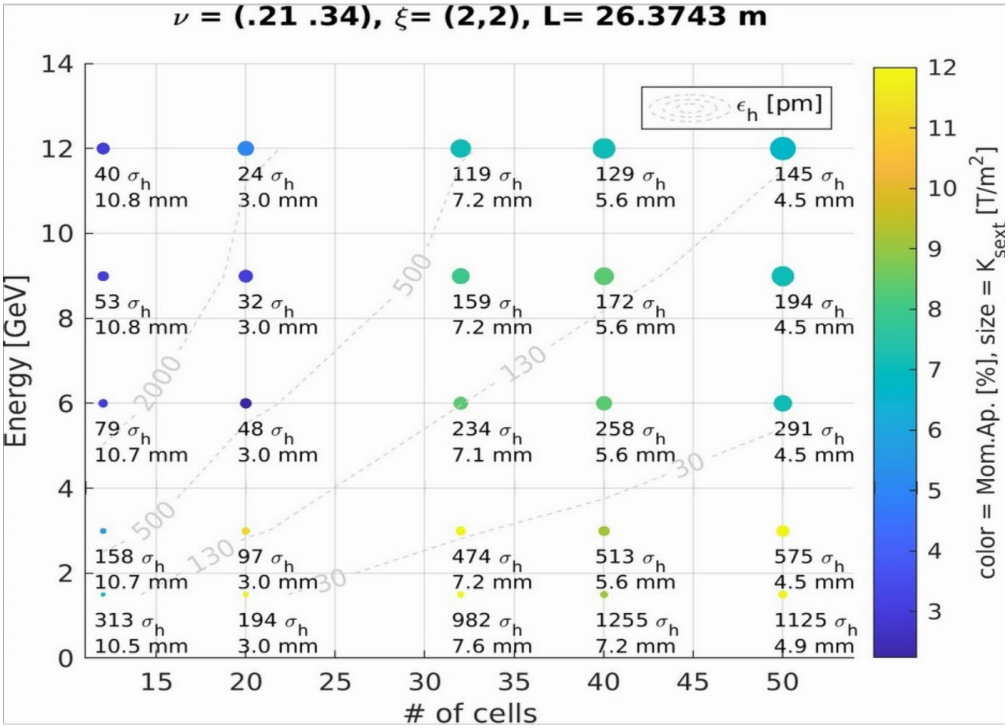

Figure 2-1: Main lattice parameters as a function of the beam energy and the number of identical cells (no injection cells)

Figure 2-1 shows the main machine parameters evolution as a function of the number of cells and the energy. The numbers represent the size of the dynamic aperture, in mm or in units of horizontal beam size, the grey lines the horizontal emittance, the size of the dots the strength of the sextupoles and their color the momentum acceptance. The dynamics aperture is representative of the injection efficiency while the momentum acceptance will constrain the achievable lifetime. We can see that at 6 GeV the 40 cells lattice will provide the desired emittance with performance consistent with the original 32 cells ESRF-EBS lattice. The strength of the sextupoles is increased but remains within the

This project has received funding from the European Union's Horizon 2020 research and innovation programme under grant agreement No. 871072.

design range of the ESRF-EBS sextupole magnets. This layout will therefore be assumed in all the following sections.

3 Magnetic system

The proposed 40 cells lattice, that is scaled EBS one, layout is presented in Figure 3-1. The magnets layout has few modifications compared to the EBS lattice [TDS]. All magnets gradients are within the same specifications of those realized for the ESRF EBS upgrade, therefore minimizing the magnet design effort. The tune were set to the ones of the ESRF-EBS.

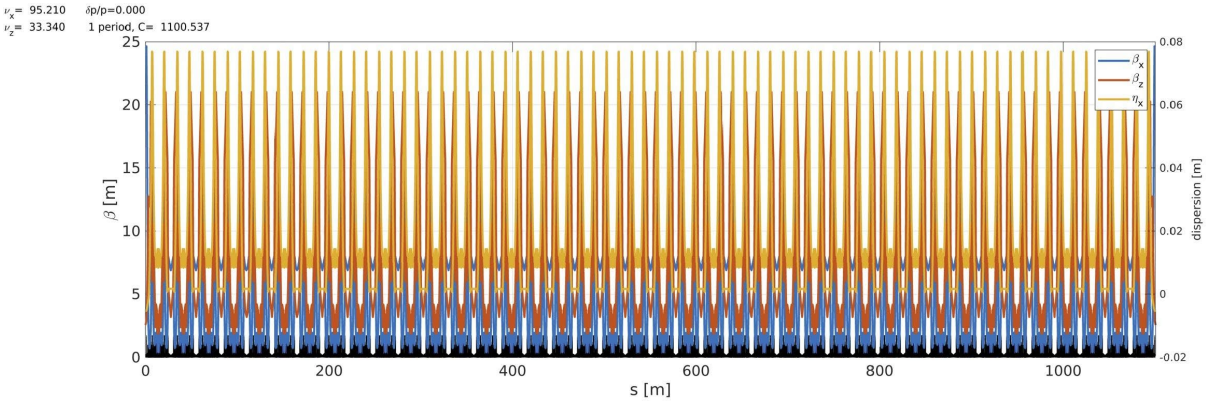

Figure 3-1: USSR lattice 40 cells: 38 standard arcs + 2 modified for injection. Injection at *s* = 0 m.

A table (Table 3-1) of relevant parameters is presented here. Two working lattice options are considered for USSR: one without short bend (SB) and of the same length of the EBS cell and one with short bend (SB) in every cell and slightly longer. This second option has one extra magnet to design and provides more than twice the number of beamlines, details will be presented in the following sections. Six straight sections are kept for accelerator operation: 1 for injection, 1 for injection improvements, 3 for RF, 1 for diagnostics. The RF frequency was chosen to be the same as the ESRF-EBS in order to be able to re-use the ESRF HOM damped cavities and existing 352.2 MHz power sources. The final arrangement and configuration of the straight sections should be decided in view of the beam lines requirements for this machine. In addition to the increased flexibility in terms of beam lines arrangement, the version including short bends meets all design requirements.

It should be noted that the natural horizontal emittance of the storage ring will be reduced when Insertion Device gaps are closed. Such a reduction is difficult to predict and will vary in time according to the users defined set points. The curve in Figure 3-2 shows the expected reduction of horizontal natural emittance as a function of the total radiated ID power. This curve assumes negligible dispersion is generated by the ID and zero dispersion at the straight sections. Future refined simulations will include the real ID installed. This curve however shows the potential achievable horizontal emittance in real operation conditions (excluding Intra Beam Scattering).

It should be noted that the natural horizontal emittance of the storage ring will be reduced when Insertion Device gaps are closed. Such a reduction is difficult to predict and will vary in time according to the users defined set points. The curve in Figure 3-2 shows the expected reduction of horizontal natural emittance as a function of the total radiated ID power. This curve assumes negligible dispersion is generated by the ID and zero dispersion at the straight sections. Future

This project has received funding from the European Union's Horizon 2020 research and innovation programme under grant agreement No. 871072.

refined simulations will include the real ID installed. This curve however shows the potential achievable horizontal emittance in real operation conditions (excluding Intra Beam Scattering).

Table 3-1: Main lattice parameters and comparison with the ESRF-EBS lattice.

6 GeV SR parameters	EBS	USSR 40 EBS cells	+SB
Circumference	844 m	1055 m	1103 m
# cells	32	40	40
# beamlines	27 ID + 17 BM	34 ID	34 ID + 40 BM
Nat. hor. emittance	140 pm·rad	68 pm·rad	72 pm·rad
Vertical emittance	5 pm·rad	5 pm·rad	5 pm·rad
Energy spread	$0.95\ 10^{-3}$	$0.85\ 10^{-3}$	$0.85\ 10^{-3}$
Mom. comp. factor	$8\ 10^{-5}$	$5\ 10^{-5}$	$7\ 10^{-5}$
Bunch length (I = 0)	2.9 mm	2.7 mm	3.3 mm
Tune (hor., vert.)	76.21, 27.34	95.21, 33.34	95.21, 33.34
Chromaticity (hor., vert.)	6,4	12,7.5	7,6
Energy loss / turn	2.6 MV	2.1 MV	2.0 MV
RF voltage	6.5 MV	5.0 MV	5.0 MV
RF frequency	352 MHz	352 MHz	352.2 MHz
Harmonic number	992	1241	1296
Max. total current	200 mA	200 mA	200 mA

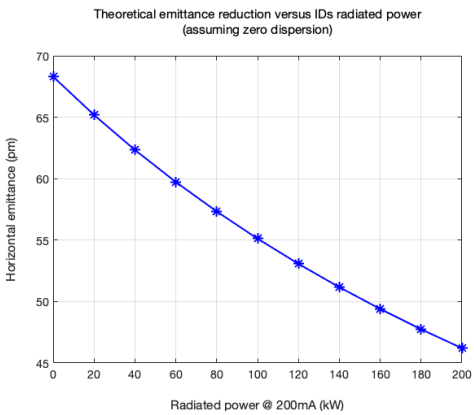

Figure 3-2: expected variation of natural horizontal emittance as a function of ID power at 200mA.

This project has received funding from the European Union's Horizon 2020 research and innovation programme under grant agreement No. 871072.

Damping wigglers can be introduced in the lattice which can both reduce the operational horizontal emittance and guarantee constant horizontal emittance during user operation[1] (insertion device gaps are varied by the users, affecting the horizontal emittance).

Figure 3-3 reports the dependence of the emittance and energy loss when including several W76 wigglers (a longer version of those used for ID19 at ESRF) in the USSR lattice . Two straight sections, each equipped with two 2.3 m long W76 devices each could reduce the horizontal emittance below 60 pm (excluding intra beam scattering effects) at the cost of a larger energy loss per turn (3 MeV/turn instead of 2 MeV/turn).

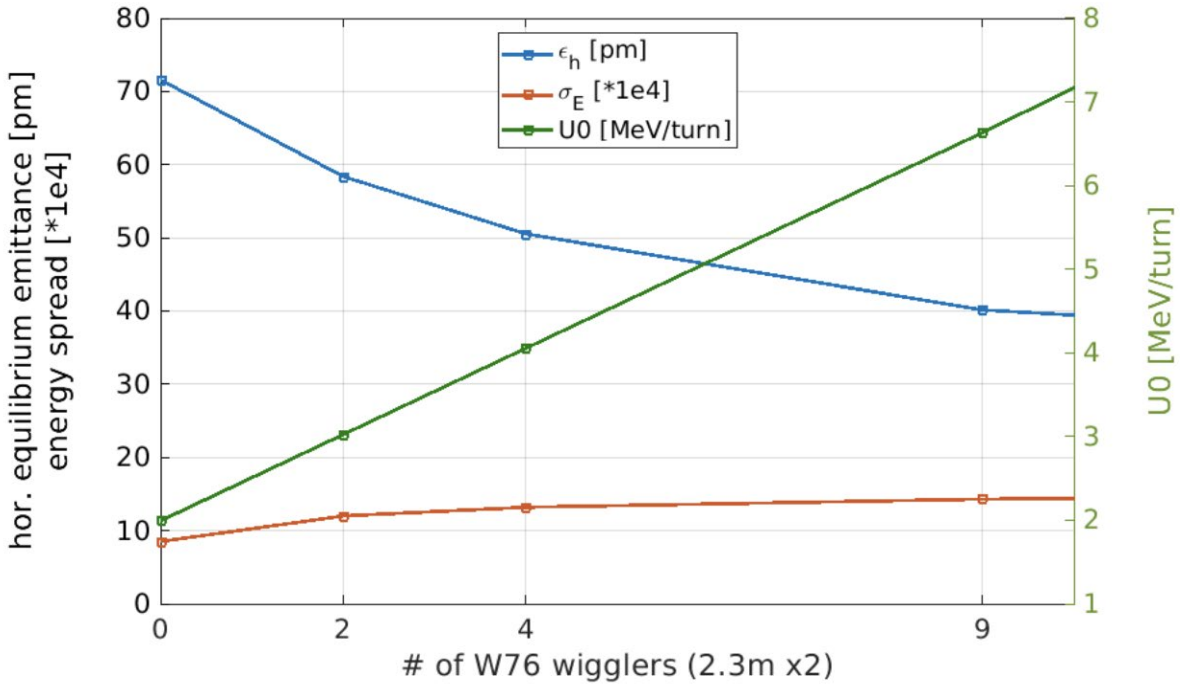

Figure 3-3: horizontal emittance, energy loss (right scale) per turn and energy spread as a function of the number of straight sections equipped with damping wigglers included in the lattice.

Intra Beam Scattering

The natural horizontal emittance of Table 3-1 is the zero current value. In normal operation, and in particular in the high current per bunch modes, the intrabeam scattering (IBS) effect can significantly increase the transverse beam size. In Figure 3-4, the horizontal and vertical emittance growth due to IBS effect are shown as a function of the bunch current, for different zero current vertical emittance values.

[1] The horizontal emittance is lowered closing the wigglers and increased with an horizontal white noise signal of amplitude determined to keep the measured horizontal emittance fixed. The reduction of horizontal emittance that would be observed by closing user undulator gaps is then canceled by a corresponding increase of horizontal white noise signal.

This project has received funding from the European Union's Horizon 2020 research and innovation programme under grant agreement No. 871072.

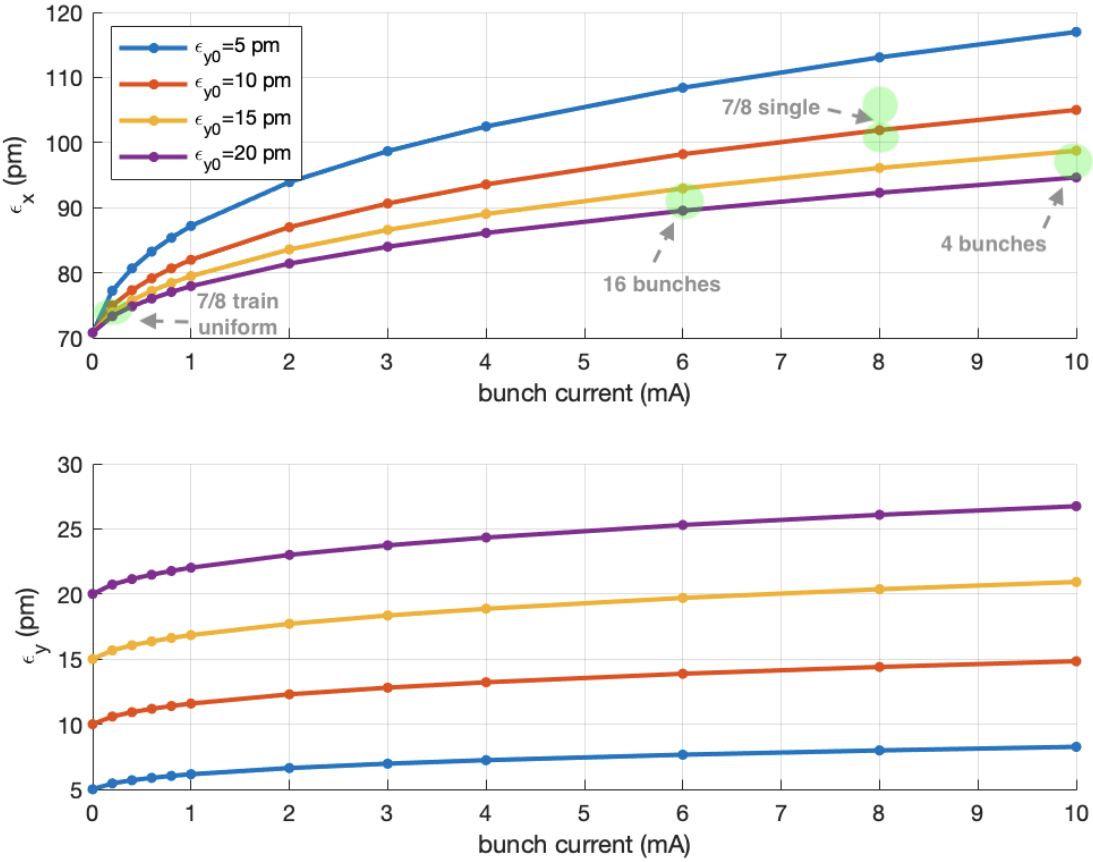

Figure 3-4: horizontal (top plot) and vertical (bottom plot) emittance growth as a function of the bunch current for the intrabeam scattering effect for 5, 10, 15 and 20 pm zero current vertical emittance. No ID gaps (0 radiated power). In green, the horizontal emittance for the different operation modes.

Standard cell

Figure 3-5 shows the USSR standard cell with SB, its length was increased by 1.215 m with respect to the ESRF-EBS standard cell to meet the design requirements in terms of total ring length and horizontal emittance. The magnet structure and layout remains the same except for the bending magnet sources. The RF frequency of the USSR-SB lattice is set to be 352.2 MHz, as described in [4]. The lattice length corresponding to 352.2 MHz is 1103 m.

To modify the circumference the DL dipole module lengths in all cells (standard and injection) are increased. This choice was made in order to minimize the modification of the vacuum chamber designs compared to EBS. The DL vacuum chambers already need to be modified due to the reduced angle in USSR compared to EBS and the module length was already changed to reduce the emittance for the SB lattice option. Also, this action has a small positive impact (-0.2 pm) on the horizontal equilibrium emittance as shown in Figure 3-6. Also the horizontal dispersion at the sextupoles is increased by this choice. The increase of total lattice length is done in subsequent steps, rematching the lattice optics to the reference quantities at each step.

This project has received funding from the European Union's Horizon 2020 research and innovation programme under grant agreement No. 871072.

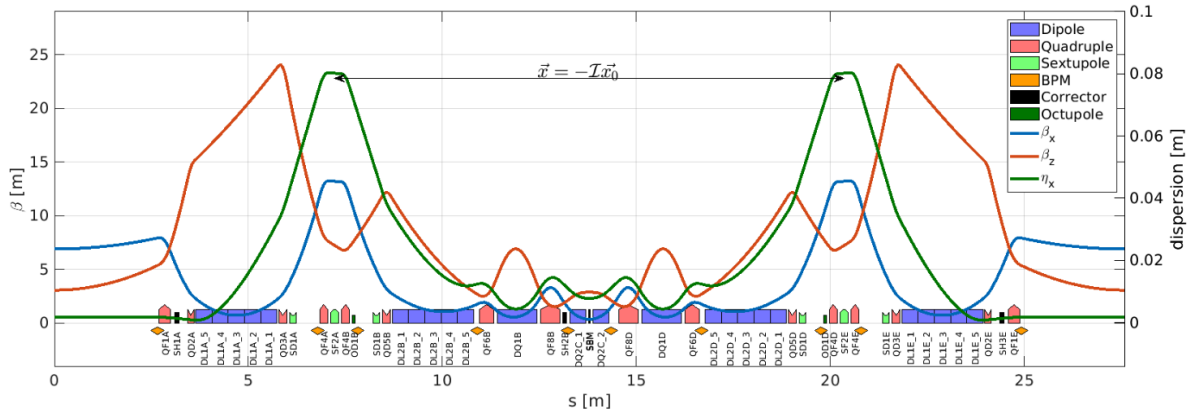

Figure 3-5: USSR lattice standard cell with short bend. Names of the magnets are reported in the figure.

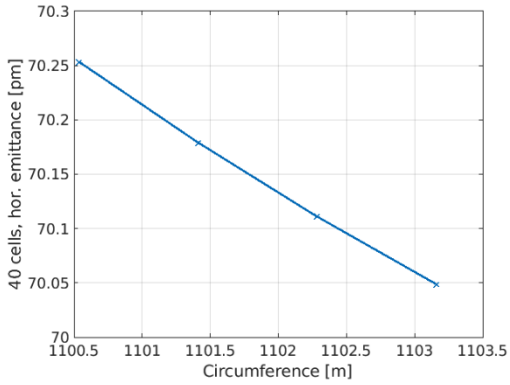

Figure 3-6: emittance of lattices of increasing length obtained by lengthening the DL modules.

The gradients of the proposed USSR lattice are compared to those of the EBS in Table 3-2. Due to the increased length and therefore reduced bending angle all dipole magnet designs and consequently the associated vacuum chambers design will need to be adapted. For this reason more flexibility is left for the specifications of dipole magnets.

The major difference between two options is the central DQ2 magnet that needs to be split in order to integrate a short bend dipole magnet to be used as a potential photon source. Also a new design for this magnet may be envisaged as done for example for the Brazilian light source SIRIUS. This is shown in Figure 3-7 with a zoom around the central area of the standard cell. Angular separation among Insertion Device and Short Bend sources is about 4.5° due to 9° of total standard cell angle.

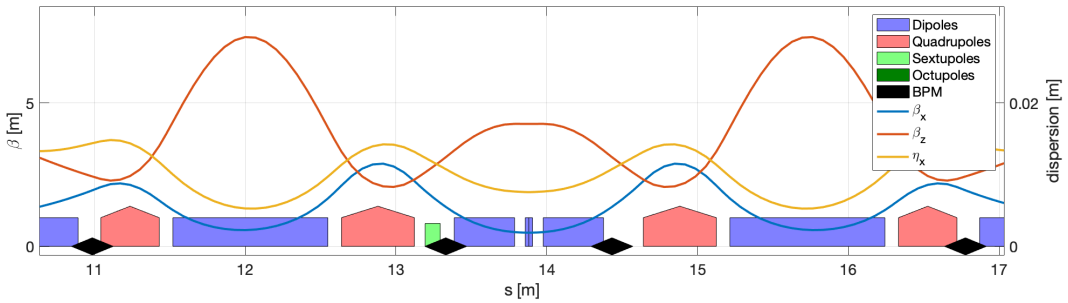

Figure 3-7: USSR lattice standard cells central region. A Short Bend is introduced in the cell center and the longitudinal dipoles are lengthened to optimize emittance.

This project has received funding from the European Union's Horizon 2020 research and innovation programme under grant agreement No. 871072.

Table 3-2 : list of gradients for EBS, and for two version of the USSR lattice. In bold magnets design to be revisited for USSR. Corresponding vacuum chambers would also need adjustment.

	EBS	USSR 40 EBS cells	USSR 40 long cells + SB
DL1	0.17 - 0.67 T L = 0.3576 m	0.14 - 0.54 T	**0.13 - 0.53 T** **L = 0.4178 m**
DL2	0.17 - 0.54 T L = 0.3576 m	0.14 - 0.43 T	**0.13 - 0.43 T** **L = 0.4178 m**
QF1	53.48 T/m	53.49 T/m	48.87 T/m
QD2	-57.05 T/m L = 0.212	57.37 T/m ***L = 0.212***	-56.82 T/m *L = 0.162*
QD3	-52.93 T/m L = 0.162	-52.78 T/m *L = 0.162*	-48.83 T/m ***L = 0.212 m***
QF4	52.09 T/m	52.12 T/m	52.12 T/m
QD5	-57.84 T/m	-57.89 T/m	-48.91 T/m
QF6	91.03 T/m L = 0.3880	91.21 T/m	**90.18 T/m** **L = 0.3745 m**
DQ1	0.57 T -36.86 T/m	0.45 T -36.85 T/m	**0.48 T** **-38.78 T/m**
QF8	89.38 T/m L = 0.4840	89.04 T/m	**92.21 T/m** **L = 0.4975 m**
DQ2	0.78 T -31.18 T/m L=0.8 m	0.63 T -31.09 T/m	**0.52 T** **-31.09 T/m** **L= 2 x 0.4 m**
SB	-	-	0.86 T L = 0.05 m
SD1AE	-1718 T/m^2	-2228 T/m^2	-2044 T/m^2
SF2	1657 T/m^2	2155 T/m^2	1705 T/m^2
SD1BD	-1617 T/m^2	2096 T/m^2	-1343 T/m^2
OD	-36000 T/m^3	36000 T/m^3	-44000 T/m^3

Injection cell

In order to accommodate classic and reliable off-axis injection schemes an ad-hoc injection cell is matched following the same strategies used for the EBS storage ring.

This project has received funding from the European Union's Horizon 2020 research and innovation programme under grant agreement No. 871072.

Figure 3-8 shows the two injection cells matched for the USSR storage lattice. In order to maximize the horizontal acceptance at the injection point and consequently the injection efficiency, the horizontal β-function was increase to 25.29 m. These cells will break the 40-fold storage ring symmetry and hence degrade the machine performance in terms of lifetime and injection efficiency. In order to minimize its impact, an additional quadrupole, QF2, was inserted in the DL surrounding the injection straight section, allowing to fully match the optics conditions at the boundaries while keeping the phase advance of the injection cells equal to the ones of the standard cell. In addition, two focusing quadrupoles (QF1IJ) are moved toward the center of the straight section to match the optics at the injection point. The gradient changes are limited to the first five quadrupoles on each side of the injection point therefore minimizing the variation of optics at the sextupoles. Nevertheless, the integration of the injection cells is not transparent and further optimizations are required to recover that will be described in the following sections.

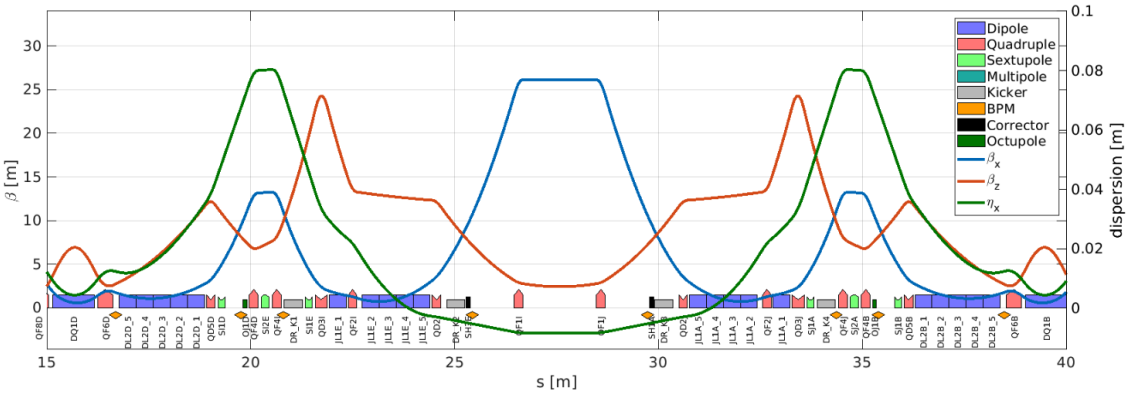

Figure 3-8: USSR lattice injection region. Two consecutive cells are modified.

The lattice length increase to match the harmonic number 1296 and RF frequency 352.2 MHz has no detrimental impact on the lattice performances in absence of errors, as shown in Figure 3-9 for a lattice including the injection cells. The dynamic aperture is computed at the injection point tracking e^- for 1024 turns. The Touschek lifetime is computed using the Piwinski formula in [5]. The longitudinal momentum acceptance required for this formula is computed over 4 cells of the ring, at each element and tracking for 1024 turns particles of increasing momentum at each longitudinal position.

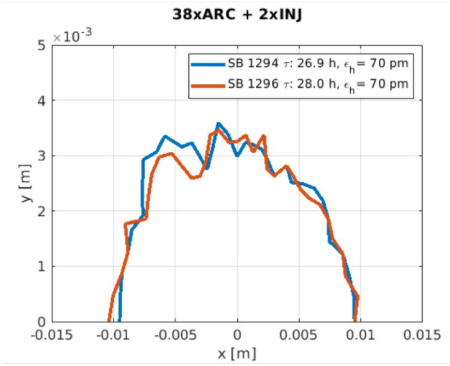

Figure 3-9: Dynamic aperture at injection and Touchek lifetime for a lattice (including injection cell) with harmonic number 1294 and length 1100 m and for a lattice with harmonic number 1296 and length 1103 m.

This project has received funding from the European Union's Horizon 2020 research and innovation programme under grant agreement No. 871072.

Lattice optimizations

This section summarizes the various optimizations performed to achieve the parameters presented in Table 3-1.

DL length optimizations

The Short Bend dipole allows to double the number of potential beamlines for users. However the introduction of this magnet in the lattice has an impact on the final achieved horizontal natural emittance. In particular, if no action is taken, the horizontal natural emittance increases from ~68 pm·rad to ~76 pm·rad due to the modified dipole fields along the cell (constant total angle).

This emittance variation may be recovered by tuning the DL modules lengths. Those magnets will have to be redesigned in any case due to the different lattice cell total angle. Figure 3-10 shows this process and depicts 1103 m as optimal lattice length with an emittance restored to 72 pm with one SB for every cell.

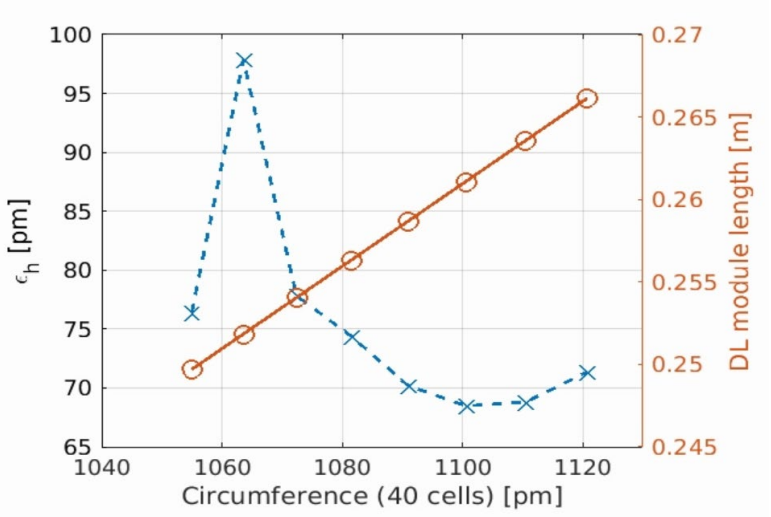

Figure 3-10: Scaling of DL modules length to optimize emittance for 40 cells lattice with Short Bend.

An optimization script has been defined to optimize the bending angles of the 12 dipoles in the cell (10 DL modules and 2 DQ dipole quadrupoles).

The script:

1. varies 11 independent dipole variables to minimize the effective emittance ($\sigma_x\sigma_{x'}$) at the Insertion device straight sections centers;
2. uses 1 dipole to fix the total cell angle to $2\pi/40$;
3. performs matching of the optics with all quadrupoles in the cell;
4. corrects the entrance and exit pole face angles to account for the change in bending angle of the individual magnets;
5. corrects the chromaticity.

The result of this optimization performed for increasing dispersion at the IDs straight section centers is displayed in Figure 3-11. For dispersions at the ID straight section centers below 1.5 mm it is possible to reduce the natural and effective emittance varying the bending angles. Above 1.5 mm instead the optimization is not able to find a better bending angle distribution. Thus, there is no better configuration found for the current baseline lattice with short bend (red dot on the Figure 3-11). Further increase of the dispersion at the straight section would not lead to improved horizontal effective emittance and it is thus also discarded.

This project has received funding from the European Union's Horizon 2020 research and innovation programme under grant agreement No. 871072.

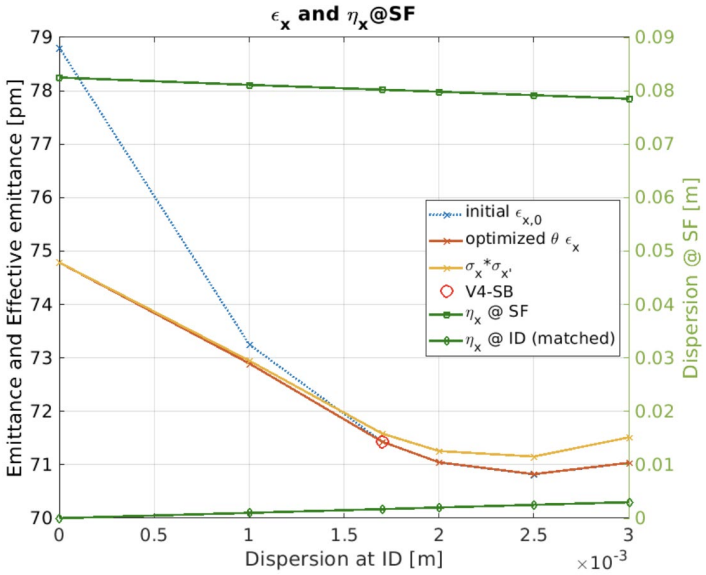

Figure 3-11: Optimization of bending angles of a standard arc cell as a function of the dispersion set at the center of the ID straight section.

Following an iterative step by step process all the optics parameters free for optimization were tested and varied to find an optimum. Initially several two dimensional scans were performed, however with limited success.

The quantities optimizes where:

- tune working point (scanning several units of tune)
- vertical beta and alpha at sextupole SF centers
- phase advance between sextupoles
- horizontal beta and dispersion at the center of Insertion device straight sections.
- chromaticities
- Sextupoles SD unbalance ($\Delta K_{SD1AE} = -\Delta K_{SD1BD}$) and octupole strength
- sextupoles and octupoles in the injection cells.

Figure 3-12 shows the search for an optimum tune working point. No better point compared to the one found for EBS is observed.

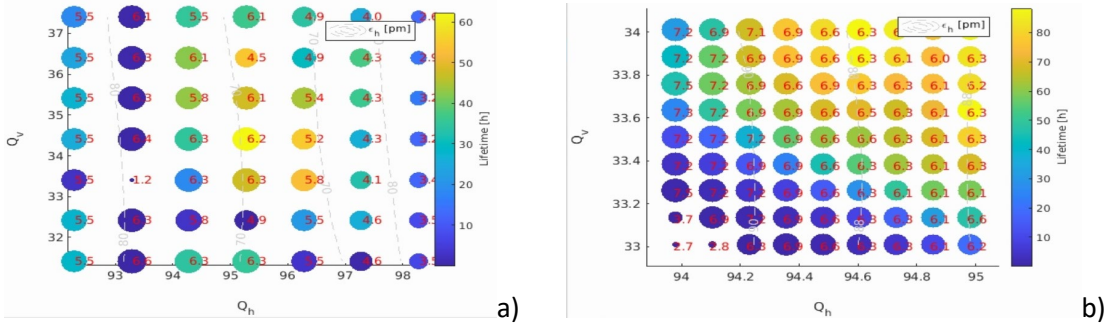

a) b)

Figure 3-12: tune working point integer part optimization 40xARCA cells (no injection). Color is lifetime, size of spot and red numbers the maximum DA at injection. Grey contours delimit equal horizontal natural emittance regions. a) several units, b) 1 unit.

This project has received funding from the European Union's Horizon 2020 research and innovation programme under grant agreement No. 871072.

Several other optimizations are shown in Figure 3-13. Only the optimization of chromaticity showed a clear improvement for larger chromaticities.

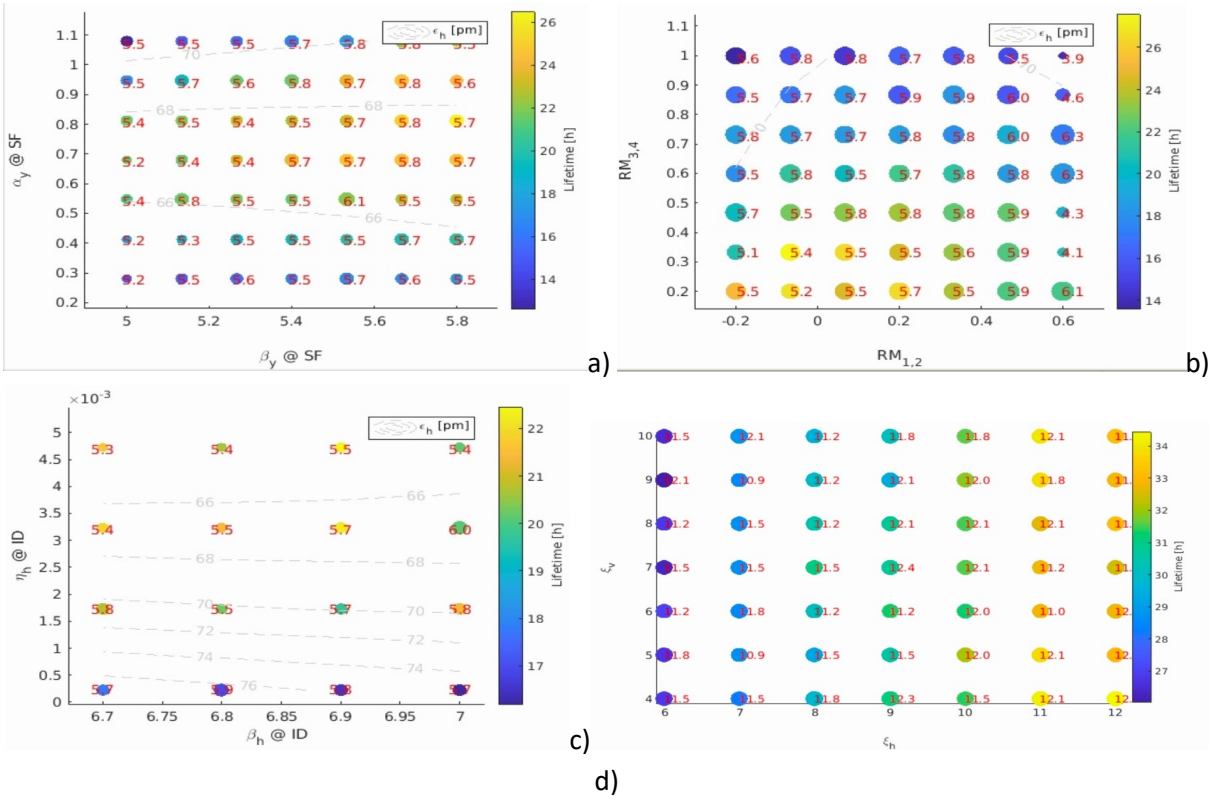

Figure 3-13: 2D optimization of 40xARCA cells (no injection) optics. Color is lifetime, size of spot and red numbers the maximum DA at injection. Grey contours delimit equal horizontal natural emittance regions. a) vertical beta and alpha at SF2 center, b) RM12 RM34 among SF2, c) dispersion and horizontal beta at straigth section, d) chromaticity.

All these parameter scans were performed initially for the periodic lattice with 40 identical cells and later iterated including the injection cells.

Sextupole optimizations

Sextupole optimizations are essential to obtain the best possible lifetime and dynamic aperture. This section summarizes, the action taken prior to the errors studies and the resulting standard performance figure of merits such as dynamic aperture, amplitude detuning or Touschek lifetime.

Periodic W functions and Dispersion derivative using injection sextupoles

The sextupoles and octupoles in the injection cell are adjusted in order to recover periodicity for the off-energy optics [6, 7]. The effect of this action is depicted in Figures 3-14 and 3-15.

This project has received funding from the European Union's Horizon 2020 research and innovation programme under grant agreement No. 871072.

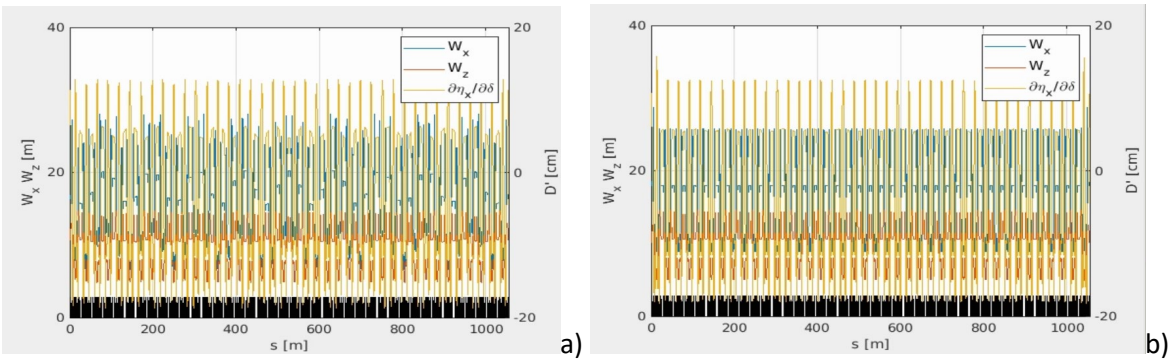

a) b)

Figure 3-14: USSR lattice ring W functions and dispersion derivative with energy. The sextupoles and octupoles in the injection cell are adjusted to recover periodicity in the rest of the lattice. a) before sextupoles and octupoles adjustement, b) after sextupole and octupoles adjustement.

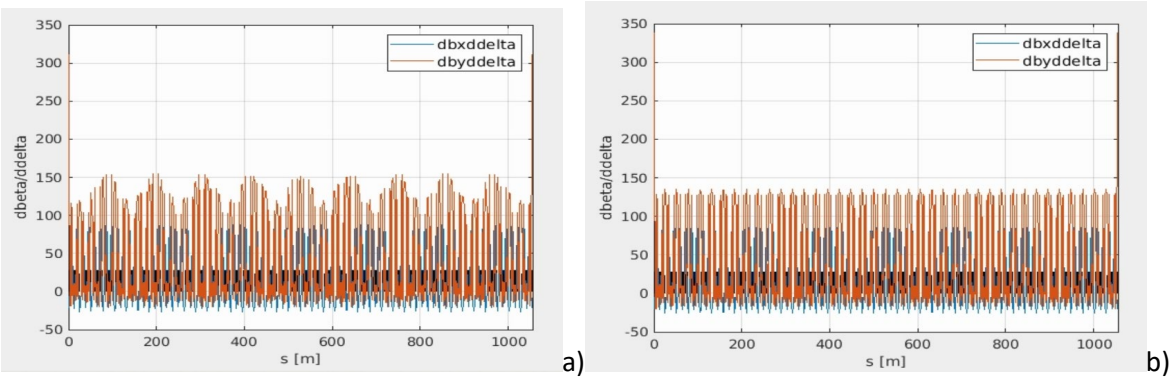

a) b)

Figure 3-15: USSR lattice ring beta functions variation with energy. a) before sextupoles and octupoles adjustement, b) after sextupole and octupoles adjustement.

MOGA optimizations

Multi objective genetic optimizations [6,8-10] have been set in place to further optimize the lattice cell optics and sextupole and octupole gradients. No errors were set at this stage.

More than 1000 different lattices were tested, and modified pointing toward improved lifetime and dynamic aperture. The modifications of the lattice included: 1) optics at sextupoles, phase advance among sextupoles, sextupoles and octupoles (at fixed chromaticity). Each of the optics had W function periodicity restored and RF cavity appropriately set for lifetime estimate. The Touschek lifetime was computed with fixed vertical emittance of 5pm.rad and bunch lengthening for ⅞ uniform filling (<0.2 mA/bunch, Z = 0.67 Ohm). Figure 3-16 shows the progress of such a process and the effectiveness of its application. These optimizations are nevertheless only preliminary as full lattices with errors and corrections must be used for a final realistic optimization.

DA, TLT, detuning with amplitude for lattice without errors

The parameters scan and the MOGA optimizations led to the dynamic aperture and lifetimes depicted in Figure 3-17.

This project has received funding from the European Union's Horizon 2020 research and innovation programme under grant agreement No. 871072.

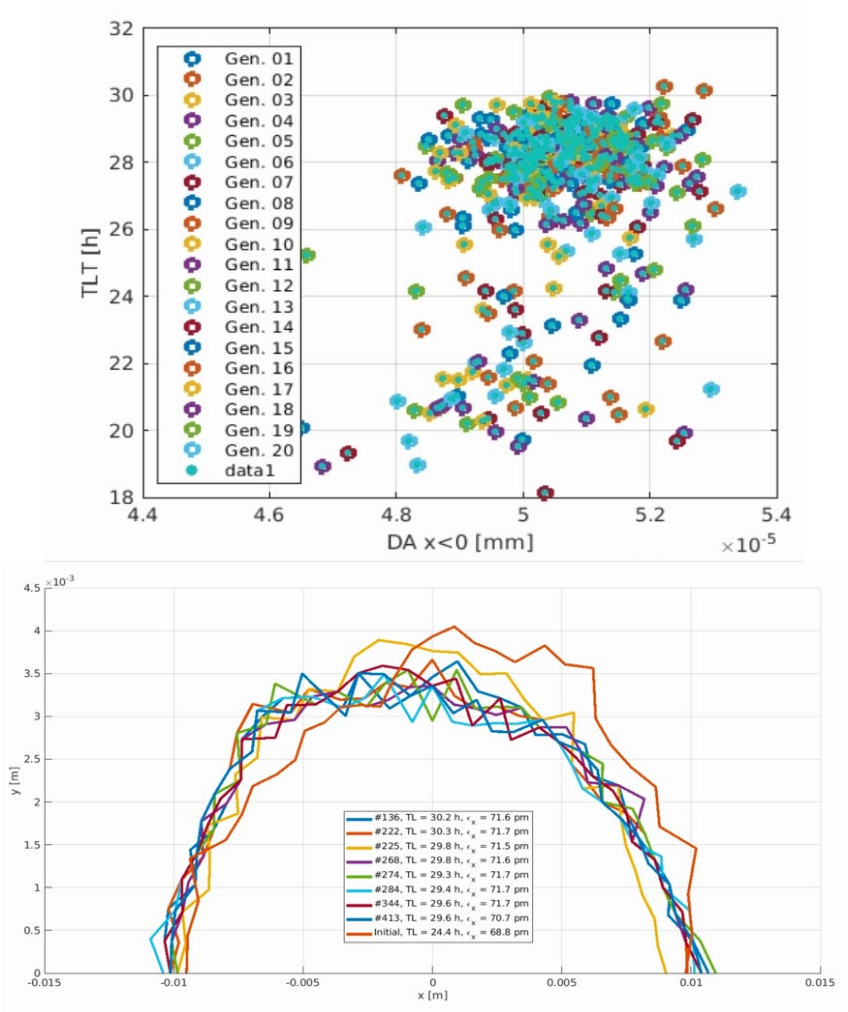

Figure 3-16: Multi Objective Genetic Algorithm progress (top) and resulting potential good candidates (bottom).

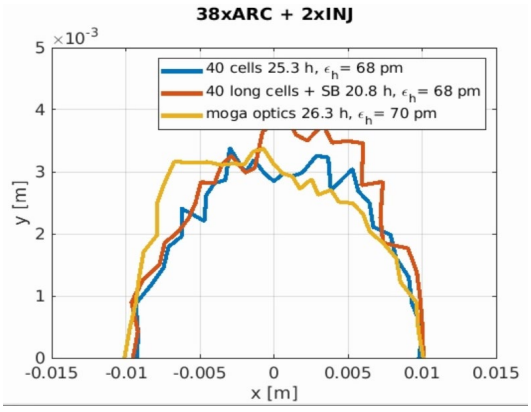

Figure 3-17: Dynamic aperture, lifetime and horizontal natural emittance for: 1) the EBS-like cell, 2) the USSR cell with SB and longer DL, 3) the USSR cell with SB longer DL and MOGA optimized optics.

The physical apertures are set in the lattice following the EBS vacuum chamber geometry. The apertures are approximated as elliptic in the lattice model, even if the profile of the chamber is more complex. For the straight section vacuum chambers this represents the real profile of the vacuum

This project has received funding from the European Union's Horizon 2020 research and innovation programme under grant agreement No. 871072.

chamber. Tapering of the apertures is not considered. The values are set at every element to be the average along that given element. Rectangular apertures are used (as more appropriate) at the collimators and at the injection septum. ID vacuum chambers are set to a full gap of 8 mm in every straight section. This is the value presently achievable for in-air undulator gaps. Several ID will be in-vacuum and the gap will be smaller for these devices, reaching values as low as 6mm or less.

This represents a first, simplified, version of the aperture model. An error in the estimate of lifetimes and injection efficiency is clearly possible, but will not affect the final conclusions. We keep on this choice for simplicity. Figure 3-18 reports a view of the apertures set at each element in the standard cell of the USSR.

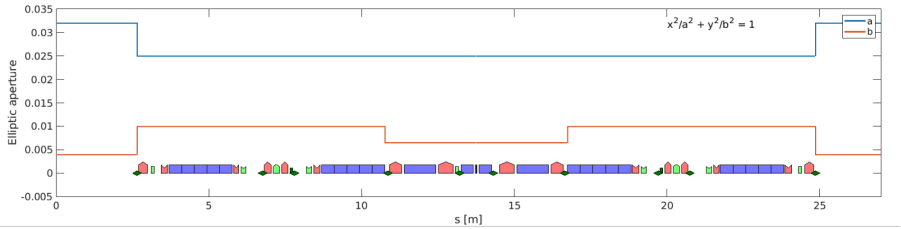

Figure 3-18: Physical elliptic apertures in the USSR standard arc cell assuming the EBS vacuum chamber design.

The injection cell has the same aperture distribution, except at the septum where an internal limit to -15 mm is imposed by the septum blade.

The dynamic aperture with and without apertures are compared in Figure 3-19. There is no impact on Touschek lifetime in absence of errors.

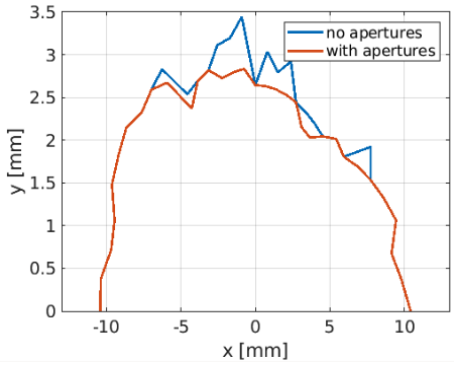

Figure 3-19: Dynamic aperture with & without physical elliptic apertures in the USSR lattice with SB.

Detuning with amplitude and momentum

The variation of tunes with horizontal amplitude and with momentum deviation is an indication of the lattice stability.

In Figure 3-20 it is visible that the horizontal tune hits the half integer resonance at about 7 mm. This value will probably determine a limitation once errors are introduced in the lattice.

This project has received funding from the European Union's Horizon 2020 research and innovation programme under grant agreement No. 871072.

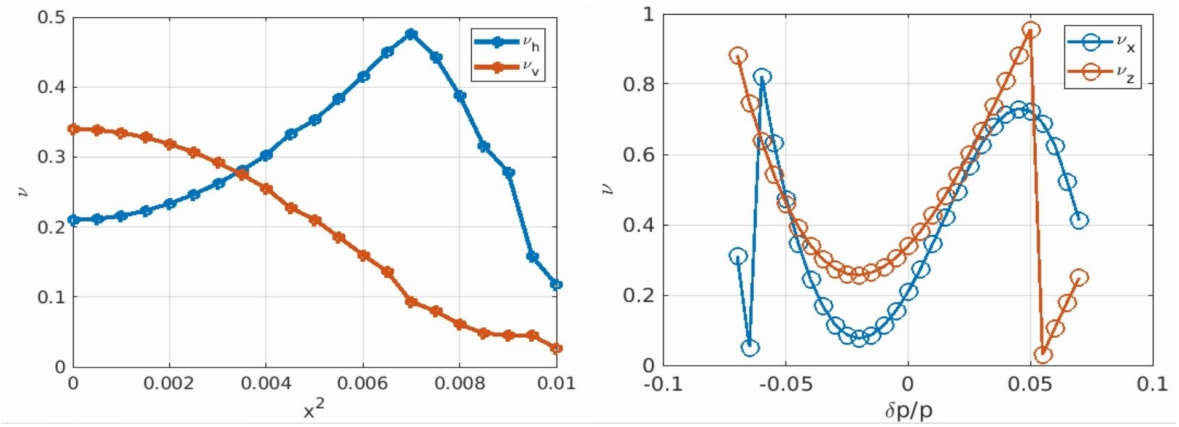

Figure 3-20: Detuning with amplitude and momentum for the USSR lattice.

Optimum RF Voltage

The momentum acceptance along the lattice may be limited by the RF voltage. This imposes larger RF voltages than the bare energy loss per turn. On the other hand too large RF voltages would lead to short bunches again impacting lifetime. The dependence of lifetime on total RF voltage is computed (see Figures 3-21 and 3-22). The simulations give that total RF voltage of 5 MV is the optimum value. For faster computation, and since this is only a comparative figure, the absolute values of lifetime are not to be considered. These are computed on a single cell rather than 4 cells (used for the values presented above) for speed reasons.

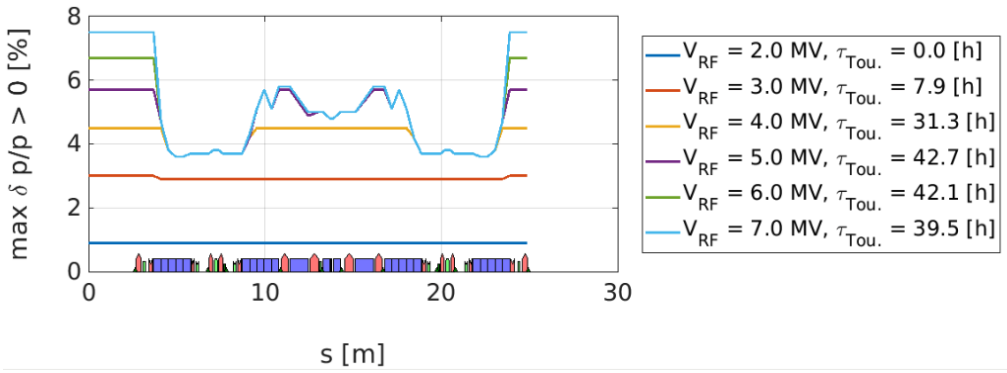

Figure 3-21: Simulated local momentum acceptance and Touschek lifetime vs RF Voltage for USSR lattice with SB [11].

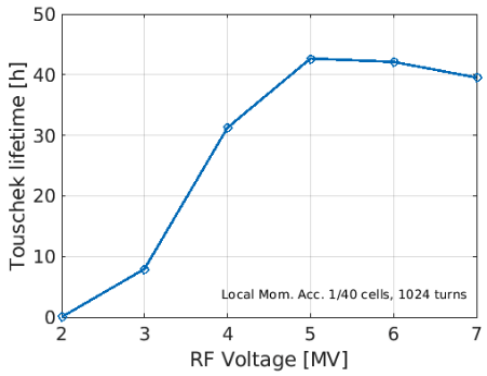

Figure 3-22: Simulated Touschek lifetime vs RF Voltage for USSR lattice with SB.

This project has received funding from the European Union's Horizon 2020 research and innovation programme under grant agreement No. 871072.

Errors studies

The lattice with errors represent the most realistic model of the future machine, in this section we assume alignment errors similar to those achieved for the ESRF-EBS. In the case of the ESRF-EBS the errors used for simulations turned out to be pessimistic and better performance was achieved thanks to a better than expected alignment of the machine. The values used for simulations are presented in Table 3-3.

Dynamic apertures (DA), lifetimes (LT) and injection efficiencies (IE) for several injector options are computed using the ESRF cluster. To obtain realistic values for those quantities alignment and gradient errors defined in Table 3-3 are set producing 10 different realization of the lattice.

Table 3-3: Alignment and gradient errors rms (normal distribution truncated at 2.5σ) used for dynamic aperture, injection efficiency and lifetime estimations.

rms single magnet errors Gaussian truncated at 2.5σ	**Δx [μm]**	**Δy [μm]**	**ΔΦ [μrad]**	**10^4·ΔK/K**
Dipoles	50	50	90	10
Dipole-Quadrupoles	50	50	90	5
Quadrupoles	50	50	90	5
High grad. quadrupoles	50	50	90	5
Sextupoles	50	50	90	35
Octupoles	50	50	90	40
Beam Position Monitors	50	50	0	0
Correctors	200	200	0	0

Commissioning-like corrections are applied to each of the lattices to obtain stable optics before computing DA, LT and IE.The corrections applied follow this order:

1. first turns steering
2. orbit
3. tune
4. chromaticity
5. optics
6. coupling
7. iteration of the above steps from 2 to 6.

Detailed description of the correction listed above and error setting for ESRF EBS can be found in [12]

DA / LT with errors

The images (Figure 3-23) below depict the reduction of DA after introducing errors and correction. IE for top-up linac with photogun is 97.6%. Such simulations result for the proposed USSR lattice options in the values reported in Table 3-4.

This project has received funding from the European Union's Horizon 2020 research and innovation programme under grant agreement No. 871072.

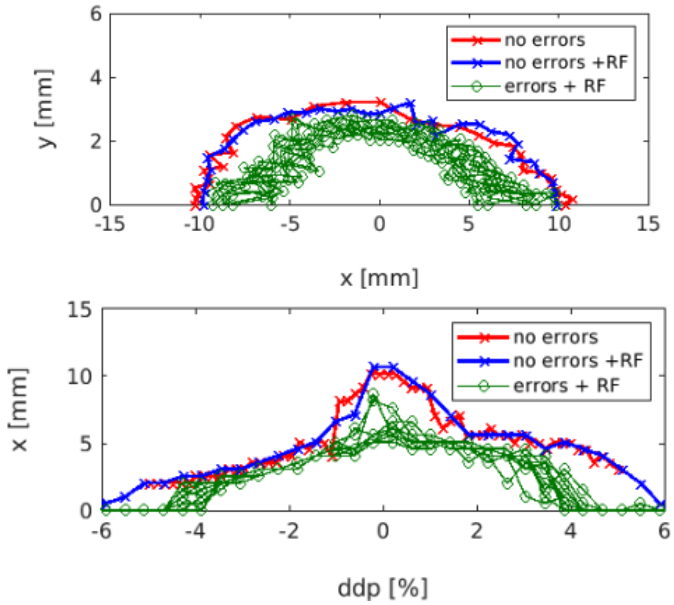

Figure 3-23: DA, TLT for lattices with errors and corrections. The image title reports all quantities with errors, and without errors.

Table 3-4: lattice global performance parameters in presence of errors and correction.

6 GeV SR with errors and correction	**EBS** S28F 2019	**USSR 40 EBS cells**	**USSR 40 long cells + SB**
max DA at injection	-8.7 ± 0.3 mm	-8.1 ± 0.4 mm	-8.7 ± 1.0 mm
Touschek lifetime ε_v = 5 pm, Z_n/n = 0.67Ohm, expected lifetime scaling EBS values: 12.4 h (⅞ uniform)			
⅞ uniform	19.6 ± 0.7 h	9.2 ± 1.5 h	11 ± 1 h
16 bunches	2.0 ± 0.1 h	1.0 ± 0.2 h	0.9 ± 0.1 h
4 bunches	1.3 ± 0.1 h	0.7 ± 0.1 h	0.6 ± 0.1 h
Injection efficiency, optimized beta at injection, 3mm septum, 1mm stay clear, off-axis parallel bump, 2σ cut (max expected I.E. = 97.7%)			
Short booster	85 ± 6 %	52 ± 15 %	-
Linac Thermo. gun	-	94 ± 7 %	97.5 ± 0.1 %
Linac Photo. gun	-	98 ± 2 %	97.4 ± 0.1 %

Alternative schemes of correction will have to be studied in particular to avoid issues observed for the ESRF EBS lattice.

Considering the parameters listed above the lattice option including SB seems the most promising. It allows to accommodate the largest number of beamlines and has appropriate injection

This project has received funding from the European Union's Horizon 2020 research and innovation programme under grant agreement No. 871072.

efficiency for any of the envisaged injectors, even considering the worst case scenario of traditional off-axis injection.

Proposed list of filling modes for USSR-SB

With the harmonic number 1296 (2^4x3^4) it is possible to specify different filling patterns for the USSR storage ring user operation. The filling patterns are presently adapted from the EBS ones, but will need input from the users community. The chosen harmonic number allows a rather flexible choice of filling modes.

All filling patterns presently in operation for EBS can be foreseen for USSR. Table 3-5 shows an initial possible list of filling schemes for USSR.

Table 3-5: list of possible filling modes for the USSR storage ring with harmonic number 1296.

Name	Filling scheme	Users	Total current, mA
⅞ + 4 mA	1 single bunch of 4 mA gap of 80 empty bunches train of 1134 bunches (0.17 mA/bunch) gap of 81 empty bunches	timing flux	200
uniform	1296 bunches (0.15 mA/bunch)	flux	200
16 bunches	16 repetitions of: ➔ 1 bunch of 4 mA ➔ 80 empty bunches	timing (flux)	64
8 bunches	4 repetitions of: ➔ 1 bunch of 5 mA ➔ 323 empty bunches	timing	40
26x8 +4 mA	1 single bunch of 8 mA gap of 101 empty bunches 26 repetitions of: ➔ 8 filled bunches (0.94 mA/bunch) ➔ 34 empty bunches gap of 102 empty bunches	timing flux	200

A schematic view of three of the proposed filling modes (the most frequently used for ESRF-EBS) is available in Figure 3-24 and the corresponding bunch lengths are displayed in Figure 3-25.

This project has received funding from the European Union's Horizon 2020 research and innovation programme under grant agreement No. 871072.

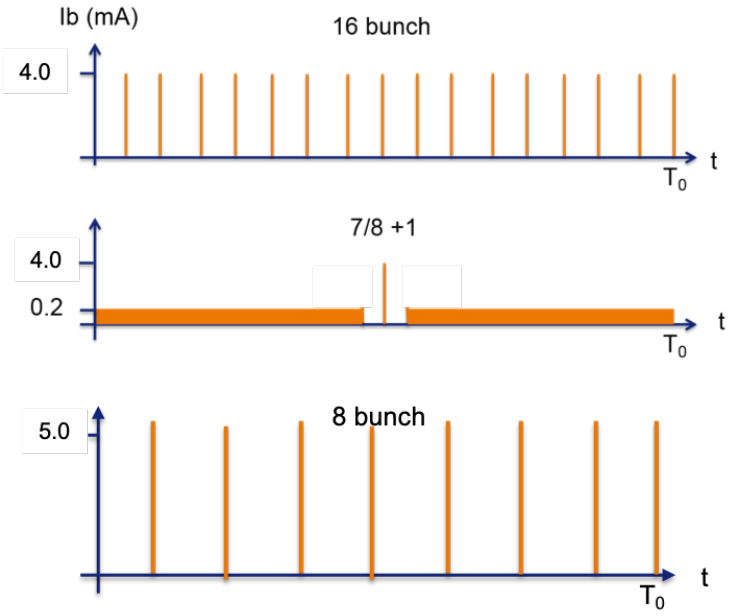

Figure 3-24: Schematic view of possible most frequently used filling modes for USSR.

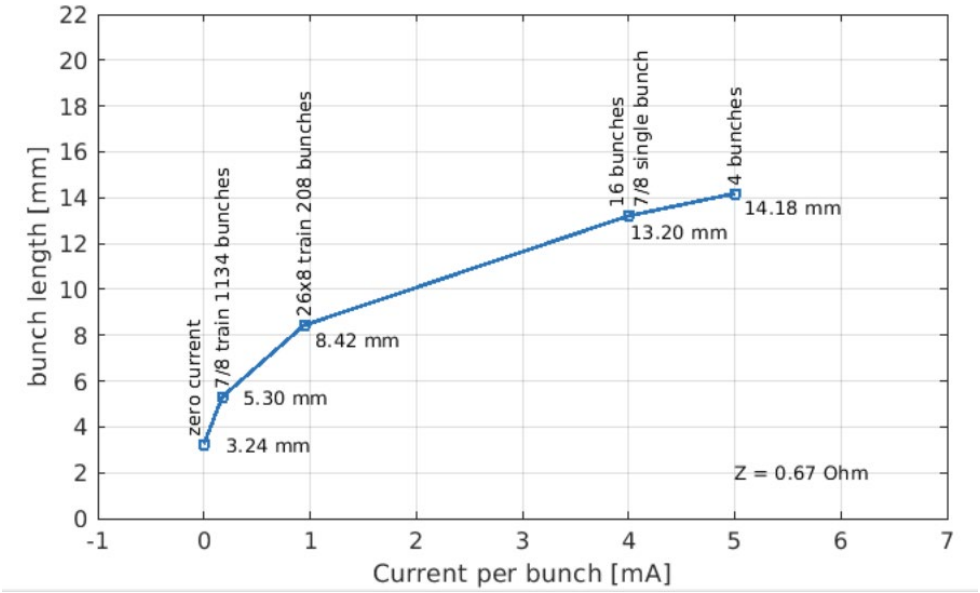

Figure 3-25: Bunch length for the different filling patterns.

The most frequently used filling mode for EBS is the ⅞ + 4 mA (>50% of users service mode). For this mode the beam sizes for the train (⅞) and single bunch (4 mA) are shown in Figures 3-26 and Tables 3-6 including the contribution of the photon beam for an undulator of length 5.3 m (filling the whole straight section) and at a wavelength of 60 fm. It has to be noted that assuming a vertical emittance of 10 pm the vertical beam size for a train of electrons in ⅞ + 4 mA (or uniform mode) the electron beam size is smaller than the photon beam size. The beta functions at the IDs are matched to close to optimal values (Length of undulators divided by 2, ~2.5 m) as in [13] only in the vertical plane.

This project has received funding from the European Union's Horizon 2020 research and innovation programme under grant agreement No. 871072.

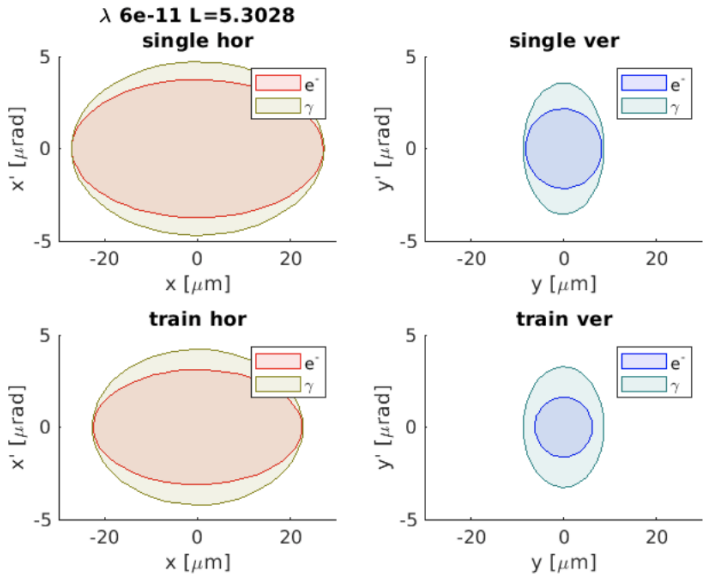

Figures 3-26: Electron and photon beam phase space at ID center for train and single bunch of a ⅞+4mA filling mode (see Table 3-5). In the vertical plane, for the specified wavelength, the electron beam size is smaller than the photon beam size.

Table 3-6: electron and photon beam sizes at the ID straight sections center for train and single bunch of a ⅞+4mA filling mode (see Table 3-5) assuming 45% horizontal emittance increase due to IBS effect.

σ_{rad}	2.8389	L = 5.3028
σ'_{rad}	1.6819	$\lambda = 6e-11$
	H	V
$\langle\beta_{ID}\rangle$	7.2396 m	3.8322 m
ϵ_{train}	70 pm	10 pm
bunch length (train)	5.3015 mm	
$\delta_E(train)$	0.085119 %	
σ_{train}	22.558	6.1905 um
σ'_{train}	3.1095	1.6154 urad
$\Sigma_{train}=\sqrt{\sigma^2+\sigma_{rad}^2}$	22.736	6.8104 um
$\Sigma'_{train}=\sqrt{\sigma'^2+\sigma'^2_{rad}}$	4.2105	3.2663 urad
ϵ_{single}	101.5 pm	13.0049 pm
bunch length (single)	13.2022 mm	I = 4 mA
$\delta_E(single)$	0.085119 %	
σ_{single}	27.1461	7.0596 um
σ'_{single}	3.7443	1.8422 urad
$\Sigma_{single}=\sqrt{\sigma^2+\sigma_{rad}^2}$	27.2942	7.609 um
$\Sigma'_{single}=\sqrt{\sigma'^2+\sigma'^2_{rad}}$	4.6989	3.3842 urad

The same data is reported for Short Bending magnet sources (in the center of each cell) in Figure 3-27 and in Table 3-7. In this case the length of the source is assumed to be the length of the SB dipole. The photon beam at this source location is smaller than at the IDs in both planes (smaller beta functions) and has a larger divergence in the horizontal plane.

This project has received funding from the European Union's Horizon 2020 research and innovation programme under grant agreement No. 871072.

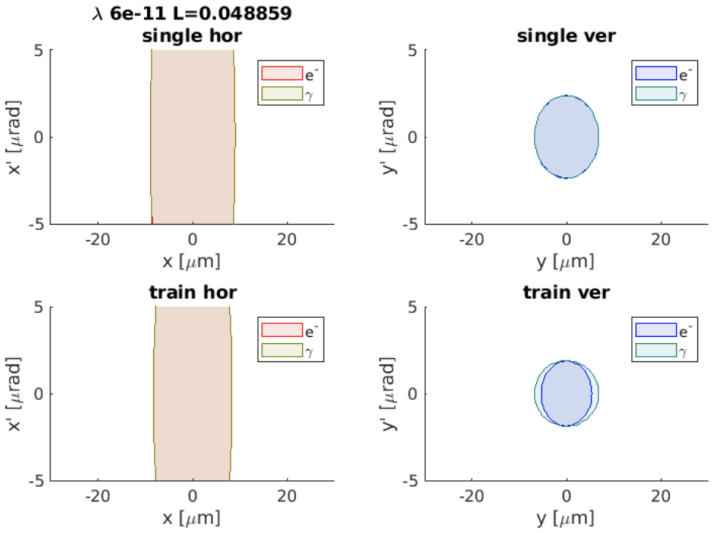

Figure 3-27: electron and photon beam phase space at SB center for train and single bunch of a ⅞+4 mA filling mode (see Table 3-5). In the vertical plane, for the specified wavelength, the electron beam size is smaller than the photon beam size.

Table 3-7: electron and photon beam sizes at the SB center for train and single bunch of a ⅞+4 mA filling mode (see Table 3-5) assuming 45% horizontal emittance increase due to IBS effect

σ_{rad}	0.2725	$\mathrm{L} = 0.048859$
σ'_{rad}	17.5216	$\lambda = 6e-11$
	H	V
$\langle\beta_{SB}\rangle$	0.37046 m	2.8711 m
σ_{train}	8.3295	5.3583 um
σ'_{train}	13.7533	1.8663 urad
$\Sigma_{train}=\sqrt{\sigma^2+\sigma_{rad}^2}$	8.334	5.3652 um
$\Sigma'_{train}=\sqrt{\sigma'^2+\sigma_{rad}'^2}$	13.756	1.8861 urad
σ_{single}	9.0028	6.8032 um
σ'_{single}	16.5584	2.3695 urad
$\Sigma_{single}=\sqrt{\sigma^2+\sigma_{rad}^2}$	9.0069	6.8086 um
$\Sigma'_{single}=\sqrt{\sigma'^2+\sigma_{rad}'^2}$	16.5606	2.3851 urad

3.1 Main ring lattice option with reverse bends

Except for basic lattice, that is scaled and a slightly modified version of that for ESRF-EBS, we considered additional options in order to slow down a value of the electron beam equilibrium horizontal emittance from the designed 70 pm down to 40 pm. This question is dictated by similar synchrotron projects being developed at 6 GeV and with a perimeter of about 1100 m such as APS-U (USA) and HEPS (China). Magnet lattices of those projects are HMBA modifications. Magnet lattices of that projects are HMBA modifications. It is well known that the special “knob” that helps decrease beam emittance in the lattice with longitudinal gradient bend for the frozen machine circumference is reverse bends [14-16] as it is done for APS-U and HEPS projects. The designed horizontal emittance for APS-U and HEPS is about three times lower that for ESRF-EBS and achieved by the introduction of reverse bends. From the other hand, mentioned projects will have significantly lower DA and it is supposed that on-axis injection will be used.

This project has received funding from the European Union’s Horizon 2020 research and innovation programme under grant agreement No. 871072.

In our case the main idea was the introducing reverse bends (RB) in the baseline 7BA lattice with SB without its significant modification. The simplest way is to use some quads as reverse bends by a small shift it from beam orbit. The most sensitive region of the standard cell is the central part. Selected quadrupoles (see Figure 3-28) can be shifted horizontally with regards to the optical axis, to generate a dipole field of resulting negative angle:

$$\theta = -k_1 l \Delta x$$

with k_1 the strength of the quadrupole, l its length and Δx the horizontal displacement.

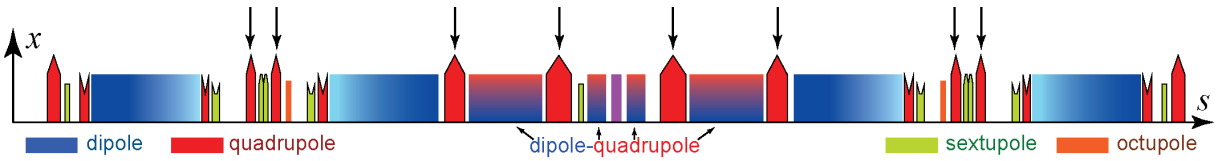

Figure 3-28: Baseline H7BA lattice layout with selected quadrupoles.

The first approaches were limited to the standard cell and assumed a homogeneous distribution of the total reverse bending angle, to simplify the scan and the results analysis. After insertion of the reverse bends, their total angle is scanned from 0 to -1 degree. At each step, the geometry of the cell should be restored; two methods were considered and tested to restore the total angle:

- **Sum method:** the total reverse bending angle (TRBA = $\sum \theta_{RB}$) is compensated by adding a constant value to all dipole angles. The angular distribution along the cell simply becomes $\theta_{RB} = -|TRBA|/N_{RB}$ for reverse bending quadrupole magnets and $\theta_{dip} = \theta_0 - |TRBA|/N_{dip}$ for the standard bending magnets (DL1, DL2, DQ1 and DQ2), where N_{RB}, N_{dip} are respectively the number of reverse bends and dipoles in the cell, and θ_0 the bending angle of the dipoles in the nominal lattice.
- **Proportional method:** the total angle here is restored by applying a corrective factor $C = 2\pi/(N_{cells} \cdot a)$ on all dipole fields (standard dipoles and reverse bends), with a the cell angle before correction ($a = \sum \theta_{dip,0} + \theta_{RB,0}$) and N_{cells} the periodicity. The change in angle per dipole therefore is: $\theta_{RB,0} = -|TRBA|/N_{RB}$, $\theta_{RB} = C \cdot \theta_{RB,0}$ and $\theta_{dip} = C \cdot \theta_{dip,0}$, where *C* is the corrective factor defined previously. Finally $\sum \theta_{RB} + \theta_{dip} = 2\pi/N_{cells}$.

The insertion of the reverse bending magnets and the correction of the total angle modified considerably the dispersion along the cell. The hybrid lattice with reverse bends was thus rematched, in terms of: dispersion, dispersion derivative, Twiss functions at IDs and sextupoles, phase advance between the sextupoles and cell total phase advance. The chromaticities were kept fixed to (7,6) for a fair comparison of the cell dynamics.

Two scans of TRBA were conducted, following each angular restoration method. The variation of both the horizontal natural emittance and the momentum compaction factor for the proportional method are displayed in Figure 3-29. The sum method experiences similar variations. As expected [17], the natural horizontal emittance follows a parabolic variation with regards to the total reverse bending angle, the momentum compaction factor a linear variation.

This project has received funding from the European Union's Horizon 2020 research and innovation programme under grant agreement No. 871072.

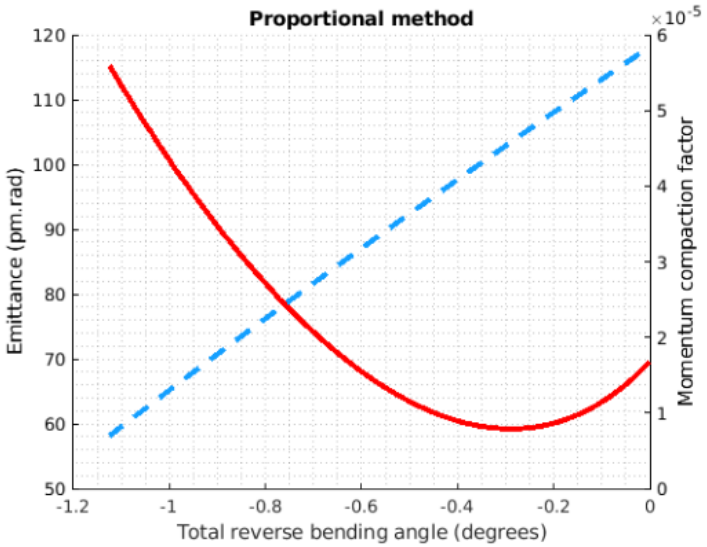

Figure 3-29: Variation of the emittance and the momentum compaction factor for the proportional angular restoration methods.

The general characteristics of the two minimum emittance lattices obtained using both angular correction methods are compared in Table 3-8. Stronger reduction in natural horizontal emittance is achieved with the proportional method, with similar total reverse bending angle and energy spread, and lower losses.

Table 3-8: Comparison of parameters for different angular correction methods.

Standard cell	USSR 40 long cells + SB	Sum method	Proportional method
TRBA	0	-0.27°	-0.29°
Nat. hor. emittance	72 pm·rad	66.9 pm·rad	59.2 pm·rad
Energy spread	$0.86\ 10^{-3}$	$1.03\ 10^{-3}$	$1.02\ 10^{-3}$
Mom. comp. factor	$7\ 10^{-5}$	$5.14\ 10^{-5}$	$4.58\ 10^{-5}$
Hor. damp. part. number	1.50780	1.91472	1.93536
Energy loss per cell	49.8 keV	56.3 keV	53.5 keV

Table 3-9 lists the required horizontal shifts of the quadrupoles. A higher horizontal shift is required for the proportional method, which remains below 3.4 mm for the QF4, and 2.2 mm for the QF6 and QF8 magnets. The maximum transverse displacement values are determined by analysis of the full cell assembly drawings for EBS, as shown in Figure 3-30, and should be shortened by 1 mm considering the presence of kapton foils between QF4s and the vacuum chambers, and specific vacuum chambers shapes and positioning of heating wires for the QF6/QF8 magnets in the EBS machine.

This project has received funding from the European Union's Horizon 2020 research and innovation programme under grant agreement No. 871072.

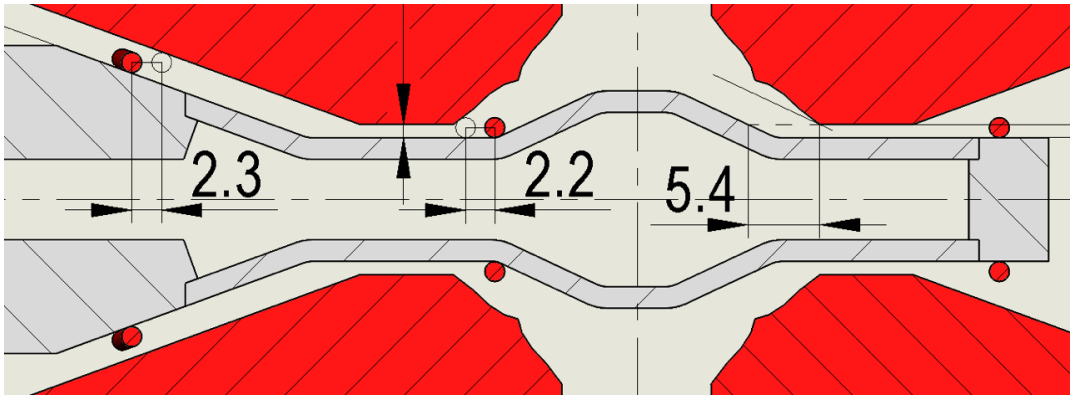

Figure 3-30: Horizontal displacement margin of a QF8 magnet in the EBS storage ring. The maximum horizontal shift theoretically achievable is 2.2 mm.

Table 3-9: Required horizontal shifts for different angular correction methods.

Horizontal shifts per quadrupole	Sum method	Proportional method	maximum allowed
QF4[AE]	0.325 mm	0.348 mm	2.4-3.4 mm
QF4[BD]	0.291 mm	0.311 mm	2.4-3.4 mm
QF6[BD]	1.01 mm	1.08 mm	1.2-2.2 mm
QF8[BD]	1.30 mm	1.40 mm	1.2-2.2 mm

Inhomogeneous distribution of the total reverse bending angle

To find the lowest natural emittance, with an angle adapted to each reverse bend - to reduce the horizontal shift and ensure the lattice remains stable, the total reverse bending angle is randomly distributed among the reverse bending magnets. Each magnet is assigned an angle θ_i, $i \in [1;N]$, with N the total number of reverse bends.

The inhomogeneous distribution is translated into random normalized weights, respecting the cell symmetry. They verify:

$$\forall i \in [1;N], w_i = \theta_i/\mathrm{TRBA},$$
$$\forall i \in [1;N], w_i = w_{N-i+1},$$
$$\sum_i w_i = 1, and\ \forall i, w_i \geq 0.$$

The inhomogeneous angular distribution frees the total reverse bending angle, which optimum was previously limited to the parabolic evolution of the emittance. To fully exploit this knob, multiple scans are conducted, with a fixed relative variation of the TRBA, of $\pm\Delta\mathrm{TRBA} = \pm 0.1$ degree. The number of scans is set at N_{scan}.The symmetric variation in TRBA allows it to go back in angle, following random walk considerations, favoring a low TRBA and low horizontal shifts. Figure 3-31: illustrates the algorithm principle. The scan controls the horizontal damping partition number for sake of longitudinal stability (J_x < 2).

This project has received funding from the European Union's Horizon 2020 research and innovation programme under grant agreement No. 871072.

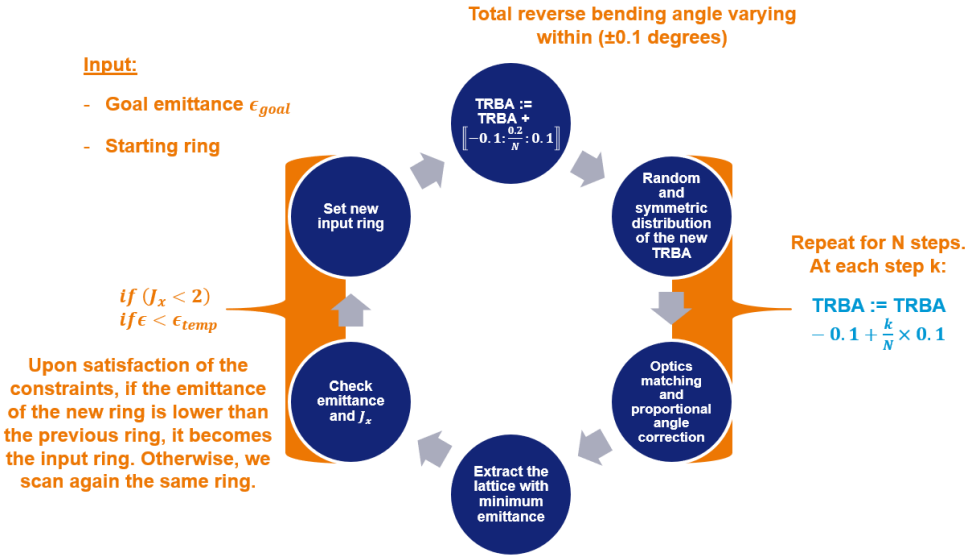

Figure 3-31: Schematic of the implementation algorithm to include inhomogeneously distributed reverse bending magnets in the USSR lattice option with Short Bend.

The angular scan is limited to a fixed number of steps. For each step, the TRBA is scanned linearly in [-0.01; 0.01] degrees. For each total reverse bending angle value, ten random distributions are generated. Optics are matched for each of these 10 lattices and the horizontal emittance and momentum compaction factor are evaluated. A new loop is started from the best solution of the previous step. The lattice of minimum emittance is selected to continue the scan, provided $J_x < 2$. The variation of both the natural horizontal emittance and the momentum compaction factor with the TRBA are displayed in Figure 3-32.

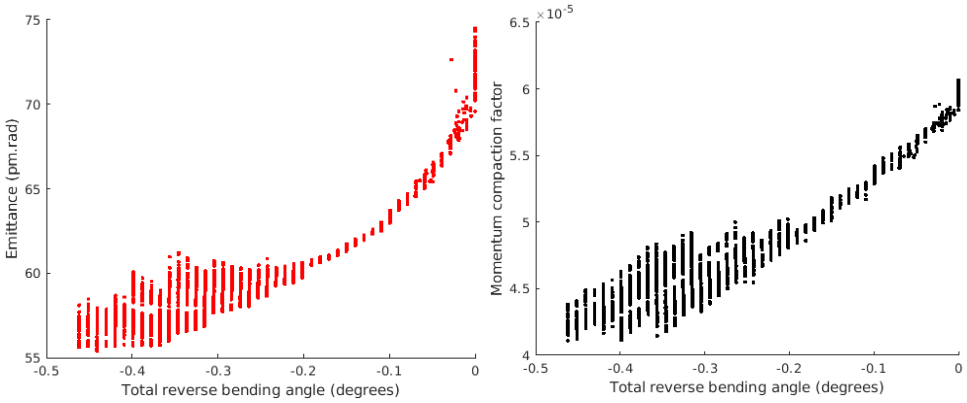

Figure 3-32: Variation of (left) the natural horizontal emittance and (right) the momentum compaction factor during the inhomogeneous implementation of reverse bending angle. The large number of points per angle originates from the random reverse-angle distribution and the two-sided evolution of the TRBA.

Lattice option with horizontal emittance 53.1 pm

After selection of the optimum standard cell option with Short Bend and reverse bending magnets (RB), the injection cells are matched and the ring optics restored. This section lists the general characteristics and analysis of the proposed ring [18].

This project has received funding from the European Union's Horizon 2020 research and innovation programme under grant agreement No. 871072.

Layout and general characteristics

Figure 3-33 displays the Twiss function of the proposed USSR lattice with Short Bend and reverse bends option. Table 3-10 compares the general characteristics of the 40-fold symmetry lattice based on ESRF-EBS cells, the option with a SB at the center of each period and the presented option with SB and RB.

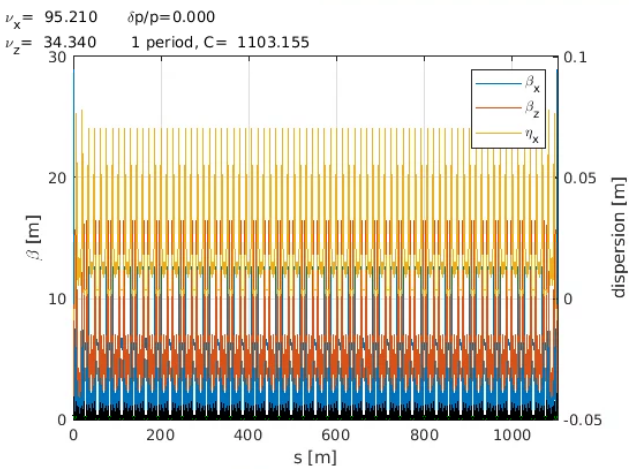

Figure 3-33: Twiss functions and dispersion of the lattice option with reverse bends.

Radiated power

The inclusion of reverse bending magnets has a double effect on the emitted power. First, the restoration of the total angle increases the magnetic field of normal dipoles, thus increasing their radiated power [19]:

$$P_{dip} = e\gamma^4 I_b L/(6\pi\epsilon_0 \rho^2),$$

with e the elementary particle charge, γ the Lorentz factor, I_b the beam current, L the dipole length, ϵ_0 the vacuum permittivity and ρ the bending radius.

Figure 3-34 compares the power emitted per dipole for an electron beam of 200 mA, for the lattice without and with reverse bends. The correction of the reverse bending angle increased the emitted power per standard dipole by at most 8% (DQ1B).

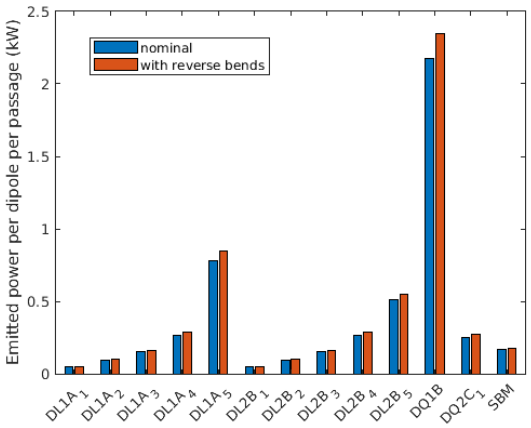

Figure 3-34: Comparison of the emitted power per dipole and per passage for an electron beam of 200mA, for the lattices without (blue) and with reverse bends (orange).

This project has received funding from the European Union's Horizon 2020 research and innovation programme under grant agreement No. 871072.

Table 3-10: Comparison of the lattice parameters.

6 GeV SR parameters	USSR 40 EBS like	USSR 40 long cells + SB	V1-RB
Circumference	1055 m	1103 m	1103.15 m
# cells	40	40	40
# beamlines	34 ID	34 ID + 40 BM	34 ID + 40 BM
nat. hor. emittance	68 pm·rad	72 pm·rad	53.1 pm·rad
vertical emittance	5 pm·rad	5 pm·rad	5 pm·rad
energy spread	$0.85\ 10^{-3}$	$0.85\ 10^{-3}$	$1.04\ 10^{-3}$
mom. comp. factor	$5\ 10^{-5}$	$7\ 10^{-5}$	$5\ 10^{-5}$
bunch length (I=0)	2.7 mm	3.3 mm	3.4 mm
tune	95.21, 33.34	95.21, 33.34	95.21,34.34
chromaticity	12,7.5	7,6	1,5
Energy loss / turn	2.1 MeV	2.0 MeV	2.2 MeV
RF voltage	5.0 MV	5.0 MV	5.0 MV
RF frequency	352.0 MHz	352.2 MHz	352.2 MHz
harmonic number	1241	1296	1296
Max. total current	200 mA	200 mA	200 mA
Z_n/n	0.67 Ohm	0.67 Ohm	0.67 Ohm

Second, the negative bending angle of the reverse bends generates synchrotron radiation pointing to the internal wall of the vacuum chamber. Figure 3-35 lists the emitted power per passage in each reverse bending magnets of the standard cell, considering an electron beam of 200 mA. Such radiation being emitted towards the inner wall of the vacuum chamber will require studying the need for dedicated photon absorbers (or other solutions).

This project has received funding from the European Union's Horizon 2020 research and innovation programme under grant agreement No. 871072.

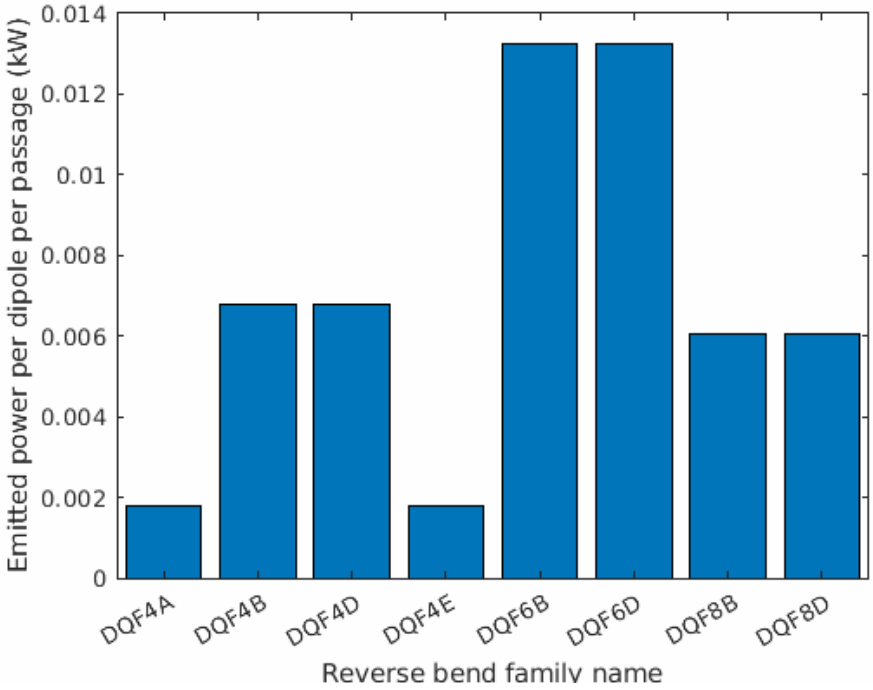

Figure 3-35: Emitted power per dipole and per passage for an electron beam of 200 mA for the considered reverse bending magnets.

Standard cell

A zoom in the standard cell (called as V1-RB), in Figure 3-36, locates the implemented reverse bending magnets: two families under the dispersion bump (QF4) and two families in the cell central region (QF6 and QF8). Dipole field values are presented in Figure 3-37.

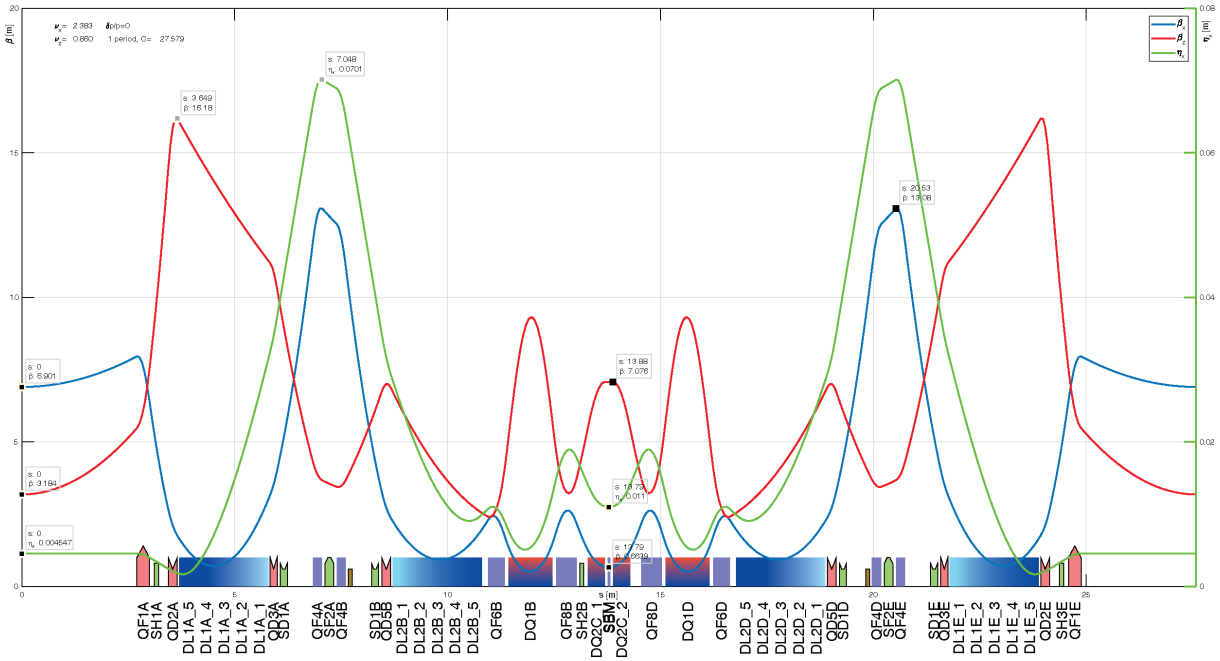

Figure 3-36: Standard cell with Short Bend and reverse bending magnets.

This project has received funding from the European Union's Horizon 2020 research and innovation programme under grant agreement No. 871072.

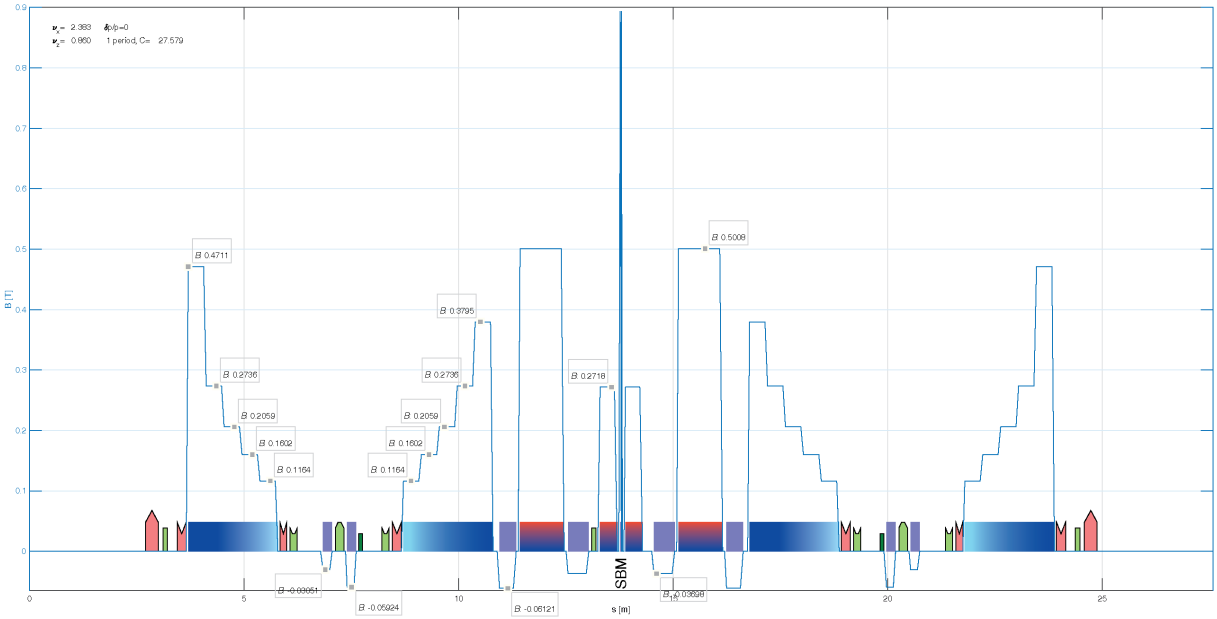

Figure 3-37: Dipole field values for standard cell with SB and RBs.

On the dispersion in the straight section

A small gain in natural horizontal emittance is achievable using the same reverse bends by releasing the condition of the dispersion in the middle of the straight section. Nevertheless, a too large dispersion can increase the beam size at the ID. To control both aspects, the area occupied by the electron beam is evaluated through the effective emittance [17]:

$$\epsilon_{eff} = \sigma_x \cdot \sigma'_x ,$$

with $\sigma_x = \sqrt{\epsilon_x \beta_x + (D_x \sigma_E)^2}$ the electron beam size and $\sigma'_x = \sqrt{\epsilon_x / \beta_x + (D'_x \sigma_E)^2}$ the beam divergence, $\sigma_E = \Delta p / p_0$. Figure 3-38 compares the evolution of the effective horizontal emittance for different dispersion values at the insertion device, on the previous standard cell. As setting different dispersion at the ID changes the dispersion along the cell, the angle of the reverse bending magnets was adjusted at each step, to try and further minimize the natural horizontal emittance. The total angle was restored for each generated ring, as well as the optics.

The dispersion at the entrance of the standard cell was optimized to reduce the effective emittance at the ID. It was decreased from 4.7 mm to 3.8 mm, which gained 1 pm·rad emittance. Such a gain remains negligible when considering intra beam scattering.

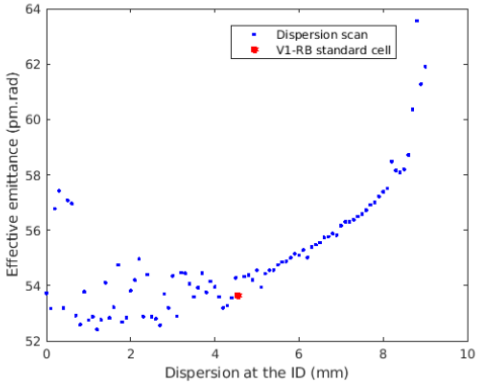

Figure 3-38: Effective horizontal emittance with dispersion at the insertion device. The red dot is the effective emittance of the standard cell before further decrease and matching of the injection cells.

This project has received funding from the European Union's Horizon 2020 research and innovation programme under grant agreement No. 871072.

Beta functions and beam sizes at key locations

Table 3-12 compares the β-functions and the dispersion level of the nominal standard cell and its option with reverse bends, at three different locations. A slight increase of the dispersion in the straight section relieved the dispersion constraints within the lattice, allowing a higher decrease of the horizontal emittance. Nevertheless, the horizontal beam size and effective emittance remain lower for the reverse bend option at both expected source points (SB and ID).

Table 3-12: Comparison of the beta functions and dispersion at three locations of the standard cells, with or without reverse bends.

Parameter	**USSR 40 long cells + SB**	**V1-RB**
	Insertion Device	
β_x	6.9 m	5.79 m
β_y	3.07 m	3.23 m
D_x	1.7 mm	3.8 mm
σ_x	22.3 um	17.9 um
σ'_x	3.2 urad	3.0 urad
ϵ_{eff}	70.2 pm·rad	54 pm·rad
	At the center of the dispersion bump	
β_x	13.2 m	12.4 m
β_y	7.2 m	3.5 m
D_x	8.0 cm	7.0 cm
	At the center of the cell	
β_x	0.37 m	0.69 m
β_y	2.9 m	7.0 m
D_x	7.7 mm	8.7 mm
σ_x	8.3 um	10.9 um
σ'_x	13.9 urad	8.8 urad
ϵ_{eff}	116 pm·rad	96 pm·rad

The change in the dispersion reduced its maximum value at the location of the focusing sextupoles. This decrease, coupled with higher quadrupole strengths and therefore higher natural chromaticities, results in stronger sextupoles. Their gradient is compared to the nominal lattice, for a

This project has received funding from the European Union's Horizon 2020 research and innovation programme under grant agreement No. 871072.

ring chromaticity of (7,6), in Table 3-13. The SD1 sextupole strengths are above the limits imposed by the EBS sextupole design (see Figure 4-5).

Table 3-13: List of the sextupole families and gradients, for chromaticity correction of the full ring at (7,6).

Family name	USSR 40 long cells + SB	V1-RB
SD1[AE]	-2044 $T \cdot m^{-2}$	-2770 $T \cdot m^{-2}$
SF2[AE]	1705 $T \cdot m^{-2}$	2313 $T \cdot m^{-2}$
SD1[BD]	-1343 $T \cdot m^{-2}$	-2692 $T \cdot m^{-2}$

Table 3-14 lists the characteristics of the reverse bending magnets and their corresponding horizontal shift. The main contribution in the emittance reduction comes from the core of the lattice, with a maximum 2 mm shift required.

Table 3-14: List of the reverse bending magnets and their corresponding horizontal shifts of the USSR with Short bend and reverse bending magnets option.

Family name	Length, m	Normalized strength, m^{-2}	Bending angle	Horizontal Shift, mm	Maximum allowed, mm
QF4[AE]	0.212	2.60	-0.019°	0.18	2.4-3.4
QF4[BD]	0.212	2.20	-0.0036°	0.29	2.4-3.4
QF6[BD]	0.388	4.52	-0.068°	2.08	1.2-2.2
QF8[BD]	0.484	4.42	-0.051°	1.91	1.2-2.2

Cell geometry

The angular variation along the cell is perturbed by the introduction of the reverse bends, and the angular correction that follows. Figure 3-39 compares the radial positions of the standard cell with reverse bends with its equivalent without reverse bends. A maximum of 4 mm displacement is expected at the center of the cell.

The strongest contribution to the geometry change comes from the longitudinal gradient dipoles at the edge of the cell. The correction of the total angle increases their field, which results in a stronger bend of the electrons at the beginning of the cell.

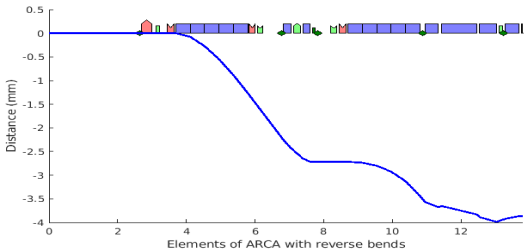

Figure 3-39: Distance between the beam trajectory in the standard cell with reverse bends and without, for the first half of a standard cell.

This project has received funding from the European Union's Horizon 2020 research and innovation programme under grant agreement No. 871072.

Magnet gradients

Table 3-15 compares the gradients of the quadrupoles and sextupoles of the standard cell with Short Bend without and with reverse bends.

Table 3-15: List of the quadrupole families and gradients.

Family name	USSR 40 long cells + SB	V1-RB
QF1[AE]	48.87 T·m^{-1}	**56.25 T·m^{-1}**
QD2[AE]	-56.82 T·m^{-1}	**-66.87 T·m^{-1}**
QD3[AE]	-48.83 T·m^{-1}	**-38.30 T·m^{-1}**
QD5[BD]	-49.89 T·m^{-1}	-51.66 T·m^{-1}
QF4[AE]	52.12 T·m^{-1}	50.03 T·m^{-1}
QF4[BD]	46.71 T·m^{-1}	44.59 T·m^{-1}
QF6[BD]	90.18 T·m^{-1}	90.62 T·m^{-1}
QF8[BD]	92.21 T·m^{-1}	88.21 T·m^{-1}
DQ1[BD]	-38.78 T·m^{-1}	-37.50 T·m^{-1}
DQ2C	-31.09 T·m^{-1}	-31.10 T·m^{-1}

Injection cells

Few adaptations of nominal injection were conducted to match the V1-RB standard cell lattice:

- The same reverse bend angles as the standard cell were implemented in the injection cells. The total angle was corrected using the proportional method[2].
- The dispersion at the ID straight sections was rematched along with the optics.
- The standard cell matching had to be adapted to guarantee convergence of the injection cell optics matching.

Figure 3-40 displays the injection cells of the lattice with reverse bends. Its high beta straight section reaches β_x = 28.86 m. List of the quadrupole families and gradients of the injection cells is pesented in Table 3-16.

[2] Notice that the dipole fields distribution in the injection cell is not the same as for the standard cells. The first two dipoles adjacent to the injection point are specific to this section.

This project has received funding from the European Union's Horizon 2020 research and innovation programme under grant agreement No. 871072.

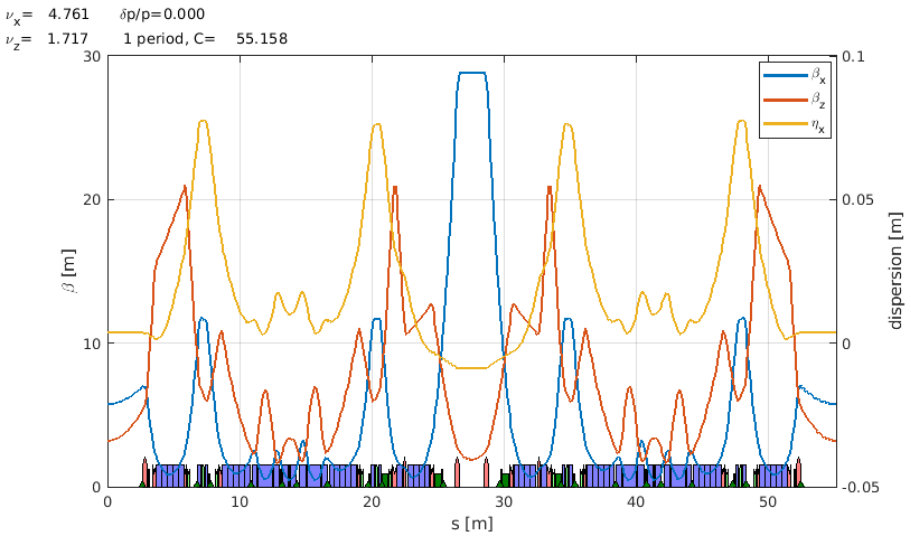

Figure 3-40: Injection cells with Short Bend and reverse bending magnets.

Table 3-16: List of the quadrupole families and gradients of the injection cells. In bold the magnets that require verification of the EBS design either for gradient or position.

Family name	Injection cells of USSR 40 long + SB	Injection cells V1-RB
QF1[IJ]	30.51 T·m^{-1}	18.81 T·m^{-1}
QF1L	48.84 T·m^{-1}	49.68 T·m^{-1}
QF2[IJ]	44.79 T·m^{-1}	**59.23 T·m^{-1}**
QD2L	-56.78 T·m^{-1}	-47.54 T·m^{-1}
QD2[IJ]	-24.54 T·m^{-1}	-33.86 T·m^{-1}
QD3L	-48.79 T·m^{-1}	**-60.55 T·m^{-1}**
QD3[IJ]	-54.76 T·m^{-1}	**-58.01 T·m^{-1}**
QD5[BD]	-48.88 T·m^{-1}	-49.89 T·m^{-1}
QF4L	52.09 T·m^{-1}	52.12 T·m^{-1}
QF4[IJ]	53.41 T·m^{-1}	52.66 T·m^{-1}
QF4[BD]	46.71 T·m^{-1}	47.52 T·m^{-1}
QF6[BD]	90.12 T·m^{-1}	87.82 T·m^{-1}
QF8[BD]	92.15 T·m^{-1}	92.89 T·m^{-1}
DQ1[BD]	-38.75 T·m^{-1}	-38.43 T·m^{-1}
DQ2C	-31.07 T·m^{-1}	-31.09 T·m^{-1}

This project has received funding from the European Union's Horizon 2020 research and innovation programme under grant agreement No. 871072.

Transverse dynamics

Figure 3-41 compares the on-momentum dynamic aperture at the injection point of two lattices: the V4-SB, presented in the previous part and the lattice option with reverse bends. Particles are tracked starting at the injection point for 500 turns for speed reasons, for both full rings with injection cells and the two standard cells alone. Table 3-17 lists the values of the corresponding beta functions.

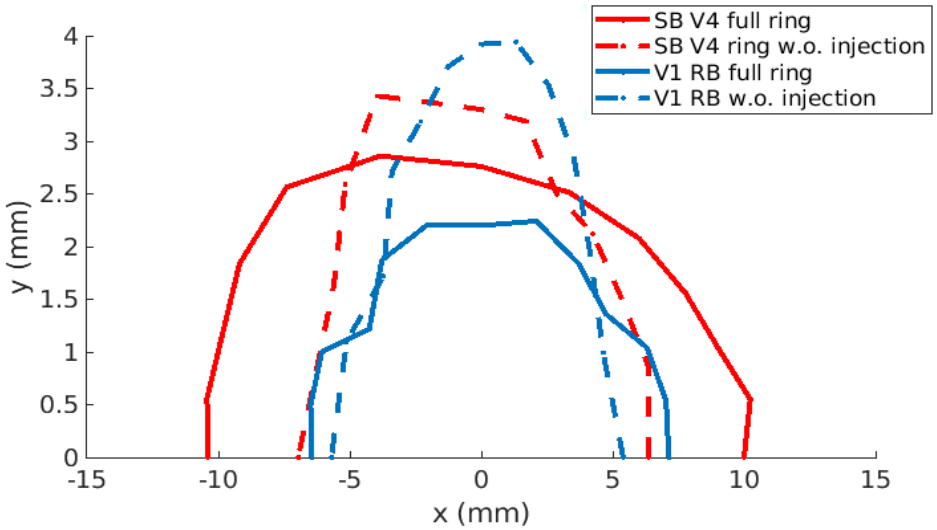

Figure 3-41: On-momentum dynamic aperture tracked for 500 turns for the SB-V4 lattice (in red) and the present option with reverse bends (in blue), for the full ring with injection cells (in plain lines) and the standard cells (in dotted lines).

Table 3-17: Beta functions for on-momentum dynamic aperture comparison.

Lattice	Injection point	Insertion device
V4-SB	β_x=26 m β_y=2.4 m	β_x=6.9 m β_y=3.1 m
V1-RB	β_x=29 m β_y=1.9 m	β_x=5.8 m β_y=3.2 m

The high-β_x injection cells applied to the lattice with reverse bends do not enhance the horizontal transverse acceptance as they should. Tuning of the injection is therefore mandatory to enhance the DA at injection point, with less impact on the Touschek lifetime.

Touschek lifetime

The Touschek lifetime was calculated for three different filling modes, for a vertical emittance fixed to 5 pm·rad and assuming bunch lengthening with current equivalent to the EBS one (Table 3-5). The results are displayed in Table 3-18. The lattice with reverse bends presents a 1.0 h lifetime. Future work will be concentrated on tuning of the injection cells optics and sextupole optimisation to increase the beam Touschek lifetime. Figure 3-42 plots the momentum acceptance along four cells of the ring, after tracking particles for 1024 turns. The minimum local momentum acceptance is of the order of ±1.5%, while for the V4-SB lattice (see below) it is about ±3.5%.

This project has received funding from the European Union's Horizon 2020 research and innovation programme under grant agreement No. 871072.

Table 3-18: Touschek lifetime of the lattice with reverse bends, for three filling patterns.

Filling mode	Total current, mA	Touschek lifetime, h
7/8	200	1.0
16 bunches	92	0.02
4 bunches	40	0.01

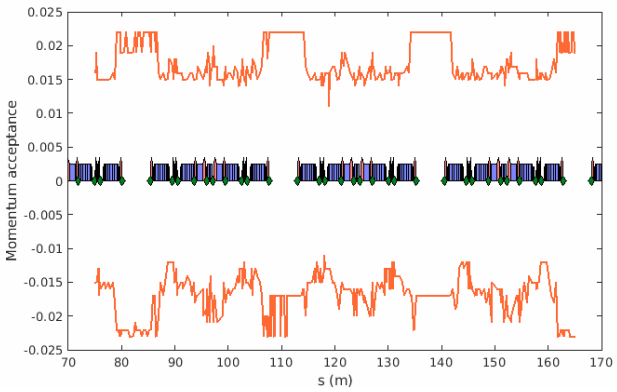

Figure 3-42: Longitudinal local momentum acceptance of the lattice option with RBs.

Chromaticities

A simple scan was conducted to select the optimum chromaticities in terms of lifetime and transverse dynamic aperture. Dynamic aperture was tracked for 512 turns. The Touschek lifetime was calculated assuming the same uniform filling pattern as ESRF-EBS (200 mA in 1296 bunches). The momentum acceptance was tracked for 2000 turns. Figure 3-43 gathers the resulting dynamic aperture area (color) and the Touschek lifetime for the scanned chromaticities (value).

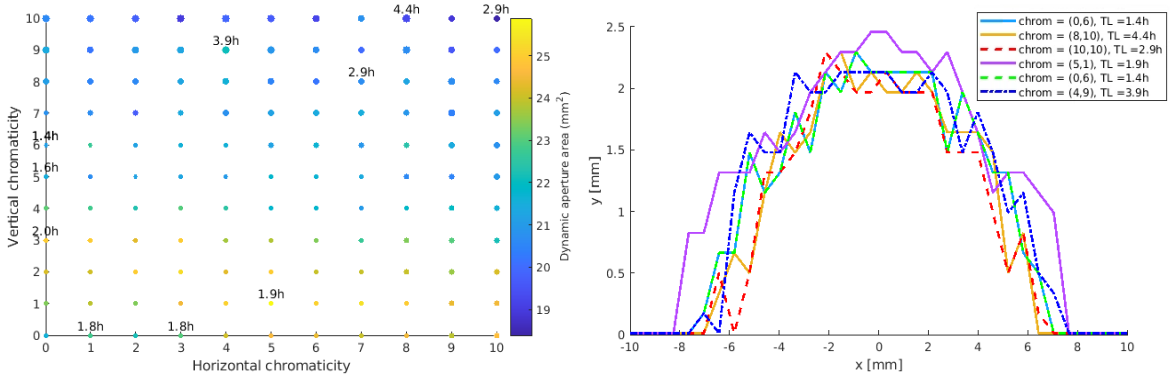

Figure 3-43: Transverse dynamic aperture area (color bar) and Touschek lifetime (point sizes/10) for different chromaticities (left) without errors, some lifetimes are displayed and the corresponding on-momentum dynamic aperture is shown on the rigth.

The best compromise found between Touschek lifetime at high current and on-momentum dynamic aperture at the injection point was found for the chromaticity (4,9), which maximizes the product of the two objectives, and remains close to the (7,6) chromaticities of V4-SB.

This project has received funding from the European Union's Horizon 2020 research and innovation programme under grant agreement No. 871072.

This final Touschek lifetime remains limited due to the unoptimised injection cells. Such a scan should be reconducted after the rematching and minimization of the impact of the injection cells on the beam lifetime.

MOGA to optimize the cell optics

Multi-objective genetic optimization ([20]) is presently running for the standard cell optics, to maximize both its on-momentum dynamic aperture and the Touschek lifetime. The optimisation generates 16 individuals for each 30 generations and uses the following knobs:

- the vertical beta function and its derivative at the location of the focusing sextupoes
- the horizontal beta function in the middle of the straight section
- the phase advance between the sextupoles.

The dispersion and the horizontal beta function at the ID are kept constant to ease the matching of the injection cells. Additional optimisations will also include sextupoles and octupoles tuning. Figure 3-44 illustrates the variation of the on-momentum dynamic aperture and the Touschek lifetime during the optimization. The sizes of the dots monitor the evolution of the natural horizontal emittance, as a means of post-optimisation control.

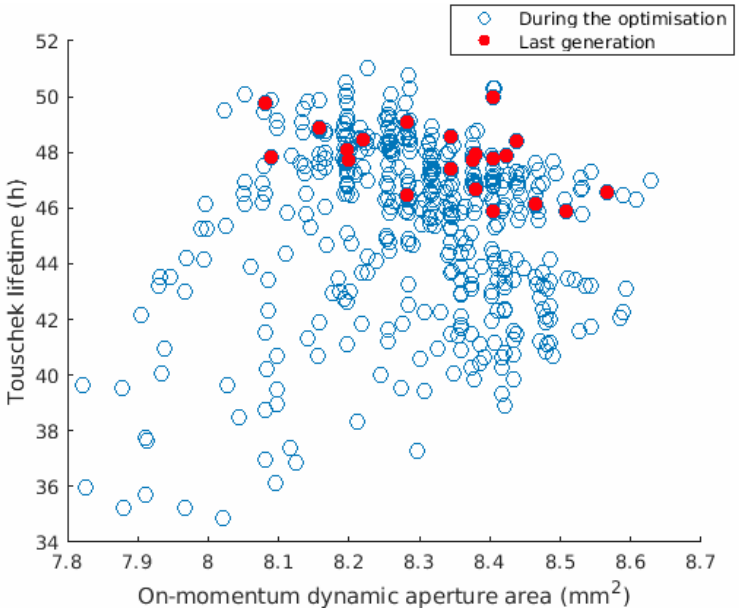

Figure 3-44: Evolution of the on-momentum dynamic aperture and Touschek lifetime during the MOGA optimization. The size of the dots correspond to the natural horizontal emittance of the standard cell.

The averaged Touschek lifetime for a 40-fold symmetry ring remains higher than 35 h, and can reach close to 48 h for the optimized cells. This result stresses the need for adapted injection cells which will be retuned in the future.

Collective effects

From measurements of the microwave and the transverse mode coupling instability (TMCI) thresholds conducted on the ESRF-EBS machine [21], those thresholds can be estimated in the future USSR storage ring lattices by scaling the measured value to the new lattices.

This project has received funding from the European Union's Horizon 2020 research and innovation programme under grant agreement No. 871072.

Table 3-19 gathers the relevant parameters for the three compared lattices: the ESRF-EBS, the nominal USSR lattice with short bend, and its option with reverse bending magnets.

Table 3-19: Microwave and TMCI thresholds of the USSR lattice with Short Bend and reverse bends, after scaling with regards to ESRF-EBS.

Parameters		**EBS**	**V1-RB**
Energy		6 GeV	6 GeV
Circumference		844 m	1103 m
mom. comp. factor		$9\ 10^{-5}$	$5.0\ 10^{-5}$
Energy loss / turn		2.5 MeV	2.2 MeV
energy spread		$0.95\ 10^{-3}$	$1.0\ 10^{-3}$
RF voltage		6.5 MV	5.0 MV[3]
bunch length (I = 0)		2.9 mm	3.3 mm
Harmonic number		992	1296
Synchrotron tune		0.00368	0.00277
Max. total current		200 mA	200 mA
Z_n/n			0.67 Ohm
Instability thresholds			
TMCI [21]	measured	0.44 mA	0.29 mA*
	simulated	0.53 mA	0.34 mA*
Microwave instability	measured	1.4 mA	0.76 mA*
	simulated	3 mA	1.6 mA*

*the values were scaled with regards to the ESRF-EBS measured and simulated thresholds.

In spite of a lower momentum compaction factor, the lattice option with reverse bends scales with a higher estimated threshold for both the microwave and the mode coupling instabilities than its nominal version.

Error studies

The same alignment errors achieved for the ESRF-EBS were implemented in the lattice version with short bend and reverse bending magnets. The values used for simulations are presented in

[3] A new optimum might be found, adapted to the RB option.

This project has received funding from the European Union's Horizon 2020 research and innovation programme under grant agreement No. 871072.

Table 3-3, using the same correction protocol as it was described. Figure 3-45 compares the dynamic aperture of the lattices with errors and correction with the lattice without errors.

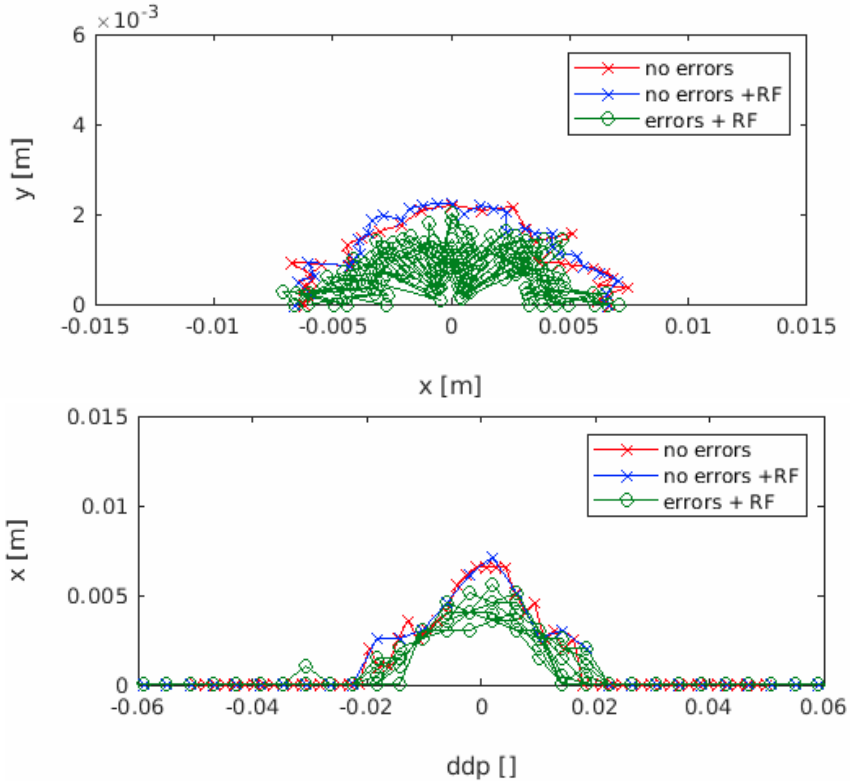

Figure 3-45: Dynamic aperture for the lattices with errors and correction. The red and blue lines refer to the perfect lattice.

Several seeds with errors provide dynamic apertures with points (green circles) very close to zero and the injection efficiencies give reasonable values but with a large error bar (top up e-linac with photo-gun: 88.3 ± 21%) as in the region of injection the dynamic aperture is different from zero for some of the seeds tested.

These observations, together with the low estimated lifetime (~1 h in uniform mode), makes this lattice not ready for operational purposes at the moment. Further studies will be needed and are already planned for the future. In particular the research activities will target the injection cell optics that have shown to have a negative effect on the lattice at the present status (see Figure 3-41) and further optimization of the cell as already started with the MOGA runs presented in the sections above.

Additions on lattice options with RBs

In addition to the above lattice option with RBs, it is worth mentioning that two more options were considered. Here we temprorarilly switched off SB. One of it is presented in Figure 3-46.

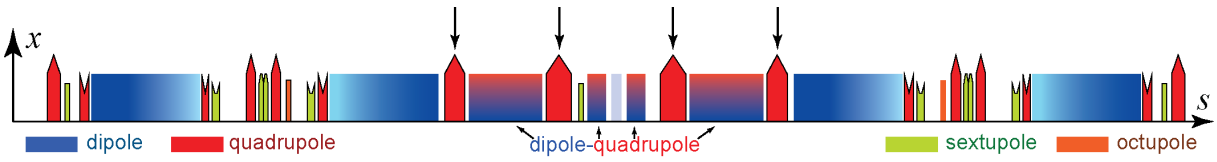

Figure 3-46: Baseline H7BA lattice layout with selected quads.

This project has received funding from the European Union's Horizon 2020 research and innovation programme under grant agreement No. 871072.

Marked quadrupoles were slightly shifted on the same distance from beam orbit and act as reverse bends [22]. Lattice optimization was carried out by means of MADX, AT, Pyhton. After all gradients and dipole fields were rematched in order to obtained stable optics and equilibrium horizontal emittace lower than 70 pm we found dependence of emittance value on the shift of marked quadrupole (bending angle). This dependence is presented in Figure 3-47 (compare with Figure 3-29). Corresponding dependence of horizontal damping partition number J_x (from Robinson's theorem) on bending angle of marked quadrupoles is shown in Figure 3-48. Note, that four marked quads have the same bending angle.

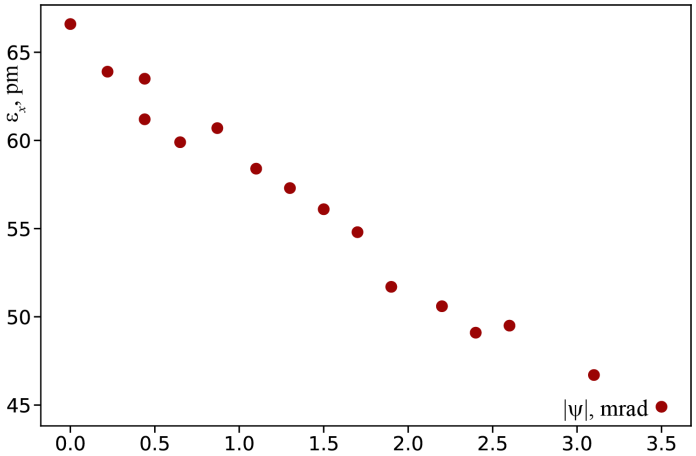

Figure 3-47: Dependence of emittance value on the bending angle of quadrupole.

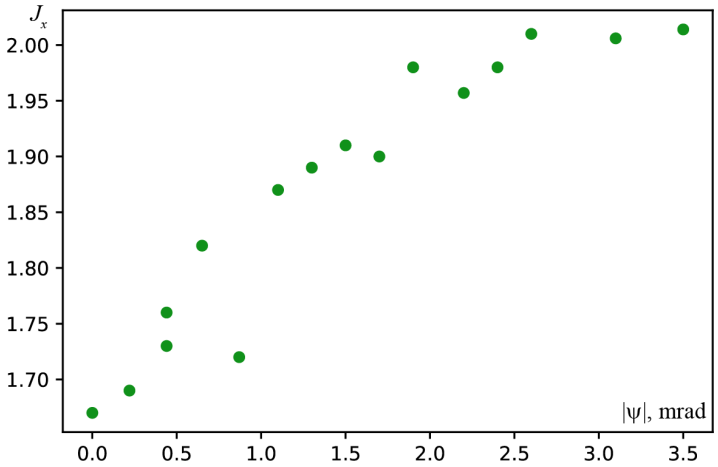

Figure 3-48: Dependence of J_x value on the bending angle of quadrupole.

From this figures one can find that ε_x value lower than 50 pm·rad corresponds for $|\psi|$ values greater than 2 mrad and, consequently, J_x values closed to 2. For example, DA for the standard cell of the lattice with ε_x = 55 pm (J_x = 1.9) is presented in Figure 3-49. As one can see, DA is rather small to use off-axis injection in this case. Thus, on-axis injection should be considered for the given case of introducing the reverse bends.

This project has received funding from the European Union's Horizon 2020 research and innovation programme under grant agreement No. 871072.

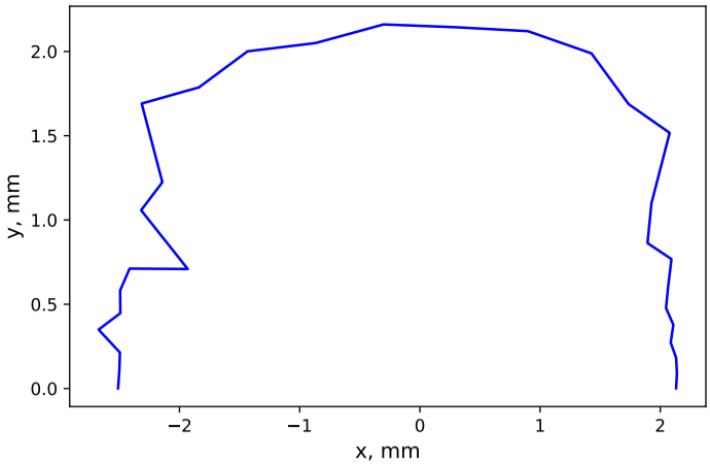

Figure 3-49: DA for the lattice option with ε_x = 55 pm.

A graph of a dependence of absolute value of closed orbit shift on absolute value of shift of RB with respect to its optical axis is presented in Figure 3-50. It follows that possible Δx value is lower than 0.7 mm because of horizontal dimension of vacuum chamber cross section. That dimension is supposed to be equal to 16.5 mm for the cell central region. In turn, this means that $|\psi|$ value is less than 1.2 mrad and, in accordance with Figure 3-47, ε_x is greater than 60 pm.

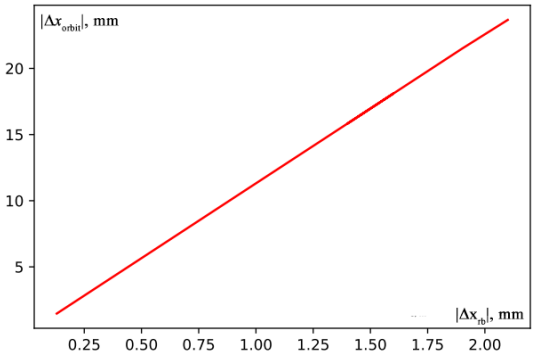

Figure 3-50: Dependence of absolute value of closed orbit shift on absolute value of RB shift.

Another one use of anti-bends (reverse bends) have been investigated. We studied the influence of different quads families on the equilibrium horizontal emittance and found that the main influence is of QF8. Thus, in contrast to the described above way here we used “pure” RB. For the one of the discussed options each QF8 quad was arranged by a pair of rather short RBs and two additional were placed between two adjacent LGB magnets as it is illustrated in Figure 3-51. Note, that in this case we used updated lattice, namely, that has the sliced central DQ2 magnet of the baseline lattice on two parts with drift space for short bend placement. Machine functions for this standard cell are shown in Figure 3-52. As one can see, optics is the same as for baseline lattice. *B*-field distribution of the magnets on the orbit along standard cell is presented in Figure 3-53. The length of the RB1 is 40 cm, and of the RBQF8 is 6 cm, that is comparable with the length of short bend for the baseline lattice option. The ring based on the suggested standard cells potentially can have equilibrium horizontal emittance value is equal to 52 pm. All quads gradients do not exceed threshold values for the quads of the ESRF-EBS main ring. The cell length is 26.61 m, momentum

This project has received funding from the European Union’s Horizon 2020 research and innovation programme under grant agreement No. 871072.

compactification factor is $4.01 \cdot 10^{-5}$, tuned chromaticities are 5 (horizontal) and 7 (vertical). Unfortunately, for this option there is no finite DA.

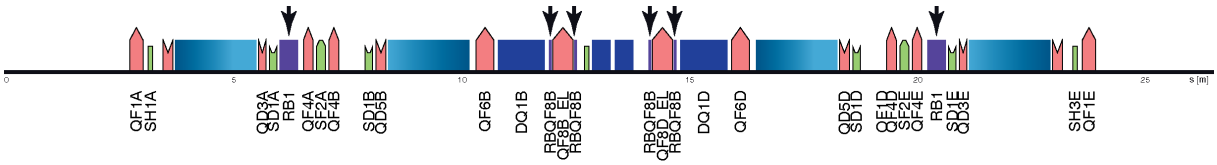

Figure 3-51: The first considered lattice option with “pure” reverse bends.

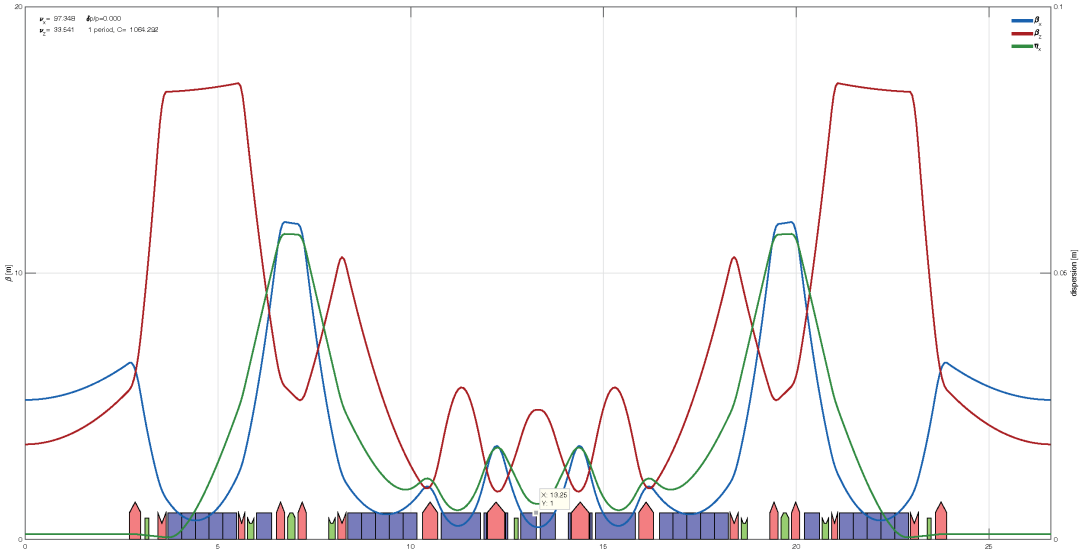

Figure 3-52: Machine optics for the first option with “pure” reverse bends.

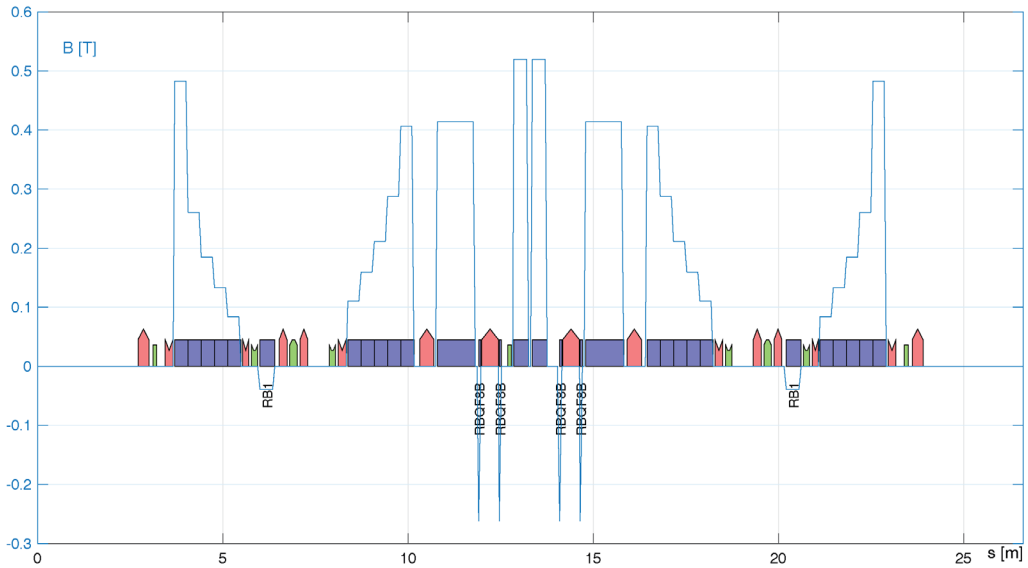

Figure 3-53: Machine optics for the first option with “pure” reverse bends.

4 Vacuum system

Because of the lattice design results vacuum chambers will be redesigned, namely, chambers no. 2 and 13 for DL1, QD2, and QD3, no. 5 and 9 for DL2, no. 6 and 8 for DQ1, QF6 and QF8, as well as chamber no. 7 for SB and DQ2. Chambers of ESRF-EBS project are considered as a prototype. The

This project has received funding from the European Union’s Horizon 2020 research and innovation programme under grant agreement No. 871072.

influence of storage ring lattice, geometric dimensions and beam parameters on the vacuum conditions in SR-source prototype chambers is studied. The geometric model of the storage ring chamber designed for simulation is considered. The simulation of the radiation flux parameters generated by the charged particles passing through the section of the vacuum chamber has been performed. The technique of calculating the parameters of SR and photostimulated desorption by means of Synrad+ and Molflow+ codes is applied [23, 24]. Here all results concerns baseline lattice option with SB.

The circumference of the storage ring includes identical sections with identical vacuum chambers. The pumping system consists of getter-ion vacuum pumps and pumps (cartridges) based on non-evaporated getters. Some sections of the vacuum tract are internally coat with a non-evaporated getter (straight section of built-in devices and adjacent outer chambers). Each element of the vacuum system corresponds to a certain coefficient of desorption or absorption of residual gas molecules. The calculation model included a set of cameras of the standard section, for reasons of symmetry, the beginning and end of the model were located along the centers of linear sections on both sides of the cameras.

The main source of gas in the system is synchrotron-stimulated outgassing, primarily from the surface of built-in SR absorbers. They are made from a copper alloy (for example CuCrZr) and water-cooling is provided in their design. Some parts of the surface of the straight chamber and the first chamber following it are also subject to the generation of stimulated gas flows. These gas loads are compensate by the pumping effect of the getter coating inside the chambers.

It is necessary to determine the relationship of changes in SR parameters with new requirements for radiation absorbers. Approaches to determining the characteristics of the radiation flux in the storage ring of the SR-source are considered. For SR absorbers, the level of gas desorption varies depending on the absorbed power from 10^{-9} to 10^{-7} mbar l/s/cm^2. Changing the circumference of the storage ring will lead to a change in the SR radiation within the individual vacuum chambers. The result of modeling the growth of the absorbed power of SR confirms the leading role of stimulated desorption from the surfaces of absorbers in comparison with the background thermal gas load (Figure 4-1). For further consideration of the parameters of the vacuum system, estimates of the SR flux distribution along the vacuum chambers and the parameters of the absorbers are required.

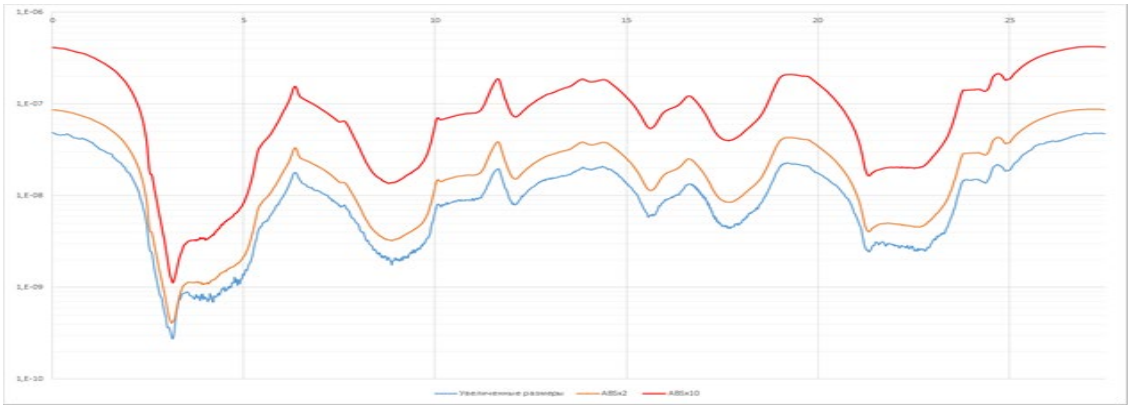

Figure 4-1: Simulation of the pressure growth in the system with the heat load on the absorbers increase and the level of outgassing flow by two (orange) and ten (red) times.

The calculation of the SR and photostimulated desorption parameters can be performed using the Synrad+ module [23, 25]. Using the Monte Carlo method, the program calculates the SR parameters

This project has received funding from the European Union's Horizon 2020 research and innovation programme under grant agreement No. 871072.

(radiation flux, power and spectrum) incident on the chamber walls. Used in the same software package with Molflow+ it is possible to transfer the obtained SR distribution into a gas desorption flow from the inner surface. Thus, it is possible to define the influence of changes in the parameters of the optical system on the vacuum level in the designed installation.

The method for calculating photodesorption using Synrad + has been tested. The calculation model is consider on the example of chamber № 2 of the period of the ESRF-EBS [26] storage ring. A model of the chamber is constructed and the specified parameters of the beam and magnet system are add to it.

The influence of the SR power on the gas desorption from absorbers from this area was studied. Using Optics Builder [27], the configuration of magnetic fields in the form of a sequence of magnets and drift sections in the model was specify. Synchrotron radiation was generated by an electron beam with an 6 GeV energy and 200 mA current. For all SR absorbers located in the selected area, the distribution of the absorbed SR flux was obtain. The absorbed power density was up to 160 W/cm^2, and for individual absorbers it raised up to 278 W/cm^2. The simulation results of the incident SR were exported from Synrad+ to Molflow+, and the values of stimulated desorption from the surface of absorbers for a dose of 100 Ah were calculated. The gas desorption level for these surfaces was $8 \cdot 10^{-8}$ - $6 \cdot 10^{-7}$ mbar·l/s/cm^2. The gas desorption level for the other sections of the vacuum chambers was equal to 10^{-11} mbar·l/s/cm^2.

The simulation results were compare with the characteristics of the prototype. Similar values are obtain, which practically coincide within orders of magnitude (Table 4-1).

Table 4-1: Comparison of the calculated desorption level with the prototype for a dose of 100 Ah.

Absorber	EBS, mbar·l/s	Model, mbar·l/s
ABS CH2-1-1	1.05E-07	8.2E-08
ABS CH3-1-1 Crotch	6.39E-07	9.9E-07
ABS CH4-1-1	3.94E-07	1.7E-07
ABS CH5-1-1	4.03E-07	6.2E-07
ABS5-1-1 H9	1.07E-08	1.3E-08
ABS5-1-1 H11	3.47E-08	9.6E-08

The beam emittance decrease in the designed facility should be lead to the power grows of radiation flux on the vacuum chambers walls. To evaluate this change, using the Synrad+ program, we calculated the characteristics of the generated radiation by the bending magnet of camera No. 2 (DL1) in the projected installation and in the prototype when operating at nominal parameters (Table 4-2):

Table 4-1: Beam parameters.

	EBS	Model
Energy, GeV	6	6
Current, mA	200	200
Emittance, pm·rad	132	69

This project has received funding from the European Union's Horizon 2020 research and innovation programme under grant agreement No. 871072.

The characteristics of the bending magnet sections have been change in addition to the changes in emittance (Table 4-3).

Table 4-3: Bending magnet DL1.

Part	EBS		Model	
	Length, m	Field, T	Length, m	Field, T
DL1-1	0,380	0,6248	0,427	0,7891
DL1-2	0,350	0,4113	0,427	0,4631
DL1-3	0,357	0,3017	0,427	0,3514
DL1-4	0,365	0,2267	0,427	0,2759
DL1-5	0,372	0,1673	0,427	0,2036

The beam generated total radiation power by passing through the magnetic field was calculate for each variant. A rectangular 80x25 facet, located 50 mm from the exit from the magnet (Figure 4-2), absorbed the received radiation.

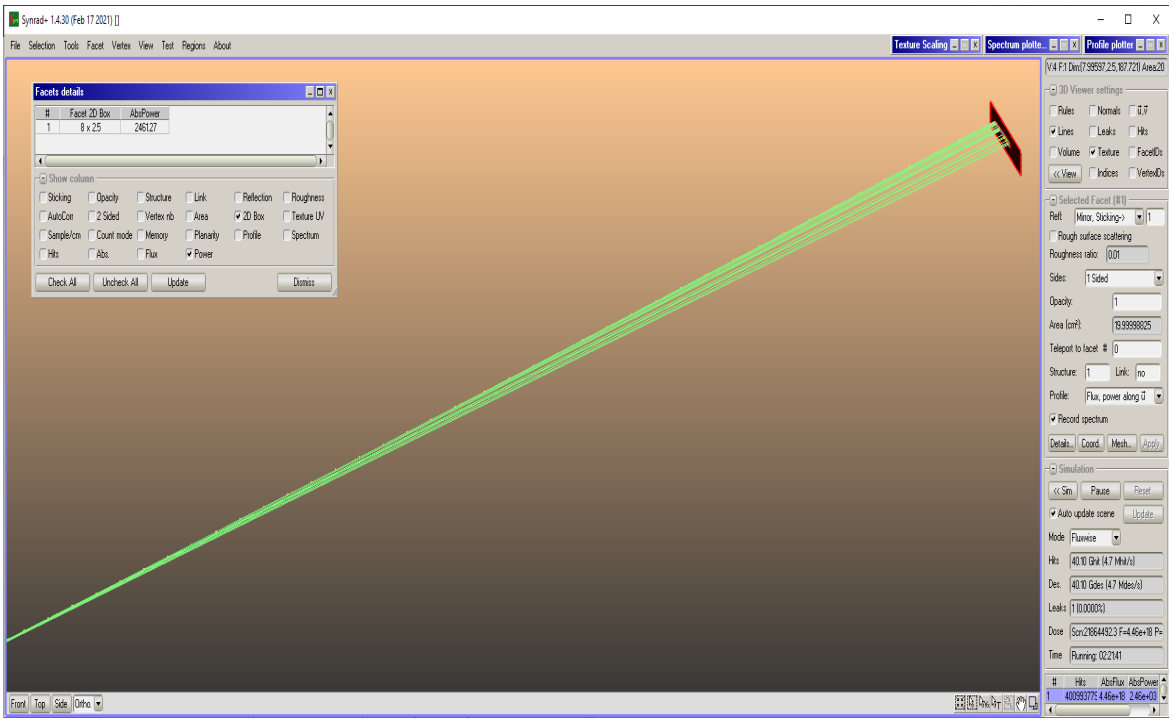

Figure 4-2: Computation model for determining the absorbed radiation power.

The results of the density and SR spectrum computing for the prototype and for the developed SR source model are present in the Figures 4-3 - 4-6.

This project has received funding from the European Union's Horizon 2020 research and innovation programme under grant agreement No. 871072.

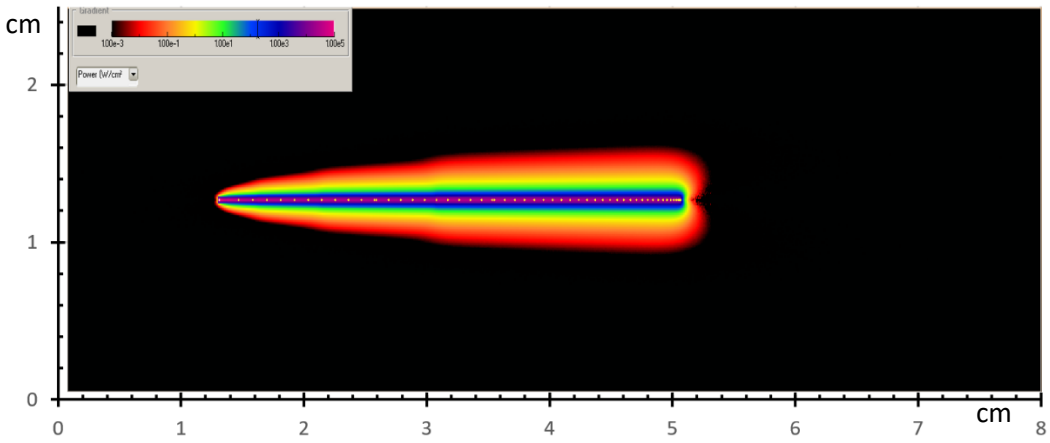

Figure 4-3: Absorbed radiation of DL1 EBS magnet.

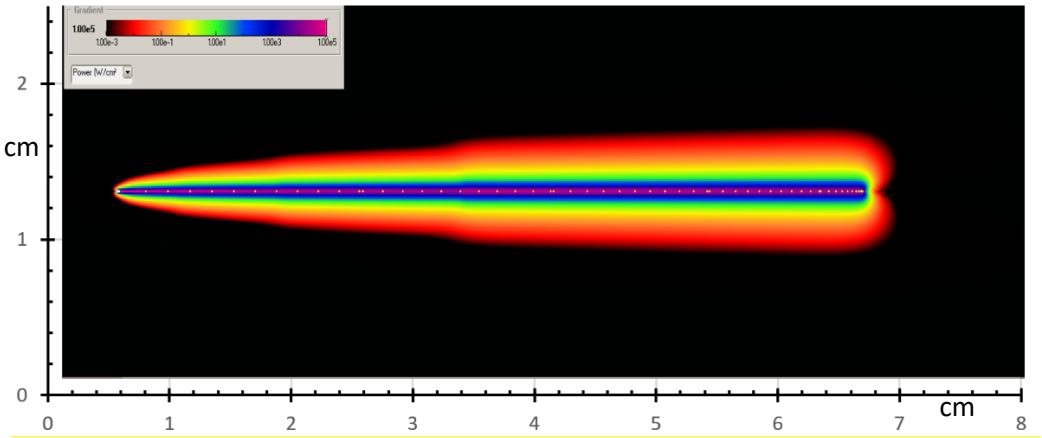

Figure 4-4: Absorbed radiation of DL1 magnet in the designed system

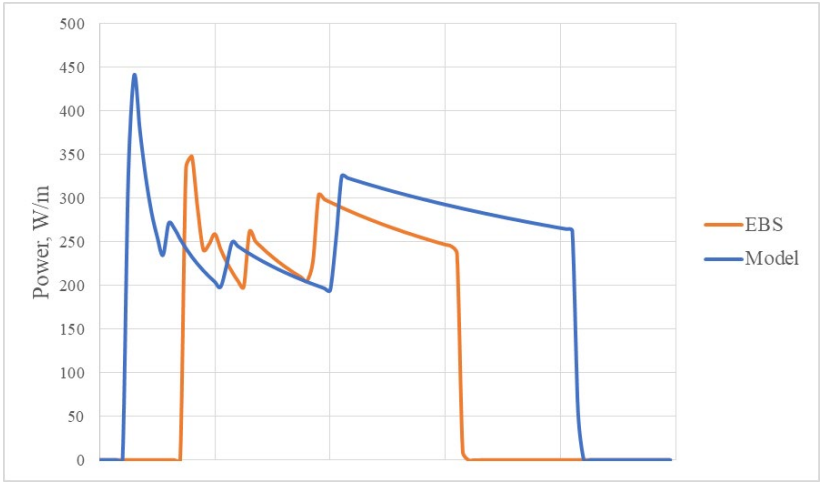

Figure 4-5: Linear distribution of absorbed power.

This project has received funding from the European Union's Horizon 2020 research and innovation programme under grant agreement No. 871072.

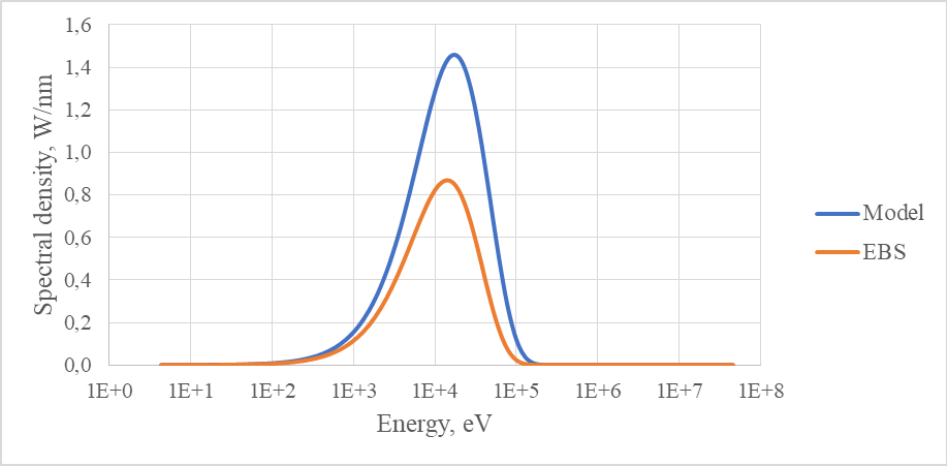

Figure 4-6: Incident radiation spectrum

Comparison of the obtained results with a similar calculation for the ESRF-EBS source showed that an increase in the length of the section and the magnitude of the magnetic field in the sectors of the magnet, together with a decrease in the beam emittance, led to an increase in the horizontal angle of radiation and to an increase in power. In addition, did not change its spectrum. The total SR power changed from 2460 W to 4200 W. Taking into account, it is necessary to clarify the parameters of the absorbers for the projected storage ring device.

Modification of the magnet, vacuum systems elements, beam parameters will also change the conditions for the distribution of SR in the new geometry. A new calculation of the distribution of SR fluxes over the inner surfaces of the chambers will be required. It will be necessary to design a new structure for the absorbers in the chambers, changes in their design under these conditions.

Taking into account the modeling results it will be possible further to consider changes in the stimulated gas load inside the chambers. All these changes may require correction of pumping systems, pumps location and design of new NEG areas to absorb these gas flows.

At the next stage of the development of the SR source project, the magnet system was corrected again. For the bending magnets, the changes consisted in a magnet fields decrease with a slight reduction of magnet length. Comparison of the previous and current versions of dipole magnets of the same period are shown in Table 4-4.

The change in the magnetic structure resulted in an insignificant change in the optical functions. It follows that the amplitude of changes in the β_y function has increased on the bending magnets for the updated lattice version in compare with discussed in 2020 year.

The changes were taken into account in the model and the SR calculation was performed for one period. To calculate the radiation power, an incident radiation monitor was placed after each bending magnet. It is a 50x10 rectangular face located 50 mm from the exit of the magnet (Figure 4-7) in a perpendicular plane to the beam.

The total SR power was 9752 W and the maximum energy density reached 5128 W/cm^2 for the DQ1B magnet. The power density distribution for each monitor is shown in Figure 4-8 and Figure 4-9 and in Table 4-5.

This project has received funding from the European Union's Horizon 2020 research and innovation programme under grant agreement No. 871072.

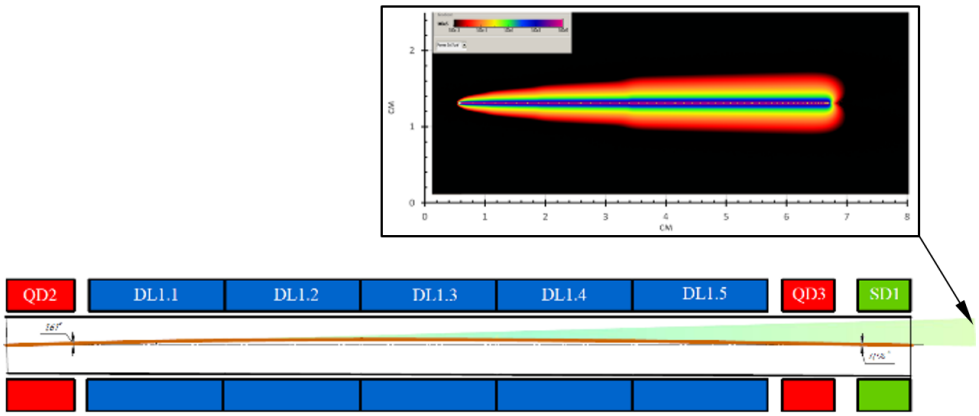

Figure 4-7: Scheme for the SR flow parameters calculating.

Table 4-4: Bending magnets.

Designation	Lengths, m			Magnet field, T		
	previous	next	Δ	previous	next	Δ
2 chamber						
DL1A_5	0,427	0,418	-0,009	0,7891	0,4536	-0,34
DL1A_4	0,400	0,418	0,018	0,4631	0,2634	-0,20
DL1A_3	0,427	0,418	-0,009	0,3514	0,1983	-0,15
DL1A_2	0,427	0,418	-0,009	0,2759	0,1542	-0,12
DL1A_1	0,427	0,418	-0,009	0,2036	0,1120	0,09
5 chamber						
DL2B_1	0,427	0,418	-0,009	0,2036	0,1120	-0,09
DL2B_2	0,427	0,418	-0,009	0,2759	0,1542	-0,12
DL2B_3	0,427	0,418	-0,009	0,3514	0,1983	-0,15
DL2B_4	0,427	0,418	-0,009	0,4631	0,2634	-0,20
DL2B_5	0,427	0,418	-0,009	0,7891	0,3654	-0,42
7 chamber						
DQ2C_1	0,400	0,400		0,3918	0,2617	-0,13
SBM	0,049	0,049		0,8602	0,8601	
DQ2C_2	0,400	0,400		0,3918	0,2617	-0,13
8 chamber						
DQ1D	1,647	1,028	-0,620	0,56696	0,4822	-0,08
9 chamber						
DL2D_5	0,487	0,418	-0,069	0,7891	0,3654	-0,42
DL2D_4	0,487	0,418	-0,069	0,4631	0,2634	-0,20
DL2D_3	0,487	0,418	-0,069	0,3514	0,1983	-0,15
DL2D_2	0,487	0,418	-0,069	0,2759	0,1542	-0,12
DL2D_1	0,487	0,418	-0,069	0,2036	0,1120	-0,09
13 chamber						
DL1E_1	0,487	0,418	-0,069	0,2036	0,1120	-0,09
DL1E_2	0,487	0,418	-0,069	0,2759	0,1542	-0,12
DL1E_3	0,487	0,418	-0,069	0,3514	0,1983	-0,15
DL1E_4	0,487	0,418	-0,069	0,4631	0,2634	-0,20
DL1E_5	0,487	0,418	-0,069	0,7891	0,4536	-0,34

This project has received funding from the European Union's Horizon 2020 research and innovation programme under grant agreement No. 871072.

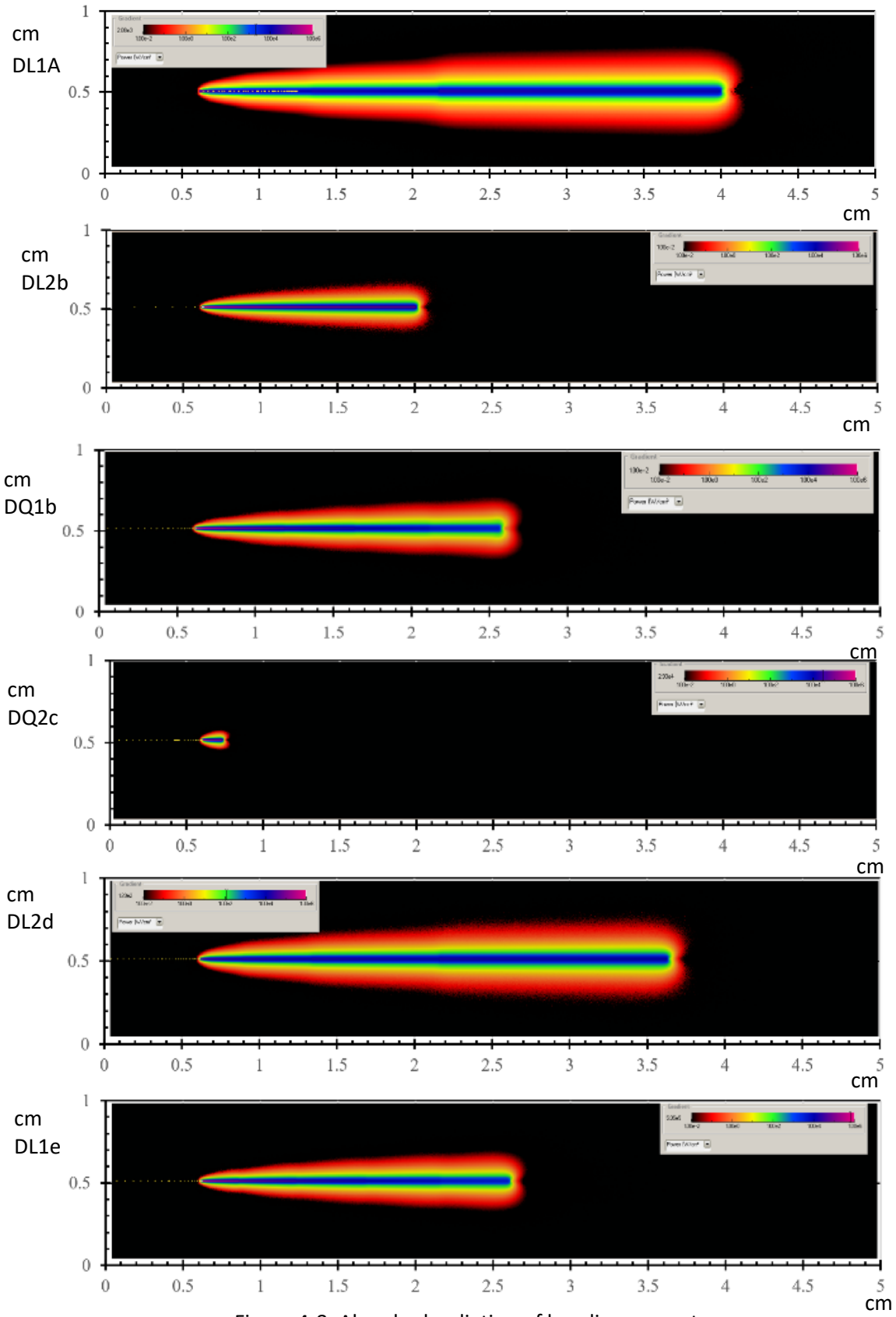

Figure 4-8: Absorbed radiation of bending magnets.

This project has received funding from the European Union's Horizon 2020 research and innovation programme under grant agreement No. 871072.

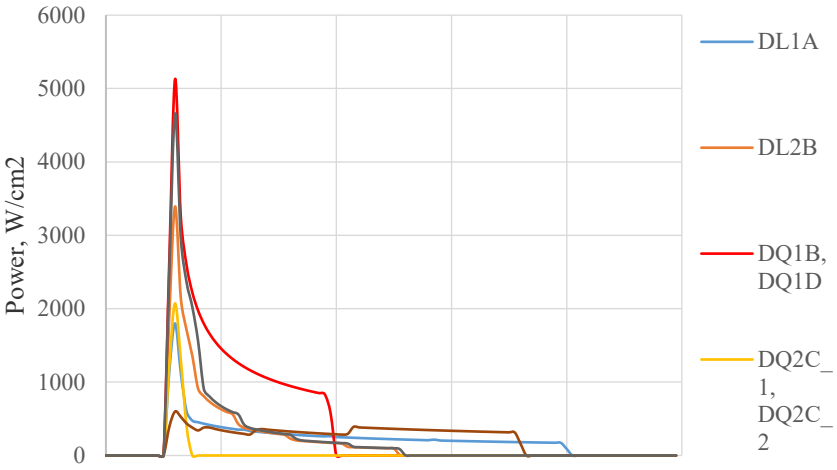

Figure 4-9: Linear distribution of absorbed SR power.

Table 4-5: Characteristics of generated by bending magnets SR and photostimulated desorption.

Designation	Power, W	Desorption, mbar·l/s
DL1A	1066,4	$8{,}0\cdot10^{-7}$
DL2B	1064,5	$4{,}0\cdot10^{-7}$
DQ1B	2182,7	$2{,}7\cdot10^{-7}$
DQ2C_1	250,3	$2{,}0\cdot10^{-8}$
SBM	350,8	$2{,}6\cdot10^{-9}$
DQ2C_2	250,3	$2{,}0\cdot10^{-8}$
DQ1D	2182,7	$2{,}7\cdot10^{-7}$
DL2D	1064,1	$7{,}0\cdot10^{-7}$
DL1E	1339,8	$4{,}0\cdot10^{-7}$
summ	9752	$2{,}9\cdot10^{-6}$

Comparing the calculation results with the previous versions, we can see a decrease in the SR power for the DL1 magnet due to an increase in the radius of rotation of the electron beam with a decrease in the magnetic field (Table 4-6). A similar decrease can be expected in other dipole magnets. Taken together, this should have a positive effect on vacuum conditions, reducing SR-stimulated desorption.

Table 4-6: Characteristics of a section with DL1 magnet in different versions.

	EBS-ESRF	Model	
		baseline	updated
Magnet field, T	0,167-0,625	0,204-0,789	0,112-0,454
Length, m	1,83	2,11	2,09
Trajectory radius, m	32,03-119,62	25,36-98,30	44,13-178,62
SR power, W	2458	4198	1066

The results of calculating of the incident SR were exported from Synrad+ to Molflow+. The flux of stimulated desorption from the irradiated surfaces was calculated at a radiation dose of 100 Ah. The

This project has received funding from the European Union's Horizon 2020 research and innovation programme under grant agreement No. 871072.

yield of molecules (the number of desorbed molecules per incident photon) was taken for copper from the simulation program data [28]. The calculated level of gas desorption of these surfaces was $4 \cdot 10^{-10}$ - $1.4 \cdot 10^{-7}$ mbar · l/s/cm^2 (Table 4-4). The level of residual desorption flow for the remaining sections of the vacuum chambers is 10^{-11} mbar l/s/cm^2. As a result, the SR stimulated dynamic gas flow is expected to be $3 \cdot 10^{-6}$ mbar·l/s. This is roughly corresponds to the gas loads for the prototype ESRF vacuum system.

The obtained data of modeling the distribution of the absorbed power of the radiation flux and the expected values of the gas load from the surfaces will further useful to consider the configurations of the absorbers and to determine the parameters of the vacuum system for pumping out the SR-source storage ring chambers.

5 Magnets

It was decided by our community that all magnets for the updated baseline lattice version with short bend will be the same as for ESRF-EBS.

Replacement of moderate gradient quadrupoles adjacent the injection point

For USSR it is possible to use standard quadrupoles design as for the moderate gradient quadrupoles (QD2, QF4, QD5 which are 0.212 m long) without consequences rather than as for EBS lattice. The quadrupoles are shorter and can be placed such that the septum straight section (center of the injection straight section) is unaffected, thus approaching the center of QF1I and QF1J to the injection point, and providing a small increase of horizontal beta functions at the injection point (see Figure 5-1 and 5-3).

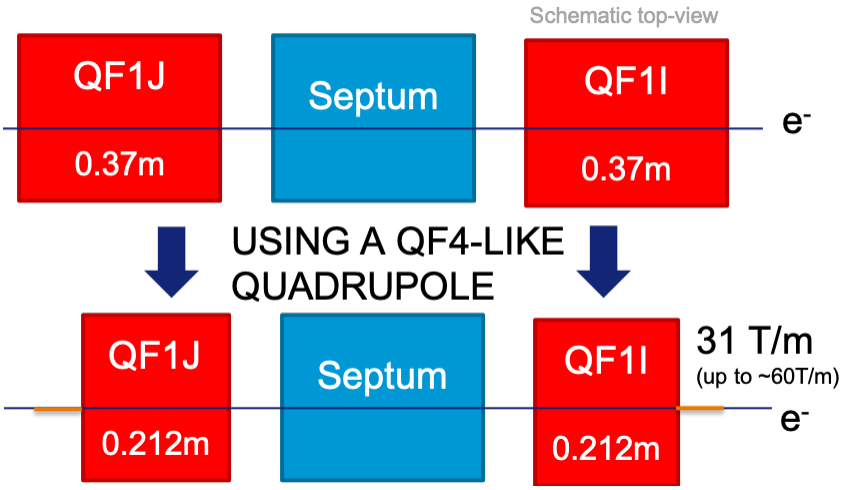

Figure 5-1: Schematic view of quadrupoles in the injection cell straight section. The long quadrupoles used for EBS are replaced by QF4-like ARC cell quadrupoles.

This replacement is done in the lattice using a QF4-like quadrupole. This magnet is chosen because in its design it includes a larger horizontal space between the stored beam and the iron yoke of the magnet (see Figure 5-2 left). This space is necessary at the injection point to fit the vacuum chamber transferring the beam from the injectors to the storage ring. A schematic view is provided in Figure 5-2.

This project has received funding from the European Union's Horizon 2020 research and innovation programme under grant agreement No. 871072.

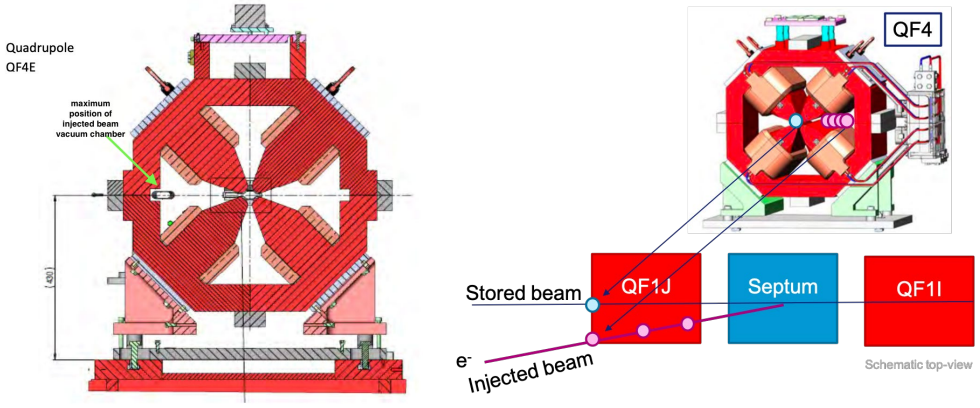

Figure 5-2: Right: schematic view of the injected and stored beam trajectories inside the quadrupole upstream the last injection septum (in the storage ring). The space among the poles of the quadrupole QF4 may be used to fit the injected beam vacuum chamber. Left: QF4E magnet with extra space on the horizontal plane.

The optics are rematched using the first four quadrupoles adjacent to the injection point on each side (4 quadrupoles upstream and 4 downstream) in symmetric pairs with respect to the injection point.

The result of this modification is displayed in Figure 5-3. A final gradient of 31T/m is obtained for the QF1I and QF1J quadrupoles. This value is well within the limits of the QF4 type magnets (< 60 T/m). The horizontal beta at the injection point increases by about 0.7 m following this action.

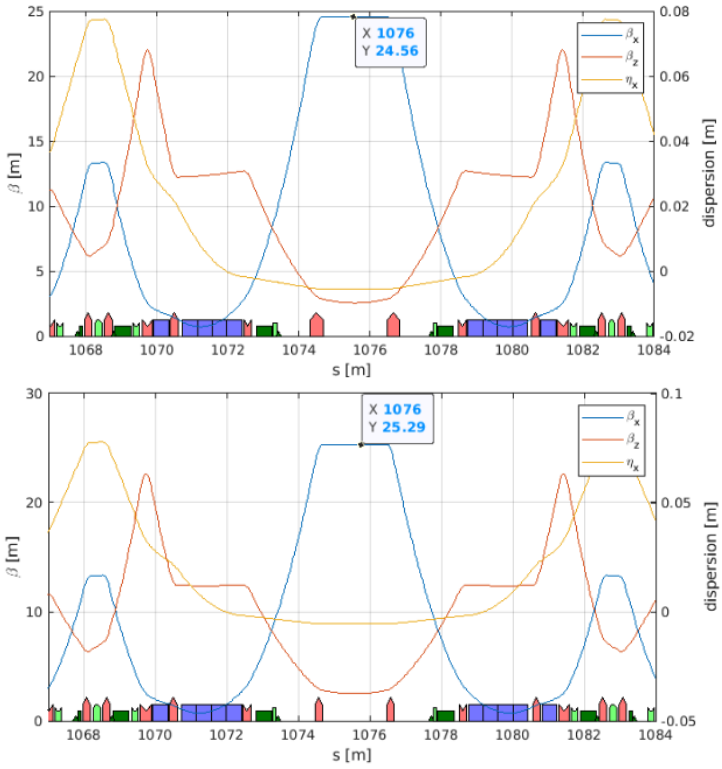

Figure 5-3: Optics in the injection cell. Top: original lattice, EBS like with 0.37m long QF1I and QF1J. Bottom, updated lattice using QF4-like quadrupoles for the injection cell straight section.

This project has received funding from the European Union's Horizon 2020 research and innovation programme under grant agreement No. 871072.

In terms of dynamic aperture and Touschek lifetime there is no visible consequence in absence of errors as shown in Figure 5-4. The differences observed are within the resolution of the DA search algorithm. The specific design of the injection region will have to be addressed in the near future to make sure all elements can fit appropriately and the magnets good field regions and stay clear are sufficient. If needed, a specific magnet design will have to be used for the injection quadrupoles.

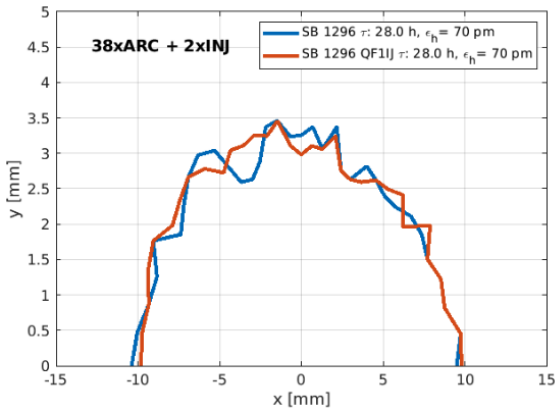

Figure 5-4: Dynamic aperture at injection and Touschek lifetime of the USSR-SB lattice with long EBS like QF1IJ quadrupoles (blue curve) and QF4-like, short QF1IJ quadrupoles (red curve).

Change of length of QF6 and QF8 high gradient quadrupoles

The gradient of QF8 magnets in the baseline USSR lattise with SB showed a QF8 gradient about 92 T/m. On the other hand the QF6 gradient is 90.18 T/m.

The change of length of these two magnets impacts both the magnet design (length and pole profile optimization) and the vacuum chamber design. The vacuum chamber in this region of the cell (about QF6 and QF8) needs to be redesigned in any case as the bending angle of the DQ1 and DQ2 dipole-quadrupoles is changed (40 cells instead of 32 for EBS). The magnet design modification would be a recomputation of the main parameters of the magnet and eventually a reoptimization of the magnet pole shapes. The mechanical drawings of the magnets would need to be revisited.

The length of the QF6 is thus empirically shortened by 1.3 cm and that of the QF8 increased by 1.3 cm. The total length of the cell is unmodified. The optics are matched using all quadrupoles and targeting the standard optics matching knobs.

The modification of the lengths balances the gradient of QF8 and QF6 to about 91 T/m and leaves further margin to increase the field within the power supply limit (110A). It is important to notice, that for EBS these magnets are not used for optics correction, even if they have independent power supplies.

Sextupole magnets with correctors

In Figure 5-5 a margin region is depicted on the sextupoles calibration curves. This is left unused to allow for stronger horizontal, vertical and skew correctors fields (obtained by correction coils on the same yoke as the sextupole). In fact when operating in the saturation region the maximum achievable correction fields are reduced (see [29] for more details). This margin will be also of large interest for the lifetime optimizations during machine commissioning and operation.

This project has received funding from the European Union's Horizon 2020 research and innovation programme under grant agreement No. 871072.

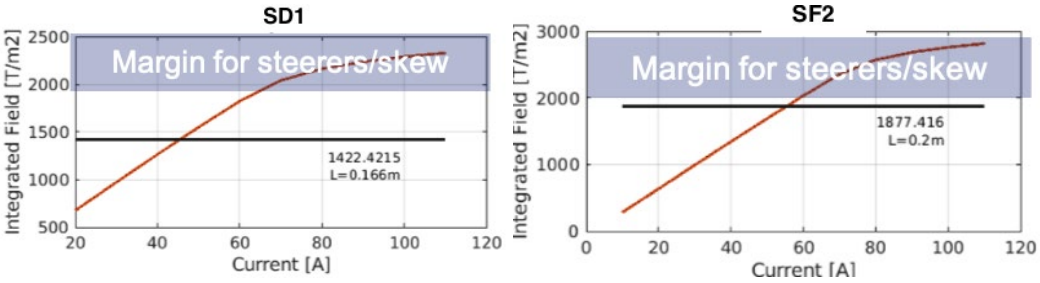

Figure 5-5: Calibration curves of SD1 and SF2 designed for EBS and operating point of USSR 40 long + SB (nominal field, black line).

Swap of QD3 and QD2 magnet lengths

Another important observation is the fact that QD3 operates rather close to the limit of the power supply (see Figure 5-6). This magnet is used for optics correction and some margin must be made available for optics tuning.

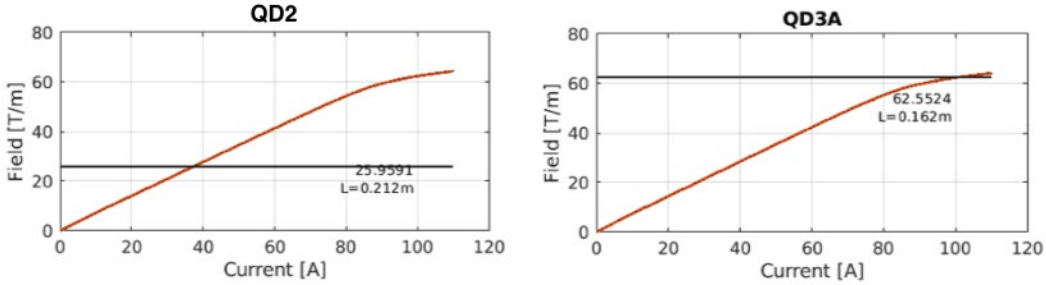

Figure 5-6: Calibration curves of QD2 and QD3 designed for EBS and operating point for the USSR lattice baseline option with RB (nominal field, black line).

In order to reduce the current needed for the QD3 magnet, the magnets QD2 and QD3 have been swapped (Figure 5-7). This action allows better balance of the integrated gradient requested from these two magnets: a shorter magnet is used where a lower integrated gradient is needed. This modification was not done for the injection cell QD2IJ and QD3IJ quadrupoles whose gradients were already well balanced. Figure 5-8 shows the updated status of the gradients compared to their expected calibration curves after lattice optics matching using all quadrupoles. The QF6 and QF8 magnet gradients increased but are still within the limit of the power supplies (scaling the calibration curves with the updated lengths of the magnets).

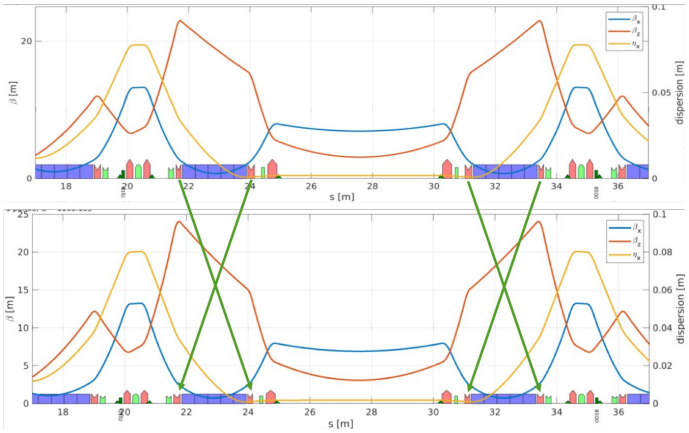

Figure 5-7: Swap of QD2 and QD3 in the standard cell.

This project has received funding from the European Union's Horizon 2020 research and innovation programme under grant agreement No. 871072.

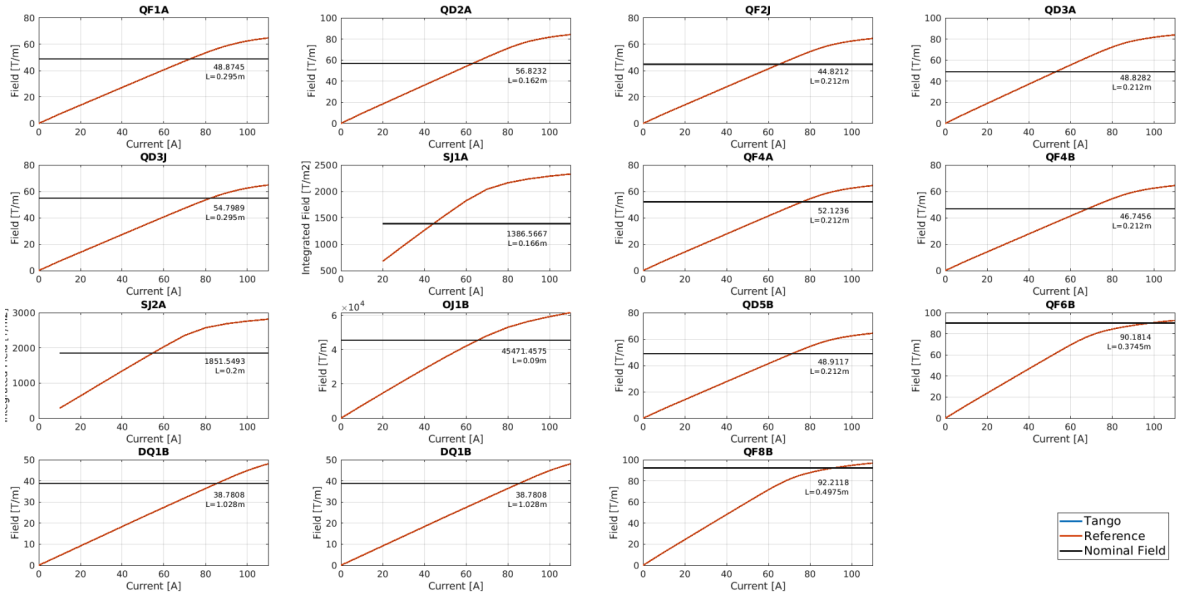

Figure 5-8: Calibration curves of magnets designed for EBS (linearly scaled to the updated lengths) and operating point of USSR V4-SB (nominal field, black line) with QD2-QD3 lengths swapped and modified length QF6 and QF8.

The modifications described above did not result in significant changes of the lattice performances in terms of dynamic aperture and lifetime in absence of errors (Figure 5-9). On the other hand the horizontal emittance increased by more than 1 pm compared to the value which was before modifications and the QF8 quadrupole gradient reached 92 T/m (still feasible with the increased length of the magnet). Due to these two drawbacks the swap of QD2 and QD3 magnets might be revisited in a future lattice release.

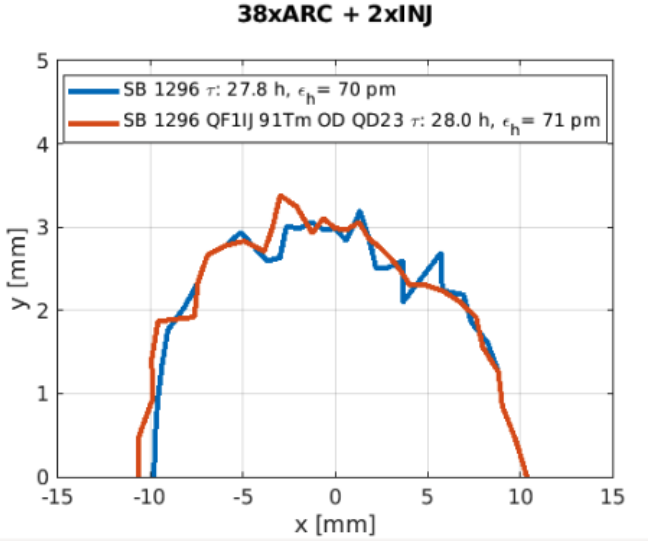

Figure 5-9: Dynamic aperture and Toushek lifetime after a modification of lengths for magnets QD2 QD3 QF6 and QF8.

Table 5-1 reports the magnets gradients for the EBS and for baseline USSR lattice option with RB (standard cell only). The magnets are assumed identical to the EBS ones. Those that would need to be revisited are marked using bold font.

This project has received funding from the European Union's Horizon 2020 research and innovation programme under grant agreement No. 871072.

Sextupoles have been removed from the list of magnets to be redesigned (in bold in Table 5-1) as the present design is sufficient for operation. The same stands for octupoles.

Table 5-1: list of standard cell magnet gradients for EBS, and for version of the USSR lattice with SB. In bold, magnets design to be revisited for USSR. Corresponding vacuum chambers would also need adjustment.

	EBS	**USSR 40 long cells + V4-SB (2021)**
DL1	0.17 - 0.67 T L = 0.3576 m	**0.13 - 0.53 T** **L = 0.4178 m**
DL2	0.17 - 0.54 T L = 0.3576 m	**0.13 - 0.43 T** **L = 0.4178 m**
QF1	53.48 T/m	48.87 T/m
QD2	-57.05 T/m	-56.82 T/m L = 0.162
QD3	-52.93 T/m	-48.83 T/m L = 0.212
QF4	52.09 T/m	52.12 T/m
QD5	-57.84 T/m	-48.91 T/m
QF6	91.03 T/m L = 0.3880	90.18 T/m **L = 0.3745**
DQ1	0.57 T -36.86 T/m	**0.48 T** **-38.78 T/m**
QF8	89.38 T/m L = 0.4840	**92.21 T/m** **L = 0.4975**
DQ2	0.78 T -31.18 T/m L=0.8 m	**0.52 T** **-31.09 T/m** **L= 2 x 0.4m**
SB	0.86 T	0.86 T
SD1AE	-1718 T/m^2	-2044 T/m^2
SF2	1657 T/m^2	1705 T/m^2
SD1BD	-1617 T/m^2	-1343 T/m^2
OD	-36000 T/m^3	-44000 T/m^3

DL magnets

Modules of longitudinal gradient dipole (LGB) magnets will have to be redesigned in compare with those of EBS because of the USSR lattice cell has different total angle. It is planned tob e done till the end oft he Project.

This project has received funding from the European Union's Horizon 2020 research and innovation programme under grant agreement No. 871072.

Short bend design

Only combination of magnets, namely, sequence of DQ2C - short bend –DQ2C, should be designed "from the ground". Thus, we carried out preliminiral design of the Short Bend. Vladimir Skachkov from NRC KI – ITEP made a significant contribution to that design.

Figure 5-10 shows the computation model and 3D outlook of five permanent Bending Magnet (BM) modules of various designs for ESRF EBS (Extremely Brilliant Source). The modules form a step-shaped longitudinal distribution of the magnetic field gradient, contributing to the emittance decrease.

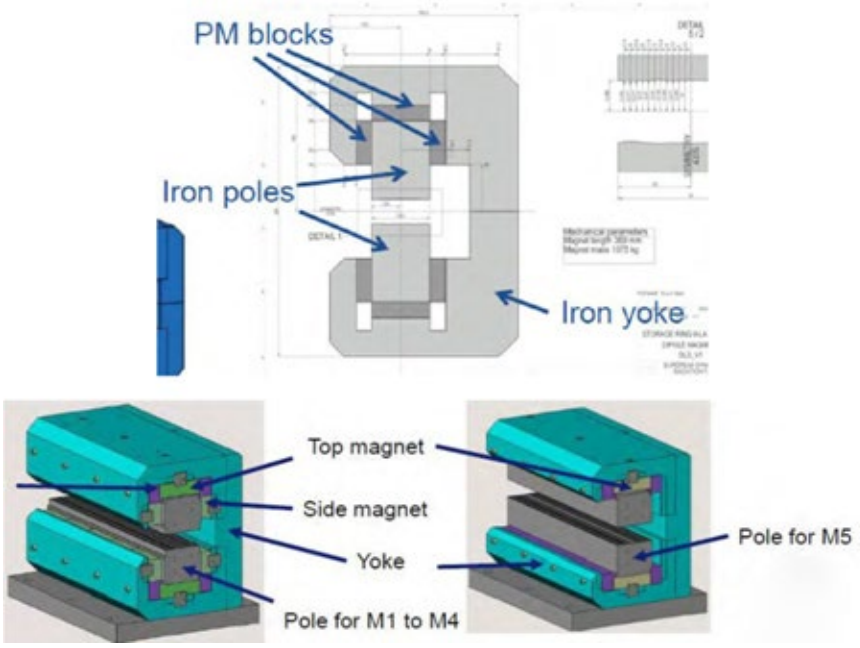

Figure 5-10: Calculation model – top and the EBS PM Bending magnets 3D outlook – bottom.

The explicit-pole design of EBS Bending Magnets provides for the use of technically pure iron for the magnetic poles and PM blocks made of rare-earth alloy Sm_2Co_{17}, with parameters listed in Table 5-2. To achieve high working field uniformity (of ≈ 2 $\times 10^{-4}$ within horizontal width of ± 10 mm), the ratio of the transverse working area dimensions has been chosen (vertical /horizontal) of ≈ 30 mm / 60 mm, whereas a special shape is given to the pole profile.

Table 5-2: Main BM parameters (for new SR Sources).

Parameter	SBM	2PW	3PW	3PW18
Maximal field, T	0.86	0.86	0.86	1.56
Length, mm	63	102	102	109
Permanent Magnet	Sm_2Co_{17}	Sm_2Co_{17}	Sm_2Co_{17}	Sm_2Co_{17}
Pole material	Pure Fe	Pure Fe	Pure Fe	Pure Fe

Computation of PM Short Bending Magnet with Explicit Magnetic Poles

In this project, a synchrotron Bending Magnet of an explicit-pole design excited by uniformly magnetized Sm_2Co_{17} blocks is considered. Figure 5-11 shows the BM design model with the main parameters listed in Table 5-3. In addition to traditional blocks whose magnetization is perpendicular to the faces of the parallelepiped, a pair of corner blocks with magnetization directed along the

This project has received funding from the European Union's Horizon 2020 research and innovation programme under grant agreement No. 871072.

diagonal of the parallelepiped cross-section is introduced on each pole, shown in Figures 5-11*a*, *b* (compare with the design of EBS magnets, shown in Figure 5-10, top).

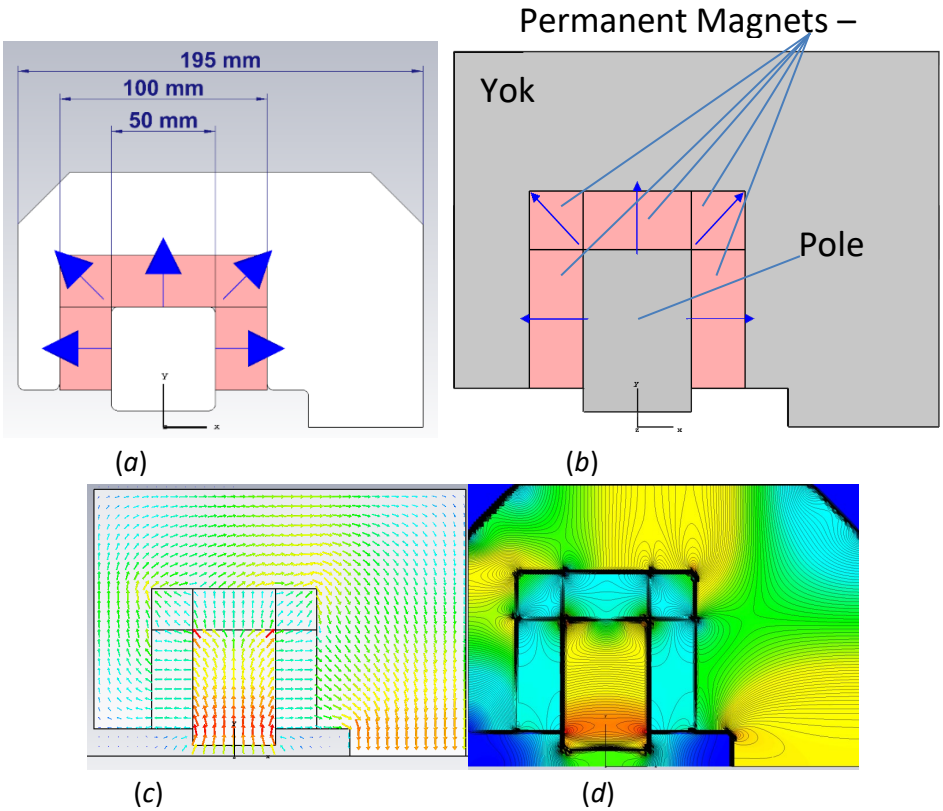

Figure 5-11: Sm_2Co_{17} BM Model (upper half of the cross section z = 0) – *a*; arrangement of permanent magnets – *b*; magnetic flux map – *c* and field level line map – *d*.

This design of the magnetic system is more effective: additionally introduced magnets significantly increase the total magnetic flux generated by permanent magnets, and the leakage flux in the corner (empty) regions between the pole and the magnetic core completely disappears, as can be seen in Figure 5-11*c*. Permanent magnets with such magnetization orientation are commercially available.

Table 5-3: The main parameters of the explicit-pole BM model.

Parameter	
Working field, T	0.89
Magnetic gap, mm	16
Permanent Magnet	Sm_2Co_{17}
Remnant magnetization, T	1.1
Transverse dimensions:	
Poles, mm	50 × 50
Side PM magnet, mm	25 × 40
Upper PM magnet, mm	50 × 25
Magnet length, mm	40
The field in the pole, T	1.8
Pole profile	Not corrected
GFR @ $\triangle B/B_{\text{average}}$=±0.0002, mm	±7

This project has received funding from the European Union's Horizon 2020 research and innovation programme under grant agreement No. 871072.

The design does not assume for the closure of the left branches of the magnetic yoke to optimize the magnet design. The decision is made for reasons of accessibility of the working magnet area for insertion from the outside of the magnet and a vacuum chamber arrangement here.

The field uniformity of the synchrotron BM is one of its most important parameters, usually set at 0.1% or better. In our case, the ratio of the pole width to the magnetic gap of 50/16 = 3.1 is chosen, due to which the field nonuniformity in the transverse plane (Figure 5-12a) is reduced to $\triangle B/B_{average}$=±0.0002 in the region (GFR - Good Field Region) of ±7 mm in the transverse (horizontal) coordinate (see Table 5-3, Figure 5-12*b*). At the same time, we did not optimize the pole profile.

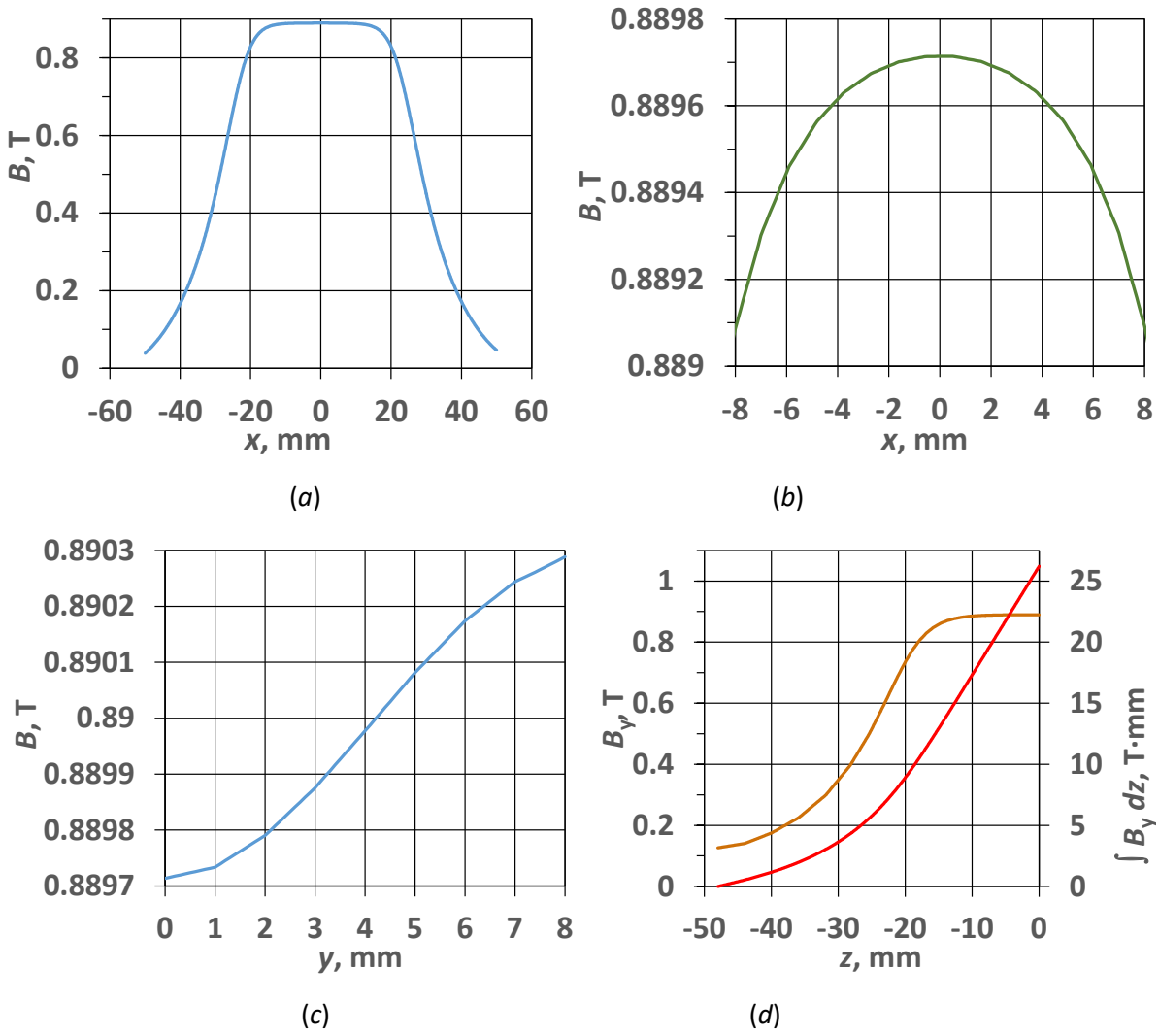

Figure 5-12: The field distributions in EBS BM magnet: transverse (horizontal) in the central section - *a*, its top part on a detailed scale - *b*, transverse (vertical) - *c*, as well as the longitudinal for the operating field component and its integral - *d*.

Along another transverse (vertical) coordinate, the relative field magnitude changes (increases) at a speed of ~10^{-4}/mm (see Figure 5-12*c*) and reaches $4\cdot10^{-4}$ on the inner surface of the vacuum chamber (y = 5.5 mm).

In the longitudinal direction (Figure 5-12*d*), the working field component B_y shows a relatively slow decline at the magnet edge: within the 30 mm area in front of the dipole geometric edge the

This project has received funding from the European Union's Horizon 2020 research and innovation programme under grant agreement No. 871072.

field decreases down only to the ~10% level. This field behavior requires optimization of the magnet design in order to reduce magnet impact on the surrounding equipment and to eliminate uncontrolled and unpredictable field integral variations associated with partial shunting (or superimposition of external) magnetic fluxes of this magnet by other magnetic elements of the accelerator. As shown in Figure 5-12*d*, the integration of the undisturbed field of the specified 40 mm long Bending Magnet (see Table 5-3) within the $z \in [-50, 50]$ mm interval is 52 T·mm. Such a field integral provides a deflection of the 6 GeV electron beam at an angle of 2.6 mrad.

At the stage of technical design, the issue of optimizing the magnetic system size and, in particular, the necessity to give the magnet pole a special profile is being considered. This list should be supplemented with the possibility to improve actively the magnetic flux distribution near the edges of the pole (Figure 5-12*c*) with additional permanent magnets. Such improvement significantly increases the field near the pole edges, where the field level lines show high density (Figure 5-12*d* and Figure 5-12*a*), and thereby moves the line corresponding to the accepted inhomogeneity tolerance out of the magnet gap. This approach seems to be technically simpler compared to the precise mechanical pole processing up to the calculated profile.

PM Split-pole Dipole as Short Bend

The PM dipole field of the split-pole design with magnetization $\mu_0 I$ depends logarithmically on the magnet radii R_1, R_2 ratio (Figure 5-13*a*):

$$B = \mu_0 I \ln \frac{R_2}{R_1}.$$

This means that only the coercivity finiteness of the selected permanent magnet limits the working field. So, for example, if the radii ratio is $R_2/R_1 = e$, then the dipole induction will be 1.1-1.3 T, depending on the choice of the modern rare-earth permanent magnet type, in which the coercivity extends from $\mu_0 H_C$= 1.5 to 3.5 T. Such field is significantly lower than the maximal level achievable in practice. In particular, in a split-pole quadrupole lens with a ratio $R_2/R_1 \approx 4$, shown in Figure 5-13*b*, the field at the pole tip achieved of more than 1.8 T [30].

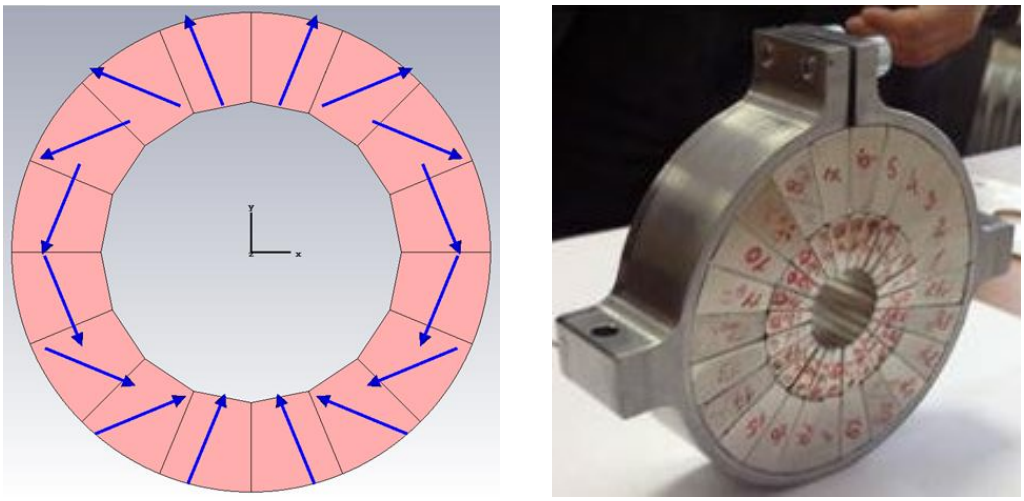

(*a*) (*b*)

Figure 5-13: Rule of magnetization distribution in a split-pole dipole magnet (spears – permanent magnet magnetization ***I***) – *a* and *b* – a quadrupole module for the PRIOR proton microscope lenses.

This project has received funding from the European Union's Horizon 2020 research and innovation programme under grant agreement No. 871072.

It is especially effective to use permanent magnets in the split-pole magnet design with small apertures [31, 32]. So if we fix the field at 0.9 T, then the external dipole dimension changes linearly, reaching only D_2= 70 mm at aperture of ∅ 30 mm (Figure 14*a*). In this case, the mass of the 50 mm long dipole will be about 1.2 kg. If the aperture is fixed at a low level of ∅16 mm, then a field of 1.15 T will be achieved at an external size of D_2= 45 mm, whereas the magnet mass will be of about 0.6 kilograms (Figure 5-14*b*).

In order to obtain a field of 0.9 T at the required aperture of ∅16 mm, the external dimension of the dipole should be set to ∅36 mm, and the mass of such 50 mm long magnet will be of about 0.35 kg.

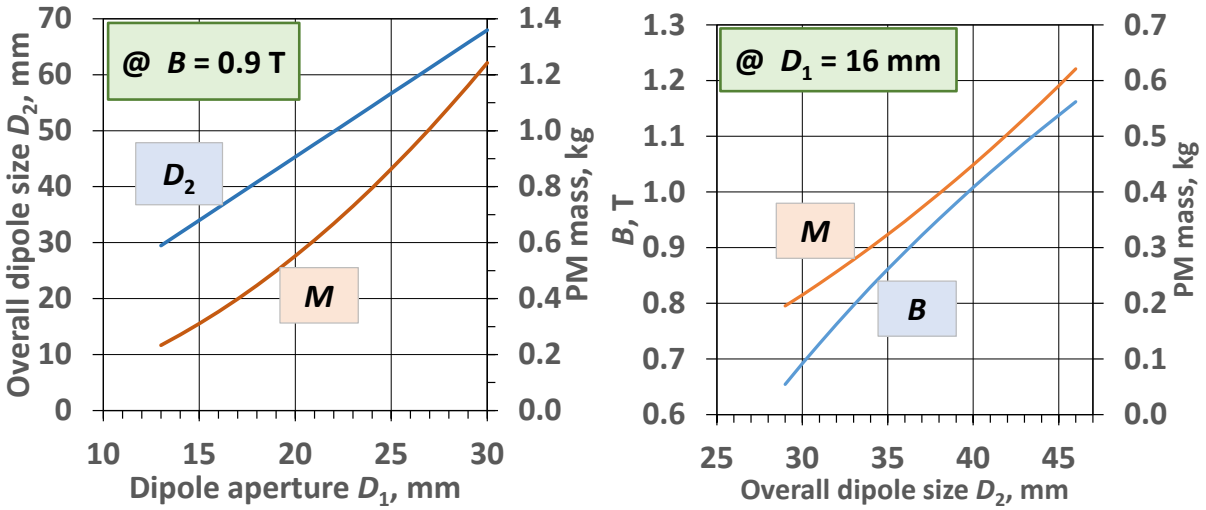

(*a*) (*b*)

Figure 5-14. Main characteristics of a 50 mm long Sm_2Co_{17}split-pole dipole: *a* – @ *B*=0.9 T and *b* – @ D_1=16 mm.

No less effective is the use of other types of split-pole dipole design to create a Bending Magnet for the SR installation, both containing a magnetically soft yoke and consisting entirely of only PM elements [33–37].

The disadvantages of the split-pole design of a multipole magnet include:

– Relatively high inhomogeneity of the magnetization distribution of modern permanent magnets, which disturbs around the aperture surface the field magnitude and its configuration up to noticeable at an accuracy level of about 0.1%. It is possible to use the local remagnetization techniques of a PM material developed in NRC KI - ITEP to suppress these disturbances.

– Relatively low resistance to temperature variations and radiation damages. Because of the influence of these factors, irreversible decreases in the magnetization of the PM material may occur, and utilizing of thermal compensators will be required to reduce small temperature fluctuations.

These factors influence decreases with the PM moving away from the axis of the accelerator, as well as with the PM protection from direct irradiation on its surface.

Summarizing the results obtained , we note:

- Possible ways of solving the problem of creating a PM Bending Magnet for the main ring of an electron synchrotron are considered and analyzed.

This project has received funding from the European Union's Horizon 2020 research and innovation programme under grant agreement No. 871072.

- A dipole magnet of an explicit-pole design is proposed and calculated, in which permanent magnets with a diagonal orientation of magnetization are introduced into the corner cavities between the poles and the yoke in order to optimize the field and dipole sizes, as well as to increase the efficiency of using permanent magnets. It is shown that with specified aperture of ∅16 mm, it is possible to achieve a magnetic field of at least 0.9 T with a field uniformity of $\triangle B/B_{average}$=±0.0002 in a region of at least ±7 mm.
- A dipole magnet of a split-pole design with an invariable field of 0.9 T at a specified aperture of ∅16 mm is calculated. The advantages and disadvantages of this Bending Magnet design are shown.
- It is noted that the split-pole design calculated in this project can be recommended for use as the most advanced and tested in real conditions of operation on relativistic electron beams at the USSR4 (SYLA) installation for the ring structure being developed within the framework of the CREMLINplus project. At the same time, the noted advantages of the split-pole design should be considered as a basis for conducting of experiments of this design magnets direct testing under operating conditions on beams as SR source.

6 Injection scheme

Injection systems are a critical part of the storage. Their design and properties may substantially impact the overall performance and operation of the machine. Two main performance criteria are generally considered in the choice of the injection scheme: the injection efficiency and the perturbation to beam lines users during top-up injection [38]. In case of low injection efficiency a higher number of electrons will be produced that may lead to unacceptable radiation levels while strong injection perturbations may prevent beam lines to run experiments across top-up injection. In addition, other considerations will impact the choice of the injection scheme such as the size of the acceptance, the injected beam characteristics or the robustness of the system. In this section we will review the different options available and apply them to the USSR lattice. In view of the remaining uncertainty on the choice of the injectors we will not draw any conclusion or final recommendations in this report but rather address the feasibility of each system.

Standard off-axis injection

This scheme was adopted in most third generation light sources and is still used in many laboratories, including the ESRF [39]. It consists of an in-vacuum septum and four fast kickers. The in-vacuum septum is used to steer the injected beam parallel to the stored beam and the four kickers are used to generate a closed orbit bump that will reduce the separation between the stored and injected beams. This bump needs to be ramped up to its maximum amplitude and then back to zero within a turn. The minimum distance between the stored and injected beam is determined by the septum blade, used to shield the stored beam from the deflecting field, thickness and the minimum distance at which the two beams can approach the blade, constrained mostly by their sizes. The injection perturbations depend on how well the fast injection bump is closed over the whole pulse.

This project has received funding from the European Union's Horizon 2020 research and innovation programme under grant agreement No. 871072.

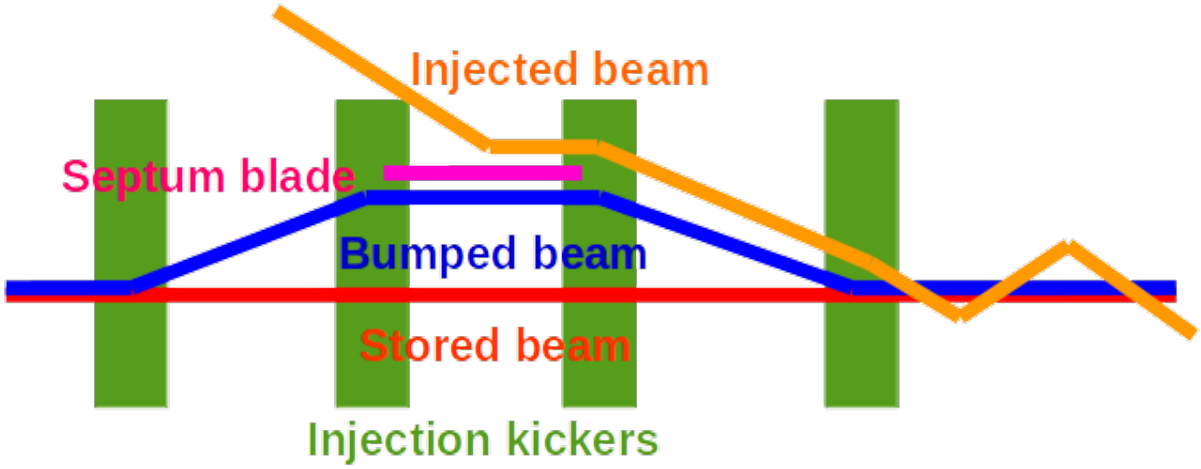

Figure 6-1: Schematic view of standard off-axis injection.

Figure 6-1 shows a schematic view of the standard off-axis injection, the stored beam, in red, is bumped, in blue, towards the septum blade, in magenta, but is not deflected by the septum field as opposed to the injected beam, in orange, which trajectory is steered parallel to the bumped beam trajectory by the septum. The bump being closed, the stored beam remains in theory on the closed orbit while the injected beam oscillates around it until it is damped by synchrotron radiations.

The injection efficiency is then determined by the amplitude of these injection oscillations, the injected beam size and the storage ring transverse acceptance. This is illustrated in Figure 6-1a where a planar view of the horizontal phase space is shown. The stored, bumped and injected beams are shown as well as the septum blade and the horizontal acceptance. Particles falling outside the horizontal acceptance, dashed line ellipse, are lost. Off-axis injection therefore requires sufficiently large horizontal acceptance in order to accommodate the injected and bumped beams as well as the septum blade. Constraints on the acceptance are therefore strongly dependent on the injected beam properties and the septum blade thickness.

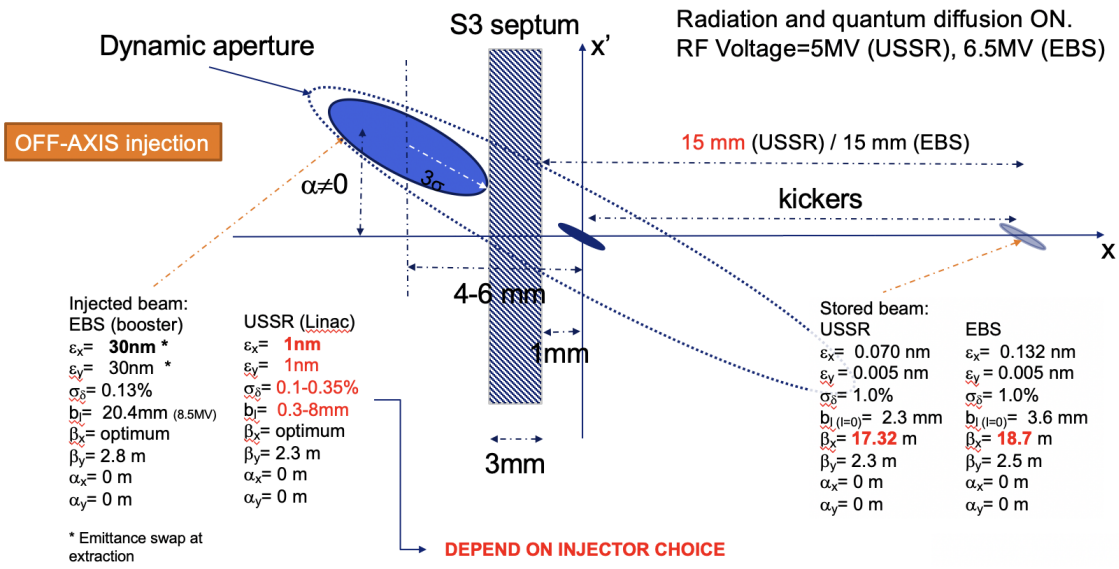

Figure 6-1a: Horizontal phase space view of the injection point.

This project has received funding from the European Union's Horizon 2020 research and innovation programme under grant agreement No. 871072.

The horizontal acceptance is generally increase by introducing a large horizontal β-function at the injection point. This can be achieved by rematching two special cells dedicated to the injection and by adding two focusing quadrupoles in the straight section.

This is shown in Figure 6-2 where the 2 injection cells layout and optics functions are shown for the USSR lattice. The horizontal β-function at the injection point is increased to 22 m in order to provide better injection efficiency. Using this layout it is possible to match the deflection angle of the four injection kickers to generate a 15 mm closed orbit bump. This amplitude is arbitrarily chosen based on the ESRF-EBS design [40], however the only constraint concerning the placement of the septum blade and hence the injection bump amplitude is that it should not be the smallest aperture. Still based on the ESRF-EBS design, with collimators placed at +/-6 mm at a smaller horizontal β-function, the septum blade could be approach as close as 10 mm from the beam axis, further relaxing the kicker design. This value is most likely optimistic and needs to be confirmed after the design of the collimation system, it will however be assumed for further calculation regarding advanced injection schemes in the following sections.

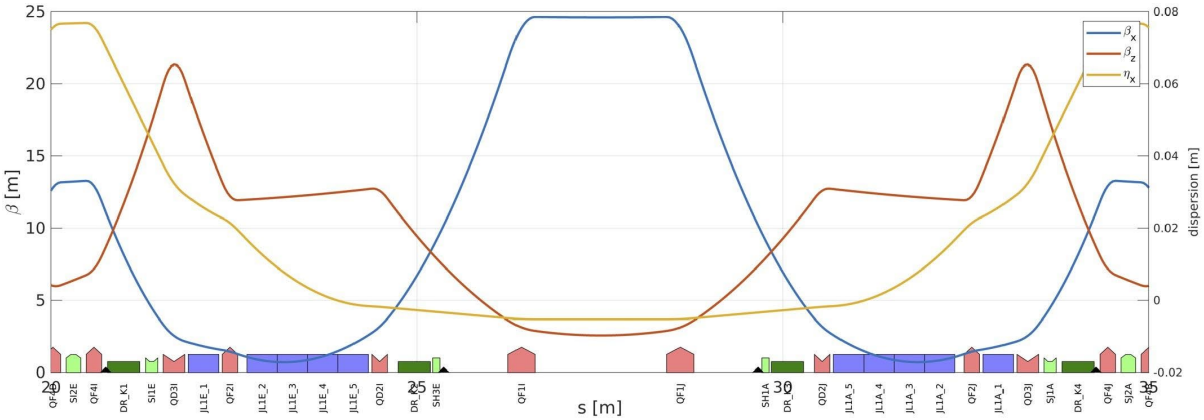

Figure 6-2: Injection cells of the USSR lattice, the injection kickers are marked in dark green.

Figure 6-3 shows the result of this matching, the four kickers strength are well balanced with a maximum at 2.0 mrad. This is fully compatible with the ESRF-EBS injection kickers design [17] that have a nominal kick angle of 2.36 mrad and can therefore be used for the USSR lattice. The kicker pulse width has to be equal or less than a turn in order to prevent the injected beam to be lost on the septum blade in the turns following injection. The duration of its flat-top, allowing to inject multiple bunches with the same oscillation amplitude, depends on the length of the bunch train from the injectors. The technical specifications of the pulsers will therefore depend on the choice of the injectors.

Similarly the in-vacuum septum design depends strongly on the injected beam characteristics and the transfer line layout. Nevertheless, a critical parameter is the septum blade thickness that can have a strong impact on injection efficiency as it determines the separation between the injected and stored beams.

This project has received funding from the European Union's Horizon 2020 research and innovation programme under grant agreement No. 871072.

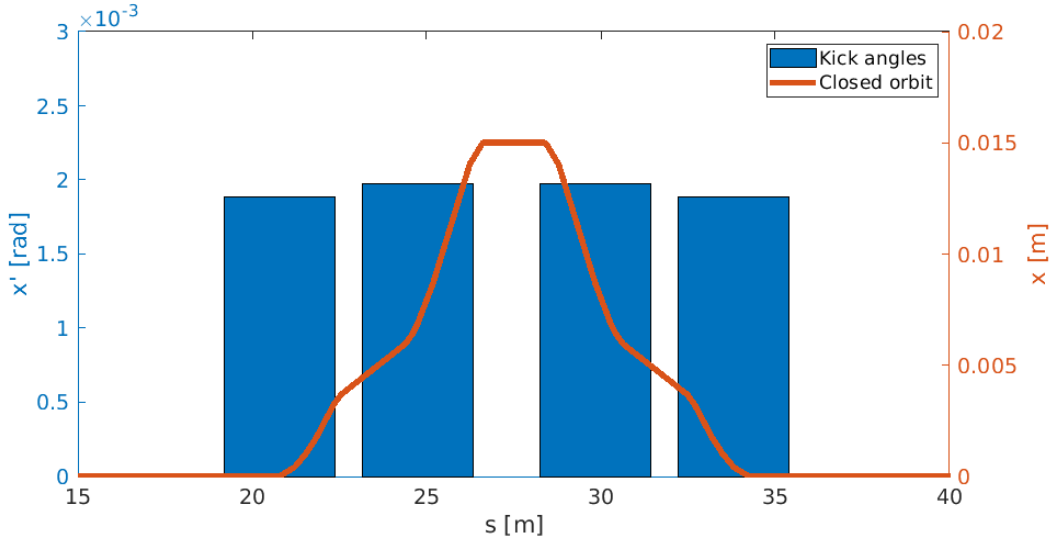

Figure 6-3: Injection bump and injection kickers deflection angles.

This is seen in Figure 6-4 where the injection efficiency as a function of the septum blade thickness for different injectors options are shown. The difference between the various scenarii is driven by the variations of the injected beam size. We can see that 100% efficiency can be obtained for all cases considered in case the septum blade thickness is 1 mm. On the other hand, the ESRF design with 3 mm septum blade thickness will not allow for 100% efficiency with the short booster option. The choice of the blade thickness will then drive the frequency of the pulser: the thinner the blade the higher the frequency to provide sufficient shielding from eddy currents established in the blade and prevent strong perturbations on the stored beam. Active feedforward systems can also be used to mitigate these perturbations [41]. However moving to high frequencies will result in stronger field variations along the bunch train and may reduce injection efficiency. The in-vacuum septum specifications are critical for the future performance of the accelerator facility and a good balance between injection efficiency and injection perturbations has to be found.

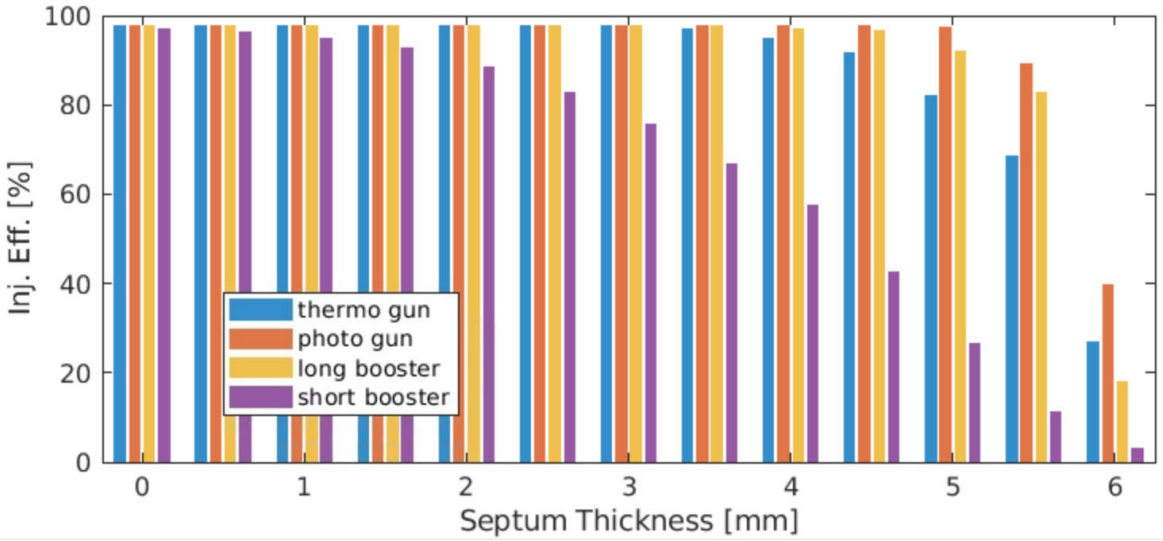

Figure 6-4: Injection efficiency as a function of the septum blade thickness for different injectors options.

This project has received funding from the European Union's Horizon 2020 research and innovation programme under grant agreement No. 871072.

Many critical decisions on the choice and specification of the storage ring injection systems derive from the choice of injectors and the injected beam characteristics. These can therefore not be made at this stage of the design. We strongly recommend freezing the injectors layout as soon as possible in order to progress on the other aspects of the injection systems design that will be critical for the future performance of the accelerator complex.

Advanced injection schemes

The standard off-axis injection allows to inject at high efficiency providing the acceptance of the storage ring is sufficiently large to accommodate the injected beam. Due to the unavoidable differences between the four injection kickers it is however not possible to perfectly close the injection bump and provide fully transparent injection using this method. Feed-forward and feedback systems have been used in some places to mitigate these perturbations but they are complicated to operate [42]. For a green field machine like the USSR is therefore desirable to explore other techniques as the design stage in order to reach the desired 100% efficiency transparent injection.

Recent fourth generation light designs feature much smaller transverse beam size, dynamic aperture and lifetime. As a result more frequent injections with significantly reduced perturbations are needed to provide stable operating conditions to the beam line users. Significant effort was therefore made in the light source community to provide high efficiency transparent injection using more complex injection schemes. This section will give an overview of some of these techniques and how they can be applied to the USSR ring.

The injection schemes considered in this report are the following:

- Single non-linear kicker [43 ,44]
- Swap-out injection [45-47]
- Longitudinal on-axis injection [48-50]
- Shared oscillation using a fast kicker [51]

This list is non-exhaustive and other potential candidates may be considered in future studies [52-54]. For now, we limit ourselves to these four methods having in common the use of a single or a series of non-conventional kickers that feature either complex higher order multipole fields or very fast pulses and require to dedicate two straight sections to integrate the injection point and the non-conventional kicker(s). The choice of the technique however strongly depends on the injectors and it is not possible to make the final recommendations at this point of the design where the injectors and injected beam characteristics are still under discussion. We will however show later in this report that it is possible to provide a common layout for all these methods in order to provide sufficient flexibility and allow progress on the design of the injection scheme until a decision is made concerning the injectors.

Figure 6-5 shows a schematic view of the four injection schemes considered in this report. All feature an in-vacuum septum at the injection point which blade is assumed to be at 10 mm for a horizontal β-function of 22 m. Except for the non-linear kicker injection, where an offset at the kicker is needed, the optimal phase advance between the septum and the kicker is $\pi/2$ such that the injected beam offset is transformed into angle that can be cancelled at the kicker. The shared oscillation scheme can be achieved with or without the closed injection bump as long as the injected beam is inside the transverse acceptance. It is however preferable to include the four kicker bump in order to reduce the required deflection angle in the fast kicker and minimize the injection oscillation to increase the efficiency. Providing the significant reduction of transverse oscillations, slow kickers

This project has received funding from the European Union's Horizon 2020 research and innovation programme under grant agreement No. 871072.

can be used to reduce the injection perturbations and ease the capabilities to correct imperfections with feed-forward or feedback systems [56]. The non-conventional kicker is the major difference between the four schemes. The non-linear kicker ressembles a pulsed octupole allowing to kick the injected beam into the transverse acceptance while the stored beam is not affected because the field goes through zero on-axis. The swap-out and shared oscillation schemes require a fast kicker which pulse width should be smaller than twice the bunch spacing in order to affect only a single bunch. In the first case the injected beam is stored while the stored beam is kicked out of the acceptance, in the second case the injection oscillations are shared between the two beams. Finally the longitudinal on-axis injection requires that the stored and injected beam are separated in time inside the longitudinal acceptance. The fast kicker therefore needs to ramp down from its nominal value down to zero in this time separation which typically is a fraction of a nanosecond.

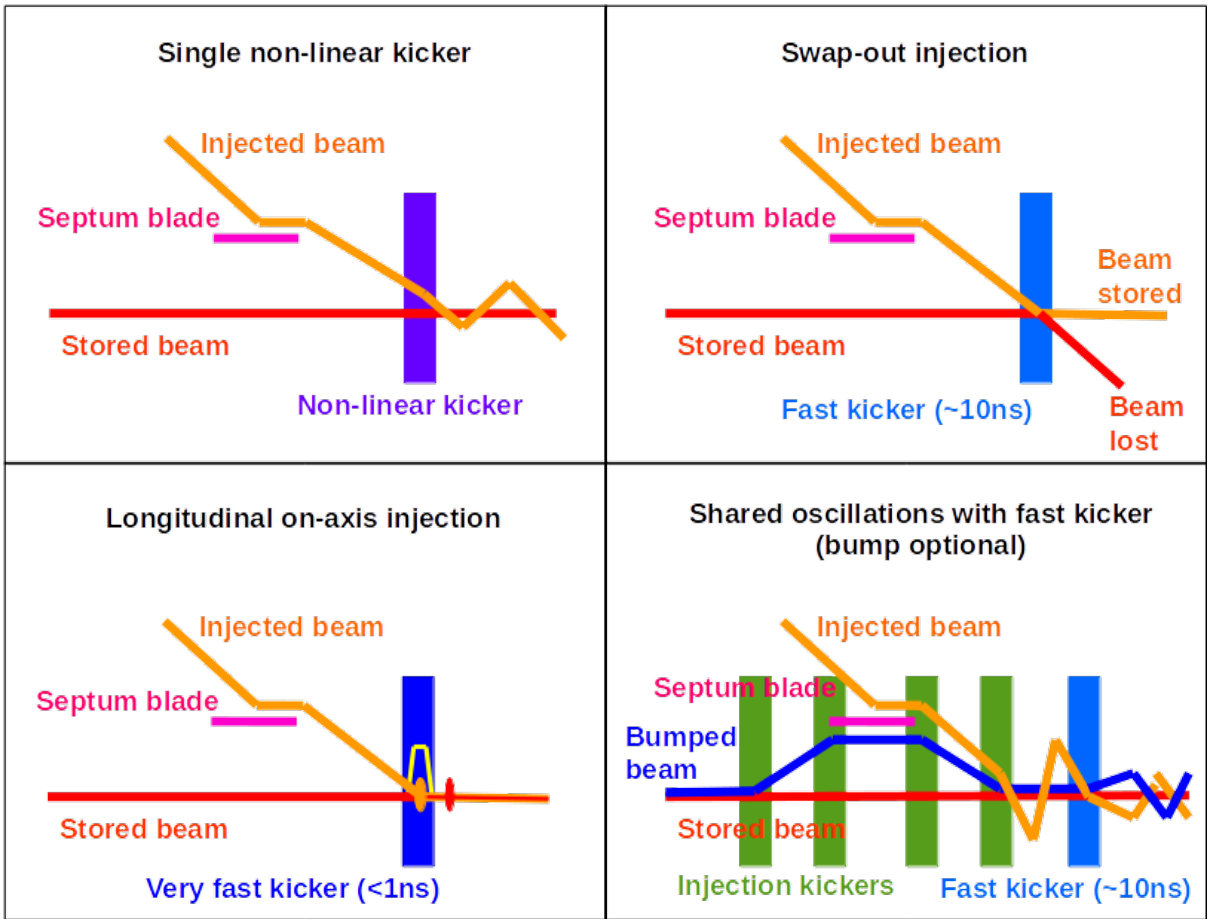

Figure 6-5: Schematic view of the different injection schemes.

Table 6-1 summarizes the main properties of the injection schemes considered in this table. The standard injection and non-linear kicker options will either not provide 100% injection efficiency or transparent injection and are therefore not meeting the design goals. The longitudinal injection is potentially a good candidate but requires a major technological challenge and should not be considered for the baseline design but rather a potential upgrade. The two remaining options are the swap-out injection, adopted at APS, and the shared oscillations envisaged for SLS and ESRF. While the swap-out injection will provide 100% efficiency and fully transparent injection, full current injectors may not be trivial to achieve depending on whether a Linac or a Booster is used. On the other hand

This project has received funding from the European Union's Horizon 2020 research and innovation programme under grant agreement No. 871072.

shared oscillation allows for accumulation and does not feature such restriction. However, achieving transparent injection with this scheme may represent a challenge. In both cases, although it should be adapted, the kicker technology exists [57-59]. Thanks to its reduced deflection angle the shared oscillation option appears to be easier to design. Again, the final decision should be made once the injectors design and injected beam characteristics are frozen.

Table 6-1: Injection schemes main properties.

	Injection efficiency	Injection perturbation	Kicker properties	Comments
Standard off-axis	>90%, injected beam size, SR transverse acceptance	Potentially large, feedforward compensation possible	Kick angle few mrad , pulse width equivalent to 1 SR turn	Well established technique, easy to commission, small injected beam size preferable
Non-linear kicker	>90%, injected beam size, SR transverse acceptance	Transparent	Multipole field, kick angle of the order of 1 mrad	Operated at MAXIV, injection with non-linear field requires small injected beam
Swap-out injection	100%	Transparent	Kick angle few mrad , pulse width ~10ns	Never operated, requires full current injectors and extraction channel. Accumulation not possible
Longitudinal injection	100%	Transparent	Kick angle few mrad , pulse width < 1 ns	Very challenging kicker design, technology not existing
Shared oscillations	100%	Transparent without injection bump or potentially with slow kickers injection bump	Kick angle fraction of a mrad, pulse width ~10 ns	Combines several techniques, staggered commissioning possible, can be upgraded to longitudinal injection

Proposal for the USSR lattice

Providing the uncertainties on the injectors and injected beam properties a flexible layout that allows to implement any of the above options is proposed. The main features of this layout are:

- A high-β straight section with an in-vacuum septum to reduce the non-conventional kicker required angle
- A non-conventional kicker located at $\pi/2$ from the injection point. For the case of the non-linear kicker the septum angle and octupoles can be used as phasers
- Standard off-axis injection systems in the high-β straight section to allow for staggered implementation of the non-conventional system and provide a robust simple solution for the commissioning of the storage ring

This project has received funding from the European Union's Horizon 2020 research and innovation programme under grant agreement No. 871072.

- An RF straight section is inserted between the two injection straight section to avoid strong oscillations in a beam line experiment

Figure 6-6 shows the proposed layout for injection systems. The whole section consists of: standard injection cell with the horizontal β-function bump, an RF section (or empty) straight section and a standard low-β straight section hosting the non-conventional kickers (fast or nonlinear). The phase advance between the injection point and the non-conventional kickers is π/2. No adjustments of phase advance are necessary as the phase advance per cell is approximately 3π/4. The special kicker is placed at the entrance of the straight section such that if it is sufficiently short the second half of the straight section can be used for other purposes, RF cavities or an insertion device for instance.

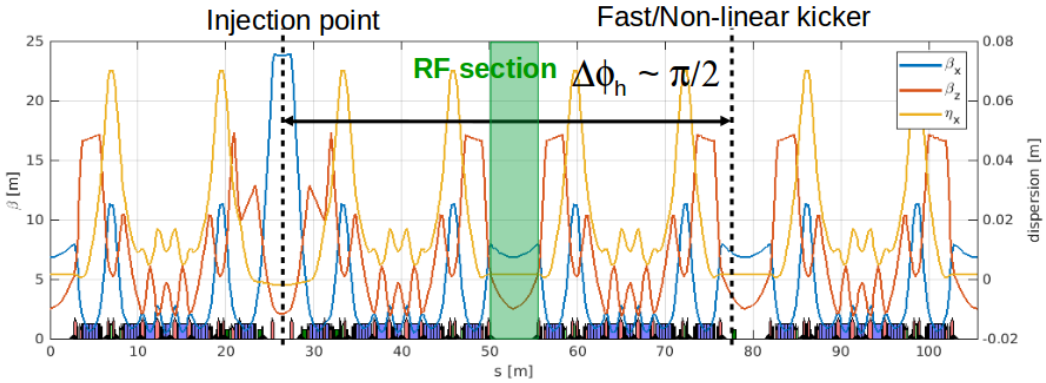

Figure 6-6: Proposed layout for the USSR lattice.

Figure 6-7 shows the horizontal injection oscillation using the layout proposed in Figure 6-6 for the four injection schemes studied in this report. In all cases the septum blade is assumed to be located at 10 mm from the stored beam axis. The cases involving a closed injection bump assume a separation of 6 mm between the stored and injected beams. These values may evolve depending on collimator settings and injected beam characteristics. Using these values it is possible to derive the required kick angle for each of these cases.

Non-linear kicker injection features a single kicker in the second injection straight, large injection oscillations are observed between the injection point and the kicker as shown by the blue curve. These oscillations are reduced down to the level of the ones observed with standard off-axis injection by the non-linear kicker. The stored beam is theoretically not affected. The transverse separation between the stored and injected beam is approximately 3 mm, the non-linear field generated by the kicker therefore has to go from zero to its nominal value of 0.8 mrad in a very short distance. This may represent a significant challenge in the design of the kicker and will require to inject the beam in a strong field gradient which may impact the injection efficiency of such a layout [56, 60, 61].

Swap-out injection features similarly large injection oscillations between the injection point and the kicker, the injected beam oscillation are however completely cancelled with a deflection angle of approximately 1 mrad. The stored beam, in red, is on the other hand kicked out of the acceptance and could be intercepted on a collimator or extraction channel [47] or even recycled in the booster ring [62, 63].

This project has received funding from the European Union's Horizon 2020 research and innovation programme under grant agreement No. 871072.

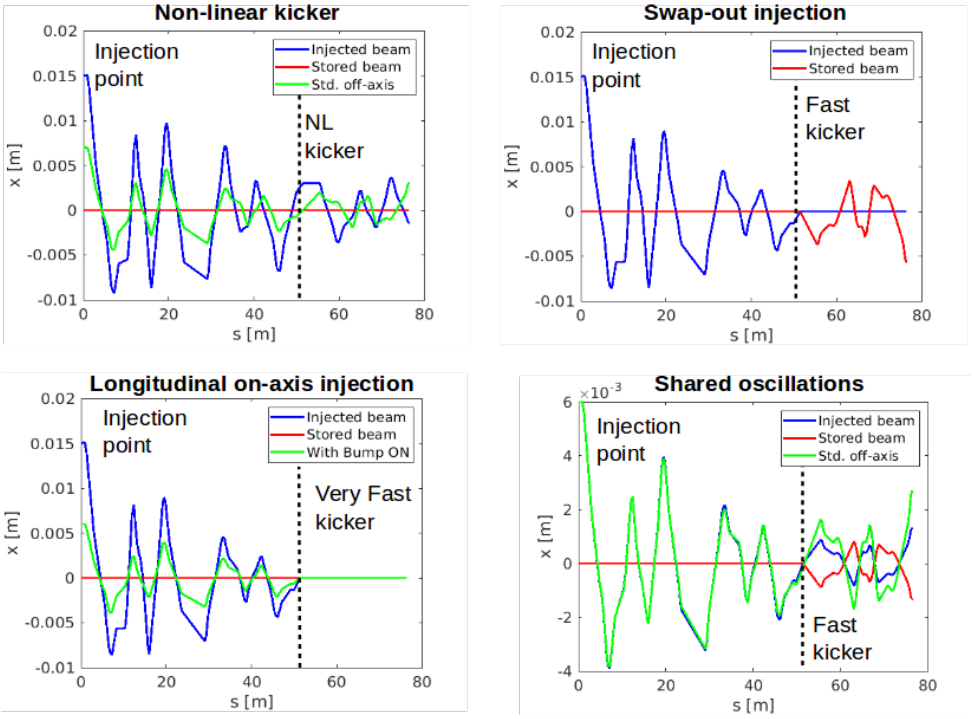

Figure 6-7: Horizontal injection oscillation for different injection schemes with the layout shown in Figure 6-6.

Longitudinal on-axis injection has similar properties as the swap-out injection in terms of injection oscillation and deflection angle, however in this case both beams are stored without any perturbation in the transverse plane. Providing the major challenge to design sub-nanosecond pulser it could be interesting to reduce the required kick angle using a closed orbit bump at the injection point. In this case the kick angle is reduced from 1 mrad down to 0.5 mrad. Figure 6-8 shows the injection efficiency as a function of longitudinal acceptance, a fall time of approximately 0.3 ns would provide 100% efficiency but only for the small beam sizes options, a short booster is therefore excluded in this case.

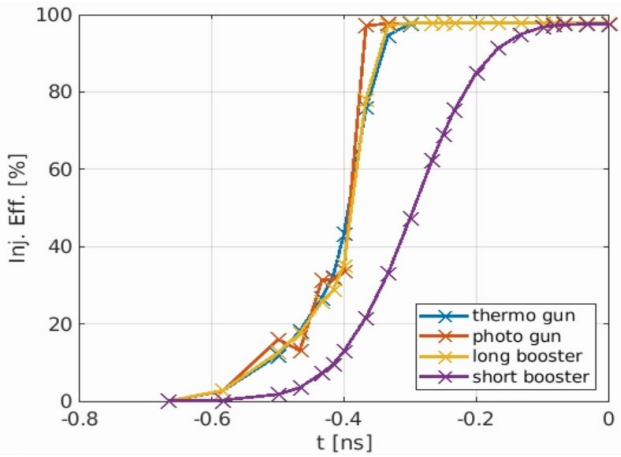

Figure 6-8: Injection efficiency as a function of longitudinal offset.

Finally, the shared oscillation case combines a fast kicker with a closed injection bump. After the kicker, the injection oscillation is shared between the injected and stored beams and therefore

This project has received funding from the European Union's Horizon 2020 research and innovation programme under grant agreement No. 871072.

reduced by a factor 2. This set-up is certainly the less challenging one in terms of pulse width and kicker design as the required kick angle is only 0.25 mrad. It offers the advantage of potential staggered implementation and potential upgrade to swap-out injection by increasing the kicker strength or longitudinal injection with a faster pulser.

Table 6-2 summarized the results of the simulations of these injection schemes. As discussed earlier only the swap-out injection and the shared oscillation schemes are potentially providing transparent injection with 100% efficiency. The shared oscillations scheme is clearly the less demanding in terms of kicker and pulser design. Transparent injection may however require the implementation of complex feed-forward systems that could be an additional complication. It is however a low risk option that has the capability to evolve towards more involved layout such as swap-out or longitudinal on-axis injection.

Table 6-2: Preliminary specifications of the kickers for the different injection schemes.

	Pulse width	Kick angle
Standard on-axis	1 SR turn (few μs)	2.0 mrad
Non-linear kicker	1 SR turn (few μs)	0.8 mrad (0.0→0.8mrad in 3mm)
Swap-out injection	2 SR bucket (~10ns)	1.0 mrad
Longitudinal injection	<1ns	1.0 mrad (0.5mrad with bump)
Shared oscillations	2 SR bucket (~10ns)	0.25 mrad

7 RF system for the ring

6 GeV Ultimate Source of Synchrotron Radiation is planned to be built in Russia. Storage ring scheme is based on the ESRF-EBS design [64-66]. Injection will be performed by means of top up electron linac that will be also used as FEL. For sources of synchrotron radiation, large values of beam currents are required. Excitation of Higher order modes (HOM) can lead to multi-bunch instabilities, emittance growth, beam breakup, etc. [67, 68].

Most of the synchrotron light sources use RF systems at 500 MHz. For historical reasons, the ESRF, APS and SOLEIL operate their RF systems at 352 MHz, the former LEP RF frequency. MAX-IV has implemented its RF system at 100 MHz and makes use of industrial components from the market for FM broadcast transmitters.

In the framework of CREMLIN+ we propose to adapt the 352 MHz ESRF-EBS RF system to fulfil the requirements of USSR. It is proposed to follow the general trend and feed each cavity individually with an RF power from RF solid state amplifier (SSA), which will provide modularity and intrinsic redundancy to the system.The general view of the accelerating cavity with an operating frequency of 357 MHz is shown in Figure 7-1.

This project has received funding from the European Union's Horizon 2020 research and innovation programme under grant agreement No. 871072.

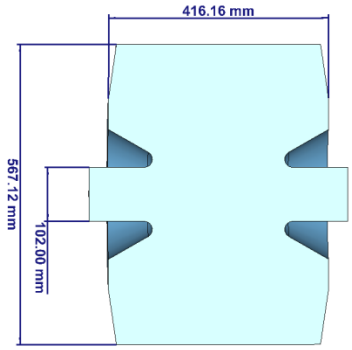

Figure 7-1: General view of an accelerating cavity at 357 MHz.

Based on the 500 MHz BESSY/ALBA cavity design, the ESRF has designed, optimized and implemented for EBS a HOM damped 352.37 MHz cavity, which is probably one of the best performing normal conducting cavities available today (352.37 MHz ESRF-EBS HOM damped single cell copper cavity) [69]:

- R/Q = 145 Ohm, Q0 = 34500 => Rs = 5 MΩ (BESSY cavity: 3.4 MΩ)
- Tuning range: -350 / +900 kHz
- 13 EBS cavities conditioned on the RF test stand to 750 kV each
- Nominal operation on EBS: 500 kV /cavity
- Exotic RF configuration: operated up to 650 kV / cavity with beam on EBS so far.

Cavity power considerations

We will further assume that the power radiated from Insertion devices (ID) can reach 1 MeV/turn, which reduces the energy acceptance from 5.6 % in Fig. x1 to 4.1 % and adds 200 kW of beam loading for the RF system.

Only 10 ESRF cavities, each operated at 500 kV, are sufficient to provide the required 5 MV of accelerating voltage for the USSR storage ring. The total power Pc dissipated in the cavities is then 250 kW. The power transferred to the beam at 200 mA varies between 400 kW for 2 MeV/turn radiation loss without ID and 600 kW for 1 MeV/turn additional ID radiation. The optimum coupling of the cavity to the generator, for which the RF system is matched, depends on the ID power according to

$$\beta_{opt} = \frac{P_c + P_{beam}}{P_c} = 2.6 \text{ to } 3.4 \quad \rightarrow \quad Safest\ value:\ \beta = 3.4\,.$$

A coupling of 3.4 will provide a good match as well as Robinson stability for a wide range of configurations. Fig. x2 shows the various power terms as a function of the beam current. Pgen gives the total generator power but doesn't include any provision for insertion losses due to the waveguide system. Fig. x2 has been computed for 1 MeV/turn ID radiation, for which a perfect match with vanishing reflection Prefl is obtained at 200 mA. Due to the Robinson detuning, the synchrotron frequency fs-Rob for coherent inphase oscillation of all bunches decreases from 781 Hz at 0 mA to 529 Hz at 200 mA. It is still far from the Robinson stability limit where fs-Rob vanishes. At 200 mA, the required generator power per cavity amounts to 85 kW.

This project has received funding from the European Union's Horizon 2020 research and innovation programme under grant agreement No. 871072.

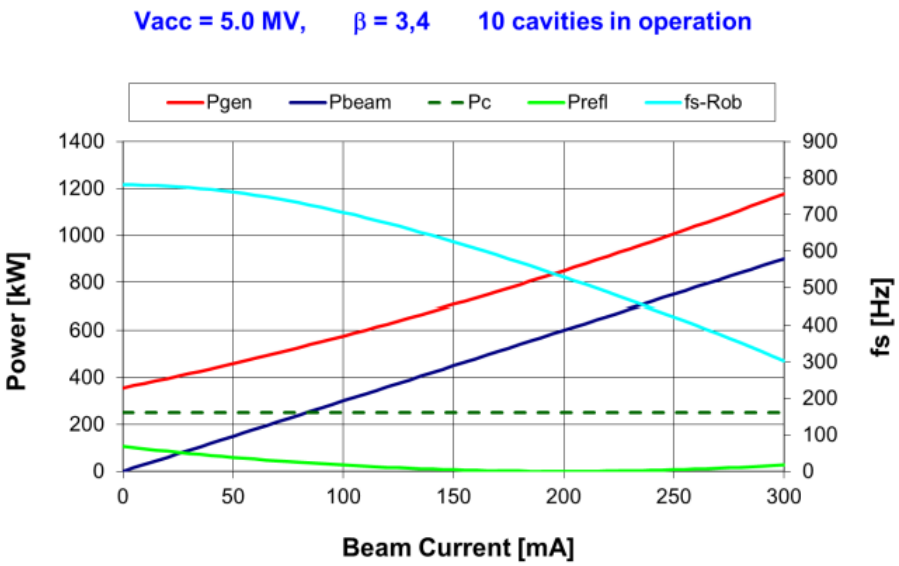

Figure 7-2: USSR beam loading diagram for ID radiation losses of 1 MeV/turn and cavity load angle of 0°.

When commissioning such a machine, the RF voltage for maximum lifetime will have to be re-optimized experimentally. For this, we have to provide a margin of ±1 MV for the accelerating voltage. The system should also remain operational in case one or, less likely and in the worst case, two cavities or SSA fail, which is in principle possible thanks to the modularity of the system. For this, we will check the power requirements if only 8 out of the 10 cavities are powered, the two passive ones being tuned off resonance in order not to couple to the beam. For this, we have checked the required generator power, the reflected power and the Robinson frequency fs-Rob at 200 mA without ID and with 1 MeV/turn ID radiation.

Table 7-1 shows that the chosen RF configuration can be operated under various conditions. It can tolerate the failing of up to two RF cavities and still no compromise on beam performance. At full ID power, without any margin, 97 kW is required per cavity to allow excursions up to 6 MV with 10 active cavities and 101 kW would allow operating with only 8 active cavities under slightly degraded conditions with 4 MV accelerating voltage. With 10 cavities at 4 MV and full ID power, fs-Rob is already very low and the DC Robinson instability would be reached at 235 mA. The voltage could not be reduced much further unless the coupling β would be increased. A power margin of at least 15 % should be provided for insertion losses in the waveguide system (due to mismatches and dissipation) as well as for some control tolerance in the operation parameters. An additional power reserve of 100 kW in total, i.e. 10 kW per cavity, should be foreseen for the operation with an additional harmonic RF system for bunch lengthening[4]. Including these margins, the RF power amplifiers should therefore be dimensioned for at least 125 kW maximum output power.

[4] At high beam current even an active harmonic copper cavity draws power from the beam that generates substantial reverse power for the harmonic generator. The main RF system can therefore be loaded by up to 50 kW additional beam power for a 4th harmonic RF system operated in bunch lengthening on USSR. Another 50 kW power margin must be provided as gain reserve for the mandatory stabilization by means of a fast RF feedback.

This project has received funding from the European Union's Horizon 2020 research and innovation programme under grant agreement No. 871072.

Table 7-1: Main RF parameters at 200 mA for a cavity coupling β = 3.5, optimized for 10 active cavities, 5 MV accelerating voltage and ID radiation of 1 MeV/turn (in green in the table). Also shown: degraded operation with only 8 cavities in operation.

Number of active cavities	ID radiation loss per turn	Accelerating voltage	Pgen per Cavity	Prefl per cavity	fs-Rob
10	0	4 MV	56 kW	0	426 Hz
		5 MV	66 kW	1.2 kW	598 Hz
		6 MV	80 kW	4.4 kW	731 Hz
	1 MeV/turn	4 MV	78 kW	2.2 kW	265 Hz
		5 MV	85 kW	0	529 Hz
		6 MV	97 kW	1.4 kW	689 Hz
8	0	4 MV	75 kW	0.3 kW	508 Hz
		5 MV	93 kW	3.6 kW	665 Hz
		6 MV	*6 MV not required for degraded configuration with 8 cavities*		
	1 MeV/turn	4 MV	101 kW	0.7 kW	398 Hz
		5 MV	115 kW	0.7 kW	607 Hz
		6 MV	*6 MV not required for degraded configuration with 8 cavities*		

High order modes

For an accelerating cavity the electrodynamic characteristics (EDC) [70] of the fundamental mode (Table 7-2) and HOM were carried out [71].

Table 7-2: EDC of Accelerating Cavity.

EDC	**Values**
f, MHz	357
Q, $\times 10^3$	41
$R_{sh\ eff}$, MΩ	10

The frequency dependence of the longitudinal shunt impedance for monopole HOMs is shown in Figure 7-3. One could see that that the shunt impedance of parasitic HOMs accelerating cavity can reach values of up to 10^6 Ohm. Electrodynamic characterisics of operationl mode and HOMs are presented in Table 7-3.

This project has received funding from the European Union's Horizon 2020 research and innovation programme under grant agreement No. 871072.

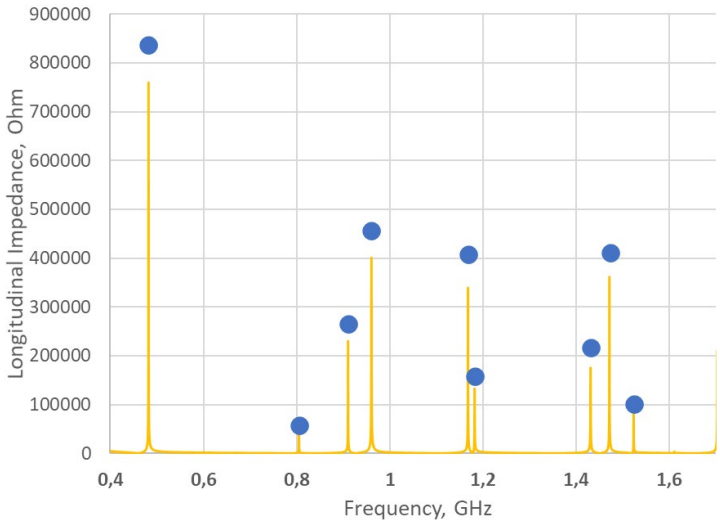

Figure 7-3: Frequency dependence of the longitudinal shunt impedance for monopole modes for an accelerating cavity at 357 MHz. Graph – result of wakefield simulations, dots – results of eigenmode simulations.

The field distributions for the most dangerous transverse and longitudinal modes are presented in Figure 7-4 and Figure 7-5.

One of the requirements for EBS-ESRF cavity design was to ensure unconditional beam stability up to currents of 1000 mA. For EBS-ESRF longitudinal coupled bunch instability threshold at 200 mA is $R_{HOM} \cdot f_{HOM}$ = 16 kW·GHz (Figure 7-5) [67].

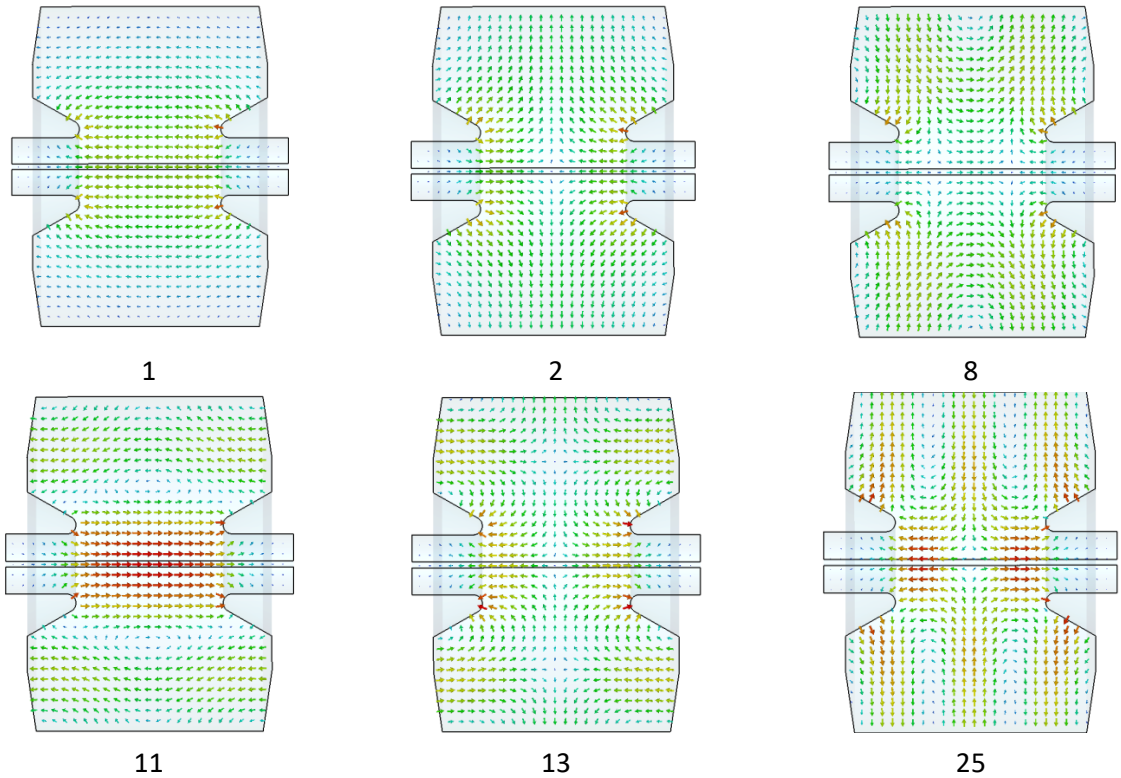

Figure 7-4: Field distribution of monopole HOMs (numbers indicate corresponding mode form Table 7-2).

This project has received funding from the European Union's Horizon 2020 research and innovation programme under grant agreement No. 871072.

Table 7-3: Electrodynamic characterisics of operationl mode and HOM.

#	Type	Frequency, MHz	Q, 10^4	$R_{sh\parallel}/Q_0$,Ohm	$R_{sh\parallel}$, Ohm	$R_{sh\perp}/Q_0$,Ohm/m	$R_{sh\perp}$, Ohm/m
1	E010	350	4,1	290	$1,2\cdot10^7$		
2	E011	482	3,6	47	$1,7\cdot10^6$		
3	H111	501	4,6			4,7	$2,2\cdot10^5$
4	H211	637	5,5			$1,4\cdot10^{-4}$	7,8
5	E110	641	6,1			26	$1,6\cdot10^6$
6	H121	794	4,8			24	$1,1\cdot10^6$
7	H311	799	5,7			$4,8\cdot10^{-6}$	0,27
8	E012	805	4,6	2,5	$1,2\cdot10^5$		
9	E111	828	5,1			0,7	$3,3\cdot10^4$
10	E210	876	8,0			$1,2\cdot10^{-4}$	9,2
11	E020	911	5,8	9,1	$5,3\cdot10^5$		
12	Quad	912	5,8			$3,8\cdot10^{-4}$	22
13	E021	961	3,7	25	$9,1\cdot10^5$		
14	Octupole	969	5,7			$8,9\cdot10^{-6}$	0,5
15	Dipole	985	9,2			$4,3\cdot10^{-5}$	3,9
16	Quad	992	5,7			$6,5\cdot10^{-4}$	0,4
17	Sextupole	1026	6,2			$1,8\cdot10^{-6}$	0,1
18	Dipole	1070	3,9			8,3	$3,3\cdot10^5$
19	Dipole	1074	5,3			0,3	$1,4\cdot10^4$
20	Sextupole	1088	8,7			$1,3\cdot10^{-6}$	0,1
21	Dipole	1091	5,1			1,9	$9,5\cdot10^4$
22	Tentupole	1143	5,6			$1,7\cdot10^{-7}$	$9,8\cdot10^{-3}$
23	Octupole	1164	6,1			$1,1\cdot10^{-5}$	0,7
24	Sextupole	1168	6,1			$3,5\cdot10^{-2}$	$2,1\cdot10^5$
25	E013	1169	6,7	12	$8,2\cdot10^5$		
26	E022	1183	4,8	6,6	$3,2\cdot10^5$		
27	Quad	1184	7,8			$2,8\cdot10^{-4}$	22
28	Quad	1194	5,6			$6,6\cdot10^{-5}$	3,7
29	Quad	1210	7,6			$9,6\cdot10^{-5}$	7,3
30	Dipole	1232	5,6			4,3	$2,4\cdot10^5$

From Figure 7-6 we can see that it is necessary to significantly decrease the shunt impedance values of HOMs. To reduce these values, it is proposed to add HOM couplers to the system.

This project has received funding from the European Union's Horizon 2020 research and innovation programme under grant agreement No. 871072.

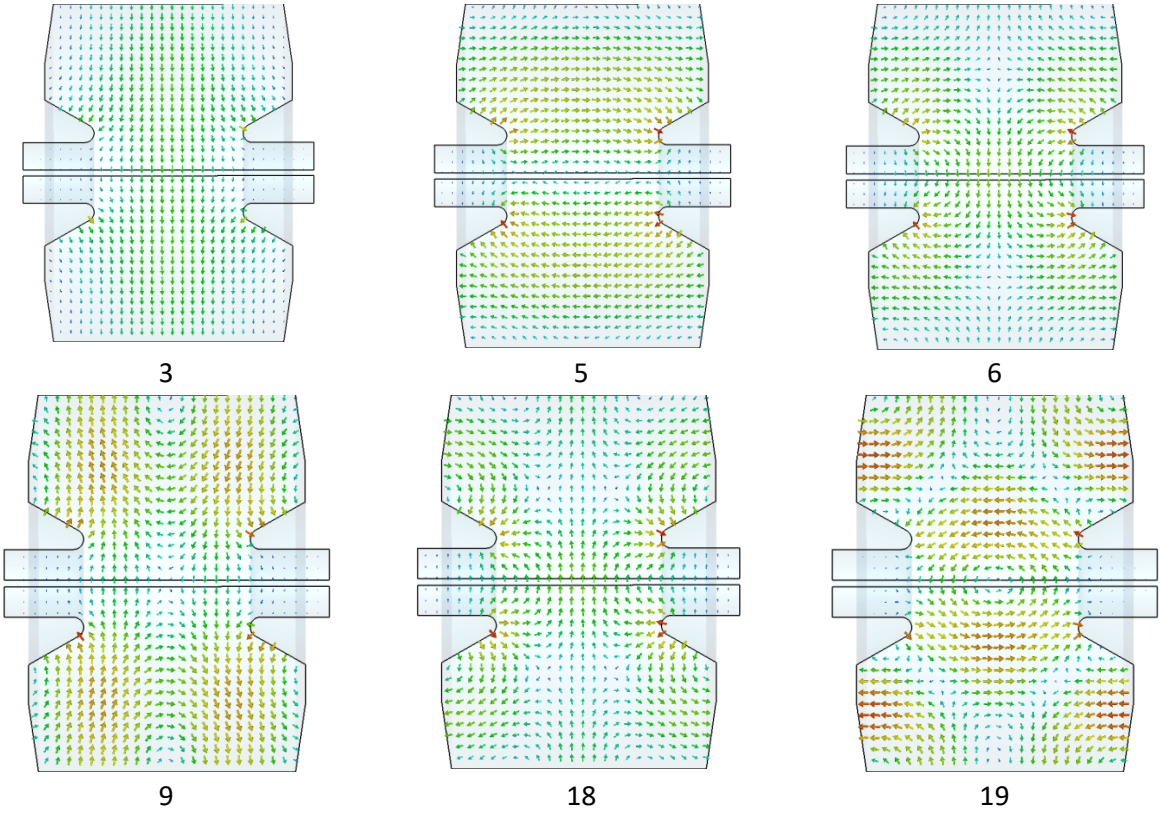

Figure 7-5: Field distribution of transverse HOMs (numbers indicate corresponding mode form Table 7-2).

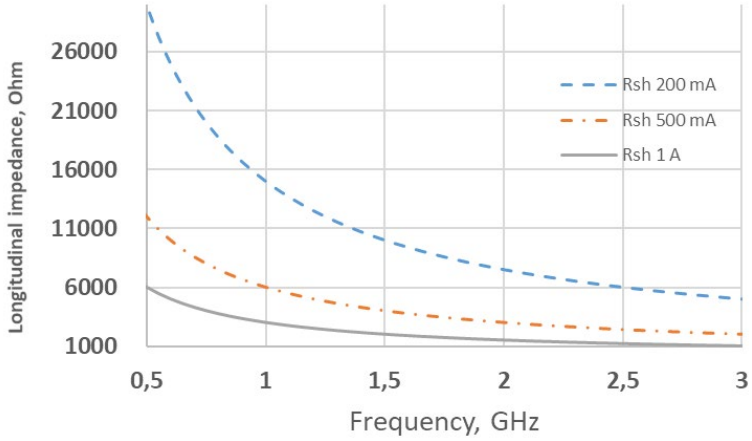

Figure 7-6: Threshold for longitudinal impedance necessary for unconditional beam stability for 200, 500 and 1000 mA beam current.

HOM damping using waveguides

As an initial variant, it was proposed to use a system for HOM damping equipment similar to that used in the DAFNE accelerator (Figure 7-7) [66]. In this design, there are three waveguides for HOM damping, located at an angle of 120 degrees with respect to each other. The presence of three waveguides is a prerequisite for damping all polarizations of higher order modes.

This project has received funding from the European Union's Horizon 2020 research and innovation programme under grant agreement No. 871072.

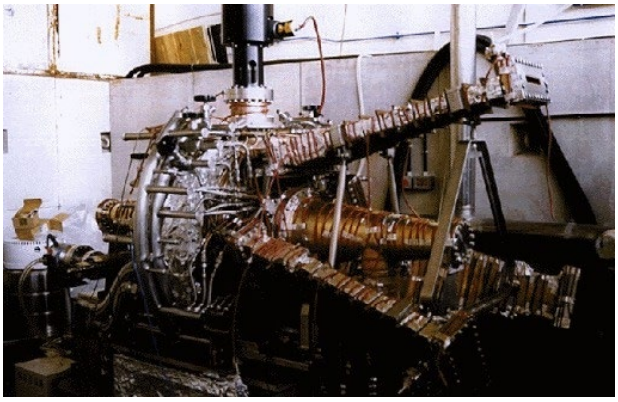

Figure 7-7: General view of an accelerating cavity at 350 MHz.

In such systems, dipole and parasitic monopole waves will excite a TM_{10} wave in the waveguide. The length of the wide wall of the cavity will determine the cutoff frequency of the H_{10} wave. The length of the narrow wall will have no effect. The cutoff frequency should be above 350 MHz (to prevent damping of the fundamental wave) but below 482 MHz (the frequency of the first monopole wave). The waveguide width is chosen 340 mm, and the thickness is 10 mm.

In the calculations, a long waveguide length (1000 mm) was used to prevent attenuation of the operational mode (Figure 7-8). The energy of the operational mode decays exponentially in the waveguide, but at short waveguide lengths, part of the power reaches the load, which leads to a decrease in the loaded Q-factor of the main wave.

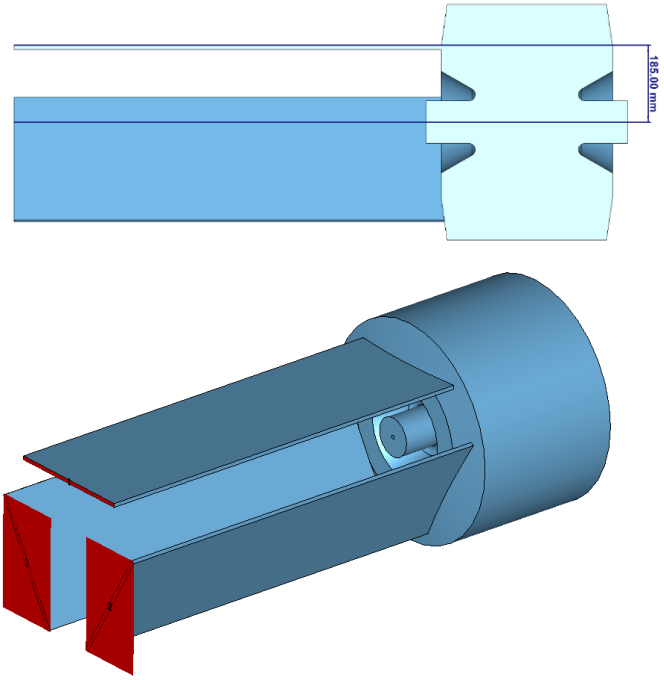

Figure 7-8: General view of an accelerating cavity at 350 MHz.

The dependence of the longitudinal and transverse shunt impedance for monopole and transverse modes on frequency for an accelerating cavity at 350 MHz with HOM output devices and a comparison of the damping results are presented in Figure 7-9. It is possible to significantly reduce the value of the transverse and longitudinal shunt impedance for the majority of HOMs.

This project has received funding from the European Union's Horizon 2020 research and innovation programme under grant agreement No. 871072.

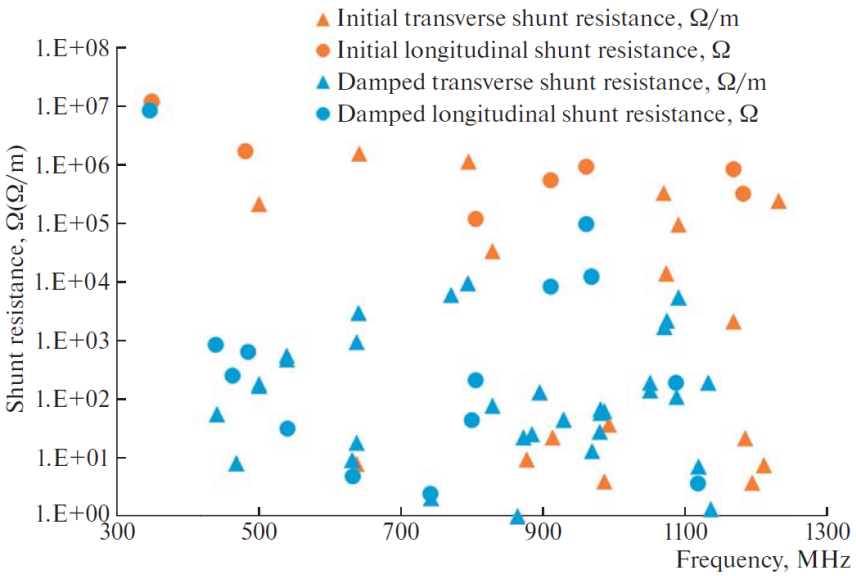

Figure 7-9: Comparison of the longitudinal and transverse shunt resistance for monopole and transverse modes of oscillation versus frequency for an accelerating resonator at 350 MHz without HOM output devices and with HOM output devices.

HOM damping using corrugated waveguides

As a baseline design for HOM damping it is proposed to use the design options applied in BESSY and ESRF (Figure 7-10) [72]. This design assumes three corrugated waveguides for HOM damping, located at an angle of 120 degrees with respect to each other. The presence of three waveguides is a prerequisite for damping all polarizations of higher order modes [73, 74].

Figure 7-10: Accelerating cavity of the BESSY accelerator (left) and ESRF (right).

In such systems, dipole and parasitic monopole mode will excite an TE_{11}-type mode in the waveguide (Figure 7-11). The cutoff frequency should be above 357 MHz (to prevent fundamental mode damping) but below 442 MHz (first monopole frequency). The height of the corrugation ribs and the diameter of the waveguide will determine the cutoff frequency of the TE_{11} mode (the rest of the parameters have no significant effect on this parameter).

This project has received funding from the European Union's Horizon 2020 research and innovation programme under grant agreement No. 871072.

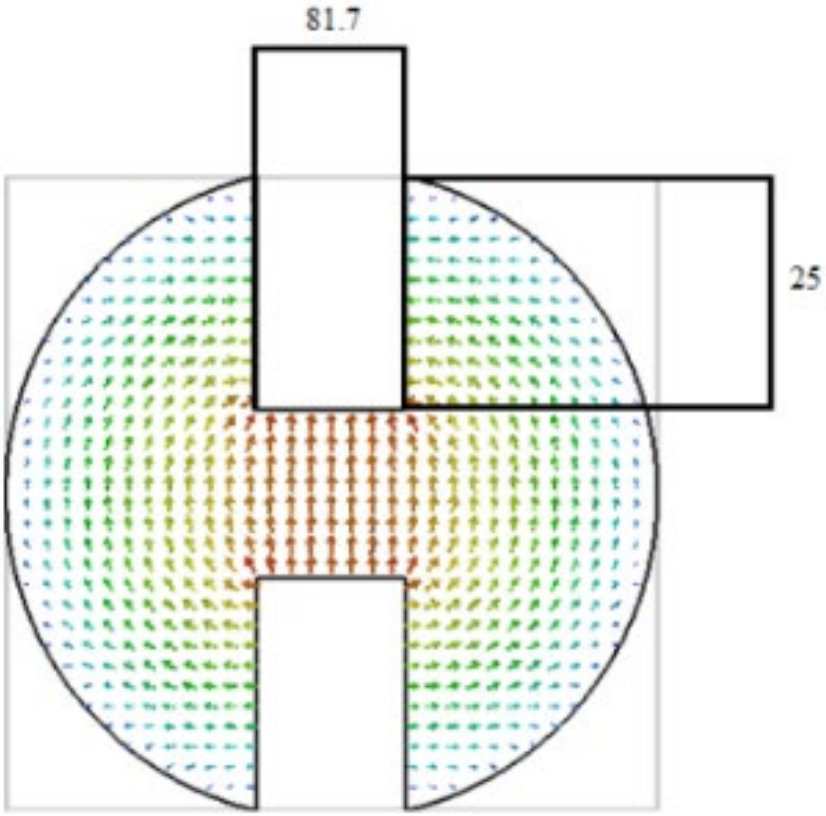

Figure 7-11: Distribution of TE_{11} mode electric field in a corrugated cylindrical waveguide.

The graph of the dependence of the cutoff frequency of the TE_{11} mode on the outer radius of the waveguide, as well as the height and width of the corrugation, is shown in Figure 7-12.

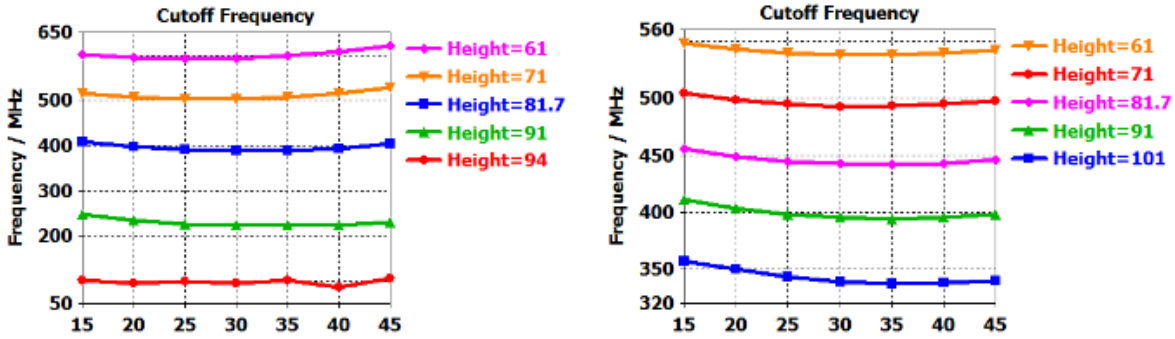

Figure 7-12: Dependence of the cutoff frequency of the TE_{11} mode on the outer radius of the waveguide, as well as the height and width of the corrugation.

The waveguide diameter is 220 mm, the corrugation height is 81.7 mm, and their thickness is 25 mm, since with these parameters the cutoff frequency is 437 MHz.

The lengths of the HOM dampers are dimensioned such that the non-propagating decaying fields at 357 MHz are sufficiently low at the HOM absorbers not to affect the quality factor of the accelerating mode (Figure 7-13). The dependence of the external Q-factor of the fundamental wave on the waveguide length is shown in Figure 7-14.

This project has received funding from the European Union's Horizon 2020 research and innovation programme under grant agreement No. 871072.

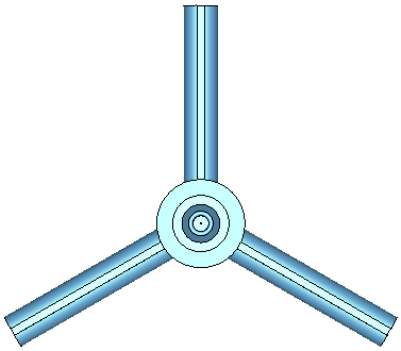

Figure 7-13: General view of an accelerating cavity with three HOM waveguides

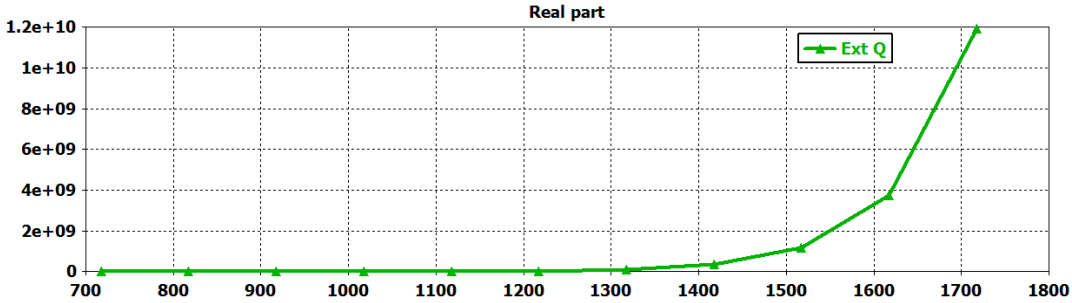

Figure 7-14: Dependence of the external Q-factor of the fundamental wave on the waveguide length.

The dependence of the longitudinal and transverse shunt impedance for monopole and transverse modes of oscillations on frequency for an accelerating cavity at 357 MHz with HOM waveguides and a comparison of the damping results are presented in Figure 7-15.

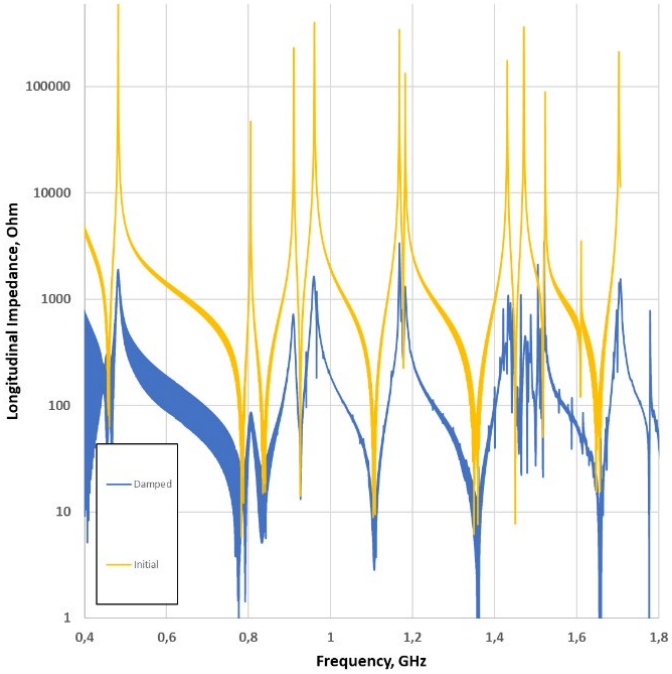

Figure 7-15: Comparison of the longitudinal shunt impedance for monopole HOMs for an initial accelerating cavity and with HOM waveguides.

This project has received funding from the European Union's Horizon 2020 research and innovation programme under grant agreement No. 871072.

From Figure 7-15 we can see that longitudinal impedance values of HOMs were reduced by 2-3 orders of magnitude.

Comparison of longitudinal shunt impedance for monopole HOMs for accelerating cavity with HOM waveguides with threshold longitudinal shunt impedance values necessary for unconditional beam stability for 200, 500 and 1000 mA presented on Figure 7-16.

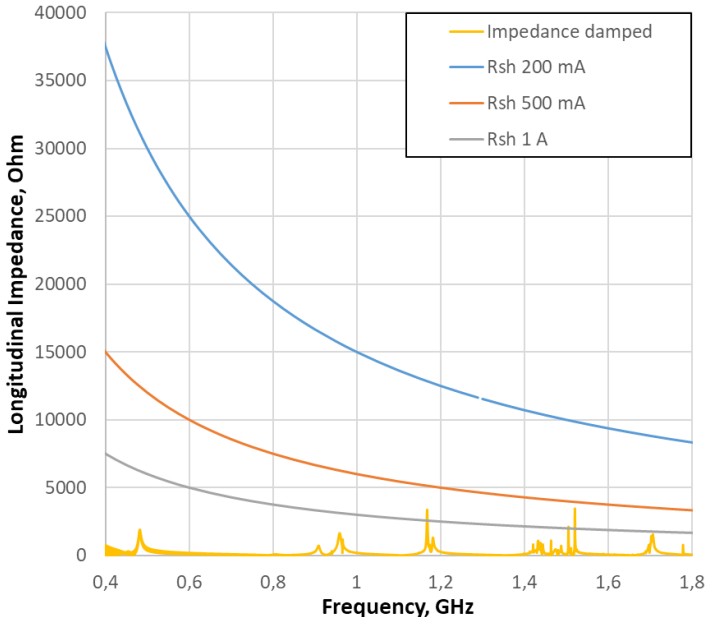

Figure 7-16: Longitudinal shunt impedance for monopole HOMs for accelerating cavity with HOM waveguides and threshold longitudinal shunt impedance values necessary for unconditional beam stability for 200, 500 and 1000 mA.

From data presented on Figure 7-16 it is clear that the impedance values achieved ensure unconditional beam stability for current up to 500mA. However, it is necessary to carry out additional studies if stability at higher currents of up to 1000 mA is necessary. Some examples of HOMs that exceed 1000 mA threshold are presented on Figure 7-17.

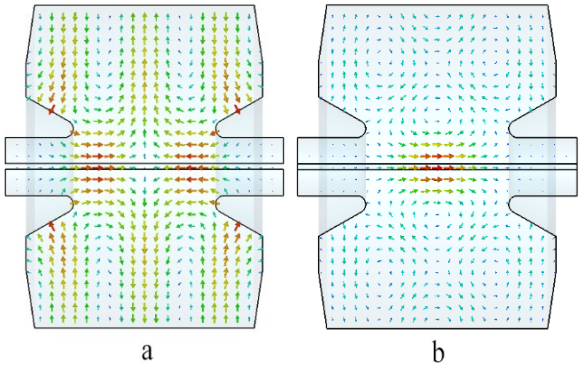

Figure 7-17: Electromagnetic field distribution of HOMs. (a) – 1168 MHz mode, (b) – 1528 MHz mode.

Thus, achieved impedance values satisfy requirements for unconditional beam stability for currents up to 500 mA. However, it is necessary to conduct further studies in order to achieve stability up to 1000 mA. Further research is currently underway.

This project has received funding from the European Union's Horizon 2020 research and innovation programme under grant agreement No. 871072.

8 Insertion devices

Insertion devices of various types are used on all modern synchrotron light sources [75]. These are classic out of vacuum insertion devices with permanent magnets, electromagnetic insertion devices, various types of in-vacuum insertion devices - both cryogenically cooled with permanent magnets and superconducting [76]. When working on the project, we decided not to limit ourselves to one of the types, but to explore all existing possibilities. We have selected permanent magnet devices as the most mature technology. During the first stage of the project, we formulated a preliminary list of stations of the first stage (see Table 8-1). For these stations, the researchers had previously selected a list of insertion devices.

Table 8-1: Beamilnes for Phase One of the USSR4 synchrotron.

Beamline Title	Photon Energy Range, keV	Source type
Multiscale x-ray imaging	10—300	Undulator+three pole SCW
Classical crystallography	5—80	CPMU23 + U35
Surface and interfaces	7—40	U27 V U35
XPCS and SAXS	5—25	U21 + U25
HAXPES - Hard-x-ray PES	2—20	U33
Nanodiffraction and nanofocusing CDI	5—40	U27 + U35
Magnetic scattering	2.5—27	APPLE II/DELTA/HELIOS
Classical PES and ARPES	0.1—2	UE125, polarization control
XAFS and QXAFS	5—30	U35 + U40
Serial crystallography	5—20	U24 V U35
Time resolved experiments	5—30	U27 + U35

As parameters of the insertion devices in the calculations, we used the parameters of the ESRF synchrotron ID obtained from [76] (Figure 8-1). As a first candidates were chosen out of vacuum permanent magnet devices – U27&U35

The analysis of the needs of experimental stations of the first stage is carried out. The analysis showed that the most popular are medium-period undulators with a period from 23 to 35 mm, providing effective generation of radiation in a wide spectral range. According to the formulas presented in XDB [78], we calculated the brightness of the source, and using the Orange Suite [79], radiation flux (Figure 8-2). The standard out of vacuum ESRF undulator with a period of 27 mm was chosen as the first model. The partner provided some drawings of such an undulator of the 1996 model.

Based on the provided documentation (Figure 8-3), we conducted a primary study of the design of the undulator.

The documentation provided did not contain data on the degree of magnetization and the materials used. They were taken from the works [80, 81]. Based on this model and the publication with parameters, we calculated the fields in the undulator structure using the ANSYS Maxwell 3D program. In the provided drawings there was also no data on the end elements of the undulator. The design of the holder in the provided drawings were given for the type C end elements currently used on the ESRF synchrotron. Its initial block consists of a number of magnets, while those of them that create the vertical component of the field are divided by the axis into two separate blocks with

This project has received funding from the European Union's Horizon 2020 research and innovation programme under grant agreement No. 871072.

oblique magnetization directed opposite to each other. Possible variants of finite elements are shown in Figure 8-4 [82].

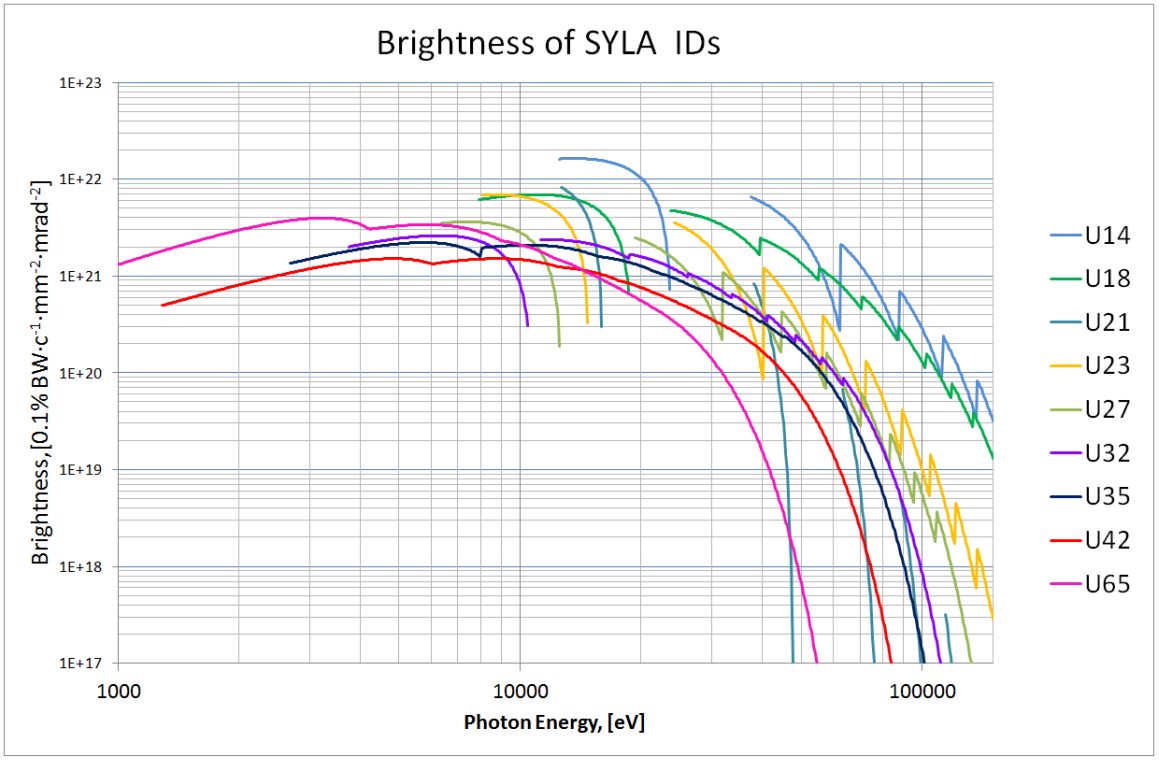

Figure 8-1: Spectral brightness of various undulators at USSR machine. Horizontal beam emittance was taken 70 pm·rad, coupling 10%, energy spread 0.1%.

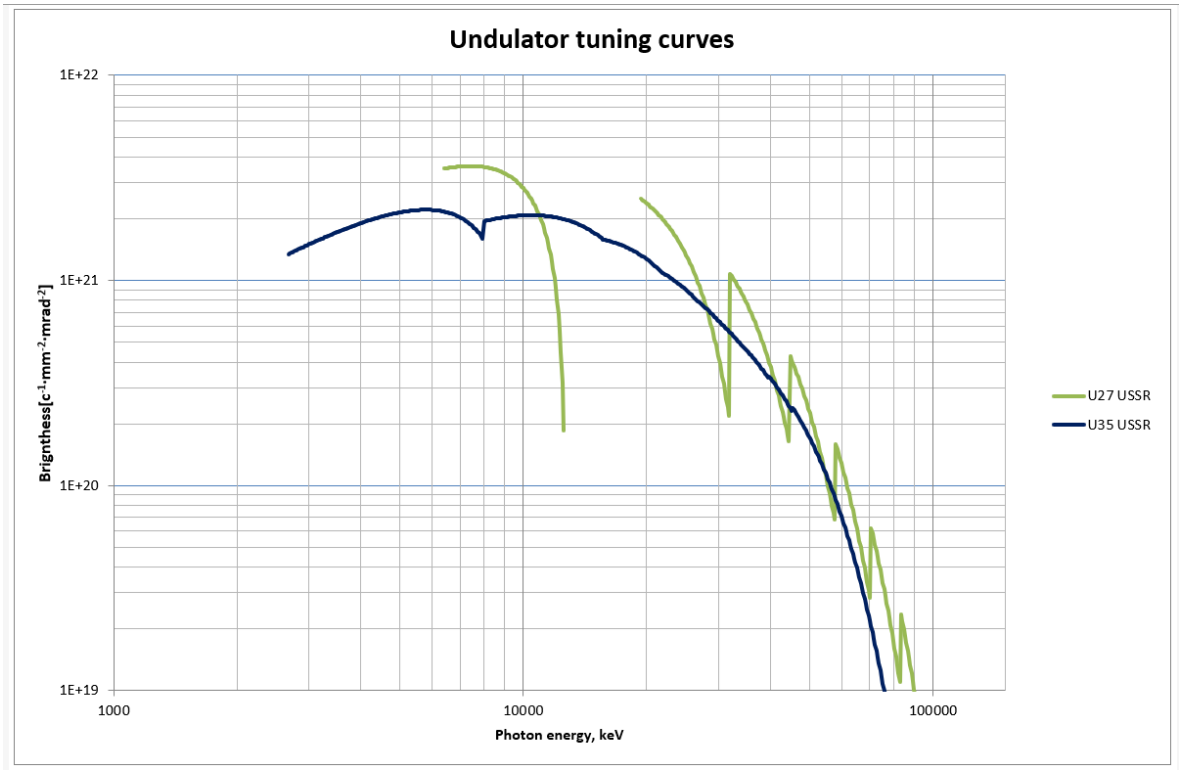

Figure 8-2: Tuning curves for U27 and U35 undulators.

This project has received funding from the European Union's Horizon 2020 research and innovation programme under grant agreement No. 871072.

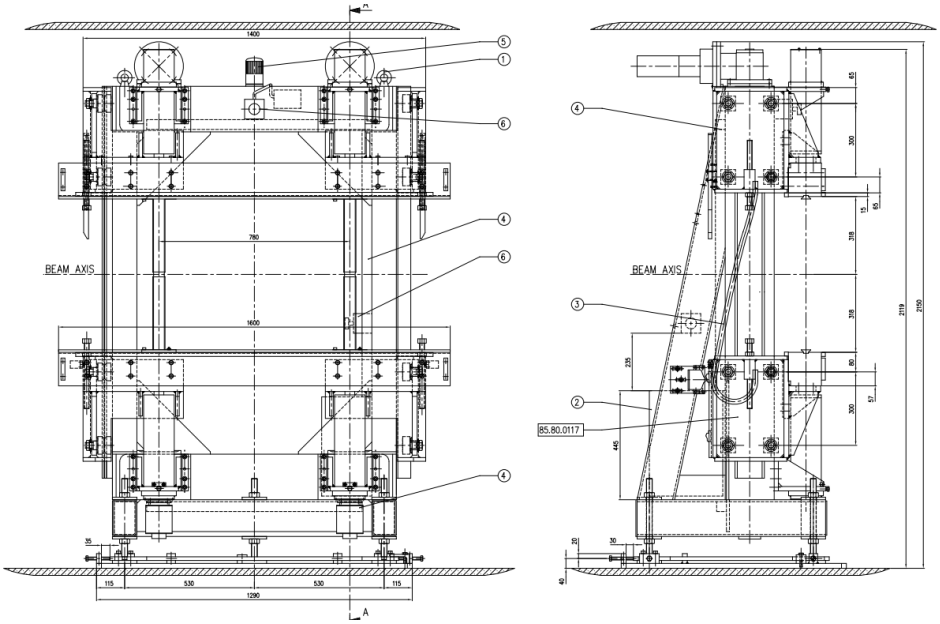

Figure 8-3: Mechanical design and drawings provided by ESRF.

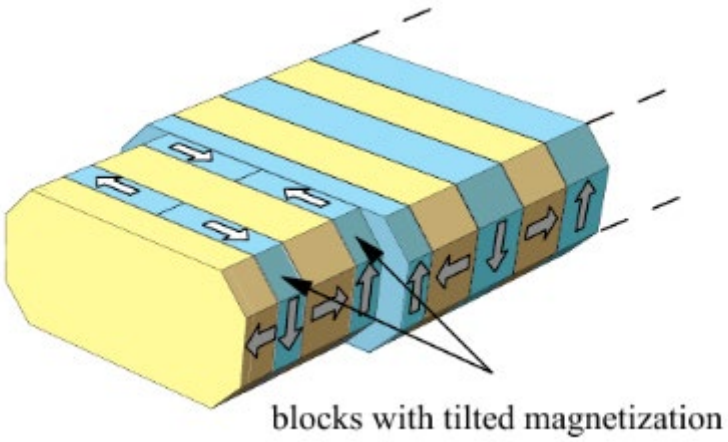

Figure 8-4: 3D view of C type termination [80].

Based on the article [82] and the book [76] we have performed the selection of the required values in the ANSYS program (Figure 8-5 & Figure 8-6). As a result of the selection, it was possible to achieve the conversion of the first and second integrals to zero with the required accuracy.

This project has received funding from the European Union's Horizon 2020 research and innovation programme under grant agreement No. 871072.

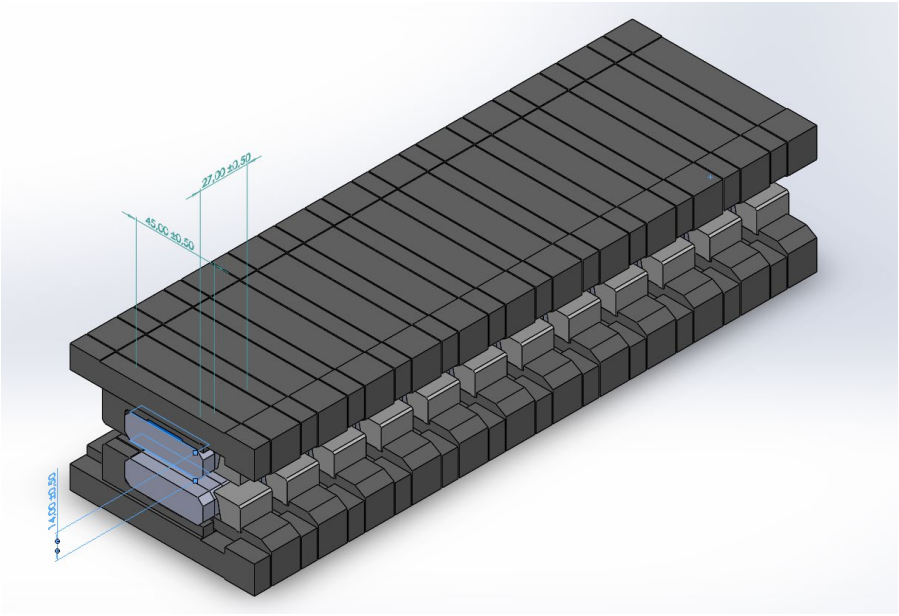

Figure 8-5: 3D model of magnetic structure with the holder, used for simulations.

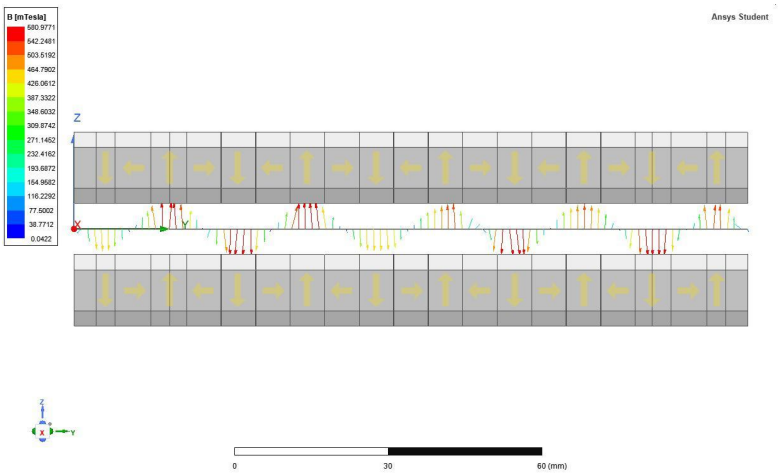

Figure 8-6: Magnetic field distribution inside the undulator.

The values of magnetic fields can now be processed to obtain the first integral of the magnetic field. The first integral (accumulated error) is 6.7 10^{-5} T m, which meets the requirements for ESRF undulators. For comparison, we simulate an undulator without end elements and derive the distribution of magnetic fields in it (Figure 8-7), as well as the error of the first integral in comparison with an undulator with end elements (Figure 8-8). Without end elements, the error reaches more than $3000 \cdot 10^{-6}$ T·m that exceeds the error with the end elements by 50 times. Obtained second integral of the magnetic field value is $89.539 \cdot 10^{-6}$ T·m^2.

For the practical implementation of the calculated devices, it is planned to create a specialized laboratory of magnetic measurements during the USSR4 project.

This project has received funding from the European Union's Horizon 2020 research and innovation programme under grant agreement No. 871072.

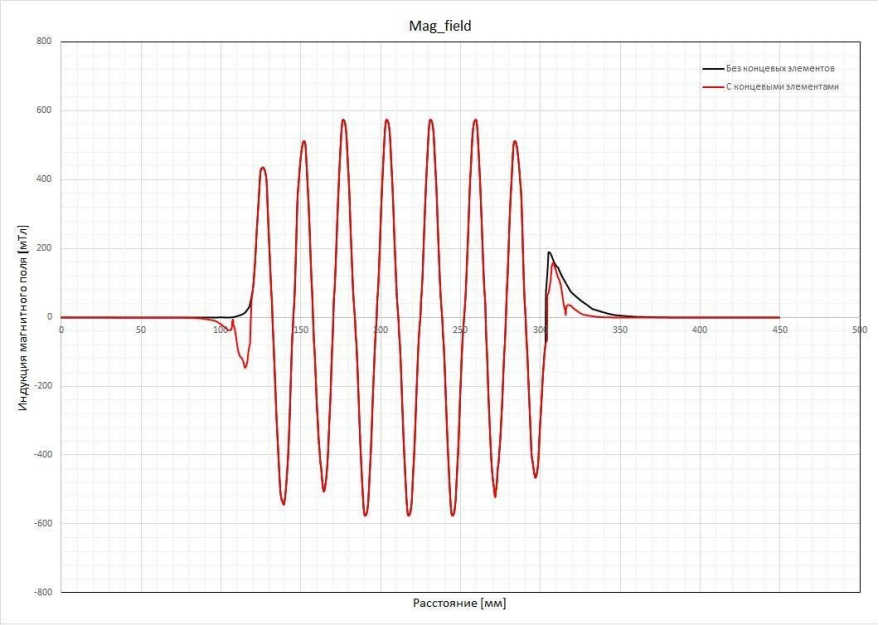

Figure 8-7: Distribution of magnetic fields in the undulator with and without terminations.

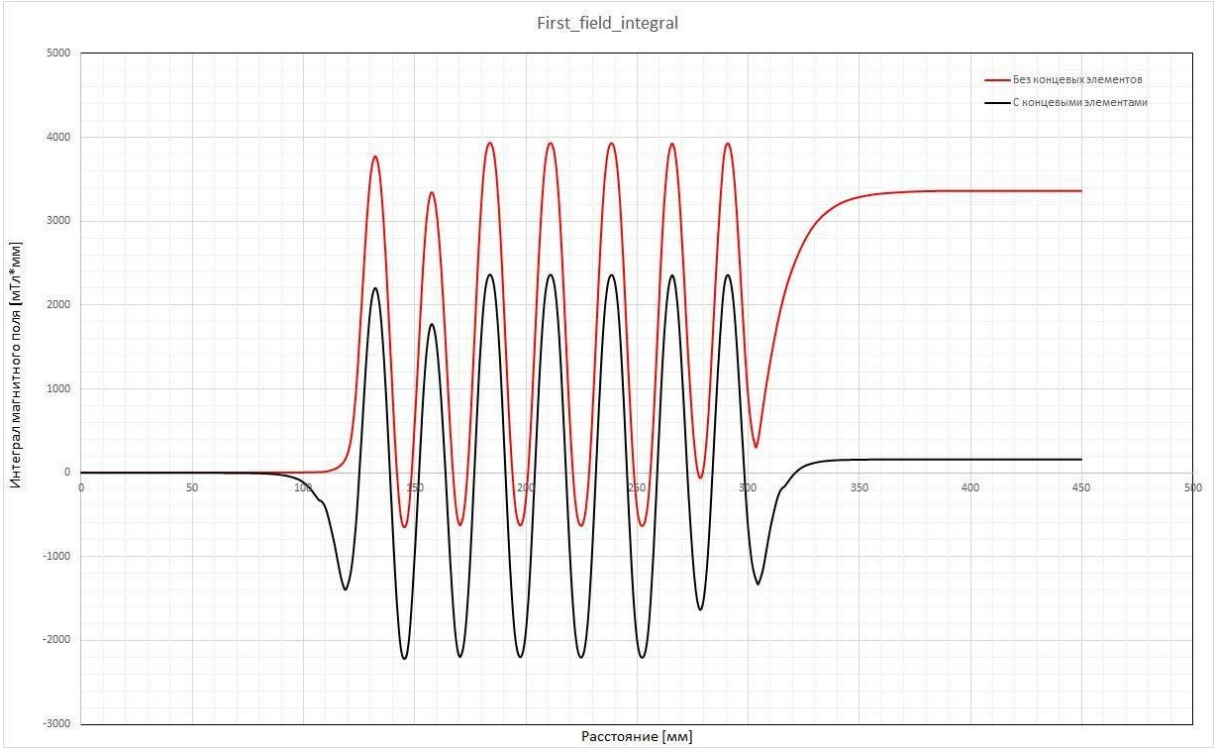

Figure 8-8: – First field integral with and without with and without terminations.

This project has received funding from the European Union's Horizon 2020 research and innovation programme under grant agreement No. 871072.

9 Bibliography

1. S.M.Liuzzo, N.Carmignani, L.Carver, T.Perron, R.Versteegen, S.White, Cremlin+ Task4.1 ESRF report 2020, ESRF Special Report 01-2021-BD, 2021, https://syncandshare.desy.de/index.php/s/PCbJQFm5BGSNKcd
2. S.M.Liuzzo, L.Hoummi, L.Carver, F.Cianciosi,G.Le Bec, J.Jacob, S.White, Cremlin+ Task4.1 ESRF report 2021, ESRF Technical Report, ASDDOC-Beam_Dynamics-2022-002, 2022, https://syncandshare.desy.de/index.php/s/SLQoMFnpmSgoN4X
3. Xiaobiao Huang, Potential performance limit of Storage Rings, IPAC 2017, Copenhagen, Denmark, https://accelconf.web.cern.ch/ipac2017/papers/wepab114.pdf
4. V. Serriere et al. “352.2 MHz HOM Damped Normal Conducting ESRF Cavity: Design and Fabrication”, IPAC 2011, MOPC004
5. A. Piwinski, arXiv preprint physics/9903034, 1999 - arxiv.org, https://arxiv.org/abs/physics/9903034
6. N. Carmignani et al., “ Linear and nonlinear optimizations for the ESRF upgrade lattice”, TUPWA013, Proceedings of IPAC’15, Richmond, Virginia,USA (2015).
7. Song Lin, "NGPM – a NSGA-II program in Matlab"
8. R. Versteegen et al., "Modeling of Beam Losses at ESRF", TUPWA016, Proceedings of IPAC 2015, Richmond, Virginia, USA (2015)
9. A. Piwinski, "The Touschek Effect in Strong Focusing StorageRings", arXiv:physics/9903034
10. K. Deb, et al., "A fast and elitist multiobjective genetic algo-rithm: NSGA-II." Evolutionary Computation, IEEE Transac-tions on 6.2 (2002): 182-197
11. https://github.com/USSR-Lattice/SR/releases/tag/V4-SB
12. N.Carmignani et al., Operation improvements and emittance reduction of the ESRF booster, IPAC2018, Vancouver, doi:10.18429/JACoW-IPAC2018-THPMF017
13. Sun, C. et al., Small-emittance and low-beta lattice designs and optimizations, Phys. Rev. ST Accel. Beams, 2012, doi:10.1103/PhysRevSTAB.15.054001
14. A. Streun. The anti-bend cell for ultra-low emittance storage ring lattices. Nuclear Instruments and Methods in Physics Research A, 737:148–154, 2014
15. B.Riemann and A.Streun. Low emittance lattice design from first principles: Reverse bending and longitudinal gradient bends. Physical Review Accelerators and Beams. 22. 10.1103/PhysRevAccelBeams.22.021601 (2019)
16. APS Upgrade Project Preliminary Design Review Report, 2017, https://www.aps.anl.gov/APS-Upgrade/Documents (accessed February 1, 2019)
17. H. Wiedemann, Particle Accelerator Physics, Third edition, Springer, 2007, p. 305
18. https://github.com/USSR-Lattice/SR/releases/tag/V1-RB
19. S.Y. Lee, Accelerator Physics, Second Edition, WSP, 2004, p.418
20. K. Deb, A. Pratap, S. Agarwal and T. Meyarivan, "A fast and elitist multiobjective genetic algorithm: NSGA-II" in IEEE Transactions on Evolutionary Computation, vol. 6, no. 2, pp. 182-197, April 2002, doi: 10.1109/4235.996017
21. https://inspirehep.net/files/cee057f2f499a62f86693cb75dbc68fe
22. V.S. Dyubkov, T.V. Kulevoy, E.D. Tsyplakov, “Lattice Options With Reverse Bending Magnets For Ussr Hmba Storage Ring“, Proc. of RuPAC2021, Alushta, Russia 2021, pp. 280 - 282. doi:10.18429/JACoW-RuPAC2021-TUPSB26

This project has received funding from the European Union‘s Horizon 2020 research and innovation programme under grant agreement No. 871072.

23. Recent developments of Monte-Carlo codes MolFlow+ and SynRad+. M. Ady, R. Ker-sevan. 10th Int. Particle Accelerator Conf., Melbourne, Australia - doi:10.18429/JACoW-IPAC2019-TUPMP037 http://accelconf.web.cern.ch/AccelConf/ipac2019/papers/tupmp037.pdf
24. Molflow+ A Monte-Carlo Simulator package developed at CERN / https://molflow.web.cern.ch/content/about-molflow
25. SynRad+/ https://molflow.web.cern.ch/content/about-molflow
26. ESRF Upgrade Programme Phase II (2015-2022) - "EBS Storage Ring Technical Report". - 2018
27. OpticsBuilder documentation. https://molflow.web.cern.ch/opticsbuilder-documentation
28. https://molflow.web.cern.ch/node/139
29. C.Benabderramane, https://accelconf.web.cern.ch/ipac2018/papers/wepmk009.pdf
30. D. Varentsov et al. «Commissioning of the PRIOR proton microscope». Review of Scientific Instruments 87, issue 2, 2016, p.023303/1–023303/8
31. I.M. Kapchinskiy, V.S. Skachkov et al. «Drift Tubes for a Focusing Channel of Ion Linear Accelerator». Proc. of the PAC-1989, IEEE, vol.2, Chicago, Il., USA, 1989, p.1073
32. V.I. Shvedunov et al. «A 70 MeV racetrack microtron», NIM A: Volume 550, Issues 1–2, 2005, p.39
33. V.I. Shvedunov et al. «A racetrack microtron with high brightness beams», NIM A: Volume 531, Issue 3, 2004, p. 346
34. V.S Skachkov. «Quasi-sheet multipole permanent magnets», NIM A: Volume 500, Issues 1–3, 2003, p.43
35. V.S. Skachkov, A.N. Ermakov, V.I. Shvedunov. «Quasi-sheet quadrupole triplets», NIM A: Volume 524, Issues 1–3, 2004, p.39
36. V.S Skachkov, G.A Novikov. «Large quasi-sheet dipole magnets», NIM A: Volume 526, Issue 3, 2004, p.199
37. Kantcyrev A.V. et al. «Proton microscope at TVN-ITEP accelerator complex». PTE, 2014, No 1, p. 5–14
38. H. Ohkuma, "Top-up Operation in Light Sources", Proc. of EPAC'08, pp.36-40 (2008)
39. "The Red Book", ESRF (1987)
40. "The Orange Book", ESRF (2015)
41. S. White, J. Chavanne, M. Dubrulle, G. Le Bec, E. Plouviez, P. Raimondi, "Damping of injection perturbations at the European Synchrotron Radiation Facility", PRAB, Vol.22, 032803 (2019)
42. K. Harada, Y. Kobayashi, T. Miyajima, and S. Nagahashi, "New injection scheme using a pulsed quadrupole magnet in electron storage rings", Phys. Rev. ST Accel. Beams, 10, 123501 (2007)
43. H. Takaki et al., "Beam Injection with a Pulsed Sextupole Magnet in an Electron Storage Ring", Phys. Rev. ST Accel. Beams, 13, 020705 (2010
44. R. Takai et al., "Beam Profile Measurement during Top-up Injection with a Pulsed Sextupole Magnet", Proc. of DIPAC'11, pp. 305-307
45. M. Borland, "A super-bright storage ring alternative to an energy recovery linac", Nucl. Instrum. and Methods in Phys. Research Section A, Vol. 557, pp. 230-235 (2000)
46. L. Emery and M. Borland, "Possible Long-Term Improvements to the Advanced Photon Source", Proc. of PAC 03, pp. 256-258
47. S. Henderson, "Status of the APS Upgrade Project", Proc. of IPAC 15, pp. 1791-1793
48. S. Myers, "A Possible New Injection and Accumulation Scheme for LEP", LEP Note 334 (1981)
49. P. Collier, Synchrotron Phase Space Injection into LEP, Proc. of PAC 95, pp. 551-553
50. M. Aiba et al., "Longitudinal Injection Scheme Using Short Pulse Kicker for Small Aperture Electron Storage Rings", Phys. Rev. ST Accel. Beams, 18, 020701 (2015)
51. M. Aiba, 'SLSII Upgrade Status', LER'20 (2020)
52. B. C. Jiang et al., "Using a double-frequency RF system to facilitate on-axis beam accumulation in a storage ring", Nucl. Instrum. and Methods in Phys. Research Section A, Volume 814, pp. 1- 5 (2016)

This project has received funding from the European Union's Horizon 2020 research and innovation programme under grant agreement No. 871072.

53. G. Xu et al., “On-axis Beam Accumulation Enabled by Phase Adjustment of a Double-Frequency RF System for Diffraction-Limited Storage Rings”, Proc. of IPAC ‘16, pp. 2032-2035 (2016)
54. G. Xu, “Longitudinal Accumulation in Triple RF Systems”, Presentation at Topical Workshop on Injection and Injection System, https://indico.cern.ch/event/635514/overview (2017)
55. M.-A. Tordeux, “Longitudinal Injection into Low-Emittance Ring: A Novel Scheme for SOLEIL Upgrade”, Presentation at Topical Workshop on Injection and Injection System, https://indico.cern.ch/event/635514/overview (2017)
56. S. White, N. Carmignani, M. Dubrulle, M. Morati, P. Raimondi, “Transparent injection for the ESRF-EBS”, IPAC’19, (2019)
57. T. Naito et al., “Multi-Bunch Beam Extraction Using Strip-line Kicker at ATF”, Nucl. Instrum. and Methods in Phys. Research Section A, Vol. 571, pp. 599--607, 2007
58. C. Yao et al., “Development of Fast Kickers for the APS MBA Upgrade”, PAC’15, (2015)
59. W. Waldron, “Injection Kicker and Pulser Development for ALS-U”, FLS’18, (2018)
60. T. Atkinson et al., “Development of a Non-linear Kicker System to Facilitate a New Injection Scheme for the BESSY II Storage Ring”, Proc. of IPAC’11, pp. 3394-3396
61. S. C. Leemann and L. O. Dalin, “Progress on Pulsed Multipole Injection for the MAX IV Storage Rings”, Proc. of PAC’13, pp.1052-1054
62. S. De Santis, “On-Axis Swap-Out Injection At ALS-U”, RuleTwiis19, (2019)
63. Y. Guo et al., ”Injection and Extraction Design of the Booster for the HEPS Project”, IPAC’18, (2018)
64. L. Hoummi et al., “Optimization and error studies for the USSR HMBA lattice,” in Proc. IPAC’21, (Campinas, SP, Brazil), ser. International Particle Accelerator Conference, https://doi.org/10.18429/JACoW-IPAC2021-MOPAB224, JACoW Publishing, Geneva, Switzerland, Aug. 2021, MOPAB224, pp. 730–733, isbn: 978-3-95450-214-1. doi: 10.18429/JACoW-IPAC2021-MOPAB224
65. S.M. Polozov et al., Current Results of the 4th Generation Light Source USSR (Former SSRS4) Development, Proc. of RuPAC2018
66. S.M. Polozov et al., Beam dynamics simulation results in the 6 GeV top-up injection linac of the 4th generation light source USSR, Proc. of RuPAC2018, p.285
67. L. Farvacque, Ed., EBS Storage Ring Technical Report, 2018
68. Ya.V.Shashkov et al. “Comparison of Higher Order Modes Damping Techniques for 800 MHz Single Cell Superconducting Cavities”, Nuclear Instruments and Methods in Physics Research A, v. 767, 2014, p 271–280.
69. J. Jacob, “The ESRF proposal for the RF system”, https://syncandshare.desy.de/index.php/s/kWS8MGgn5iQ2bgs
70. N.Sobenin and B.Zverev, “Electrodynamic Characteristics of Accelerating Cavities”, Foundation for International Scientific and Education Cooperation. Gordon and Breach Science Publishers S.A. 1999.
71. Matsievskiy, S.V et al. “Preliminary calculation of the power coupler for the SYLA storage ring RF cavity”, presented at the 27th Russian Particle Accelerator Conference (RuPAC 2021), September 2021, paper WEPSC12
72. E. Weihreter, “Status of the European HOM Damped Normal Conducting Cavity,” in Proceedings of EPAC 2008 (Genoa, Italy, 2008).
73. Shashkov YaV, Sobenin N P, Bazyl D S, Kaminskiy V I, Mitrofanov A A, Zobov M, 2016 Suppression of higher order modes in an array of cavities using waveguides, Journal of Physics: Conference Series, Volume 74, p. 116-123
74. Ya. V. Shashkov, A.A. Mitrofanov, N.P. Sobenin, V.L. Zvyagintsev, Analysis of higher order modes damping techniques in 9 cell cavity with modified drift tubes, Journal of Physics: Conference Series, Volume 74, p. 124-131
735. Einfeld D. Layout of a synchrotron light source //CERN Yellow Reports: Monographs. – 2020. – T. 1. – C. 19-19

This project has received funding from the European Union’s Horizon 2020 research and innovation programme under grant agreement No. 871072.

76. Onuki H., Elleaume P. (ed.). Undulators, wigglers and their applications. – CRC Press, 2002
77. European Sychrotron Radiation Facility. ESRF ID Parameters for OASYS.
url: http://ftp.esrf.eu/pub/scisoft/syned/lightsources3/
78. Kim K. J. X-ray data booklet, section 2.1, characteristics of synchrotron radiation //Published on-line by the Center for X-ray Optics and Advanced Light Source, Lawrence Berkeley National Laboratory (http://xdb. lbl. gov/Section2/Sec_2-1. html). – 2009
79. L. Rebuffi, M. Sanchez del Rio, "OASYS (OrAnge SYnchrotron Suite): an open-source graphical environment for x-ray virtual xperiments", Proc. SPIE 10388, 103880S (2017).
DOI: 10.1117/12.2274263
80. Chavanne J. et al. Prospects for the use of permanent magnets in future accelerator facilities //Proceedings of IPAC. – 2014. – T. 14.
81. Bahrdt J. Permanent magnets including undulators and wigglers //arXiv preprint arXiv:1103.1573. – 2011
82. Chavanne J., Elleaume P., Van Vaerenbergh P. End field structures for linear/helical insertion devices //Proceedings of the 1999 Particle Accelerator Conference (Cat. No. 99CH36366). – IEEE, 1999. – T. 4. – C. 2665-2667

This project has received funding from the European Union's Horizon 2020 research and innovation programme under grant agreement No. 871072.